QATAR UNIVERSITY

COLLEGE OF ENGINEERING

# GAS PURIFICATION USING A STATE-OF-THE-ART-SOLID-VAPOR-SEPARATION-UNIT: MODELING AND SIMULATION

BY

HANI Z. ABABNEH

A Dissertation Submitted to

the College of Engineering

in Partial Fulfillment of the Requirements for the Degree of

Doctorate of Philosophy in Chemical Engineering

January 2023

# COMMITTEE PAGE

The members of the Committee approve the Dissertation of
Hani Z. Ababneh defended on 20/10/2022.

Prof. Shaheen A. Al-Muhtaseb
Thesis/Dissertation Supervisor

Prof. Ramazan Kahraman
Committee Member

Prof. Fadwa Eljack
Committee Member

Prof. Abdulkarem Amhamed
Committee Member

Approved:

Khalid Kamal Naji, Dean, College of Engineering

ABSTRACT

ABABNEH, HANI Z., Doctorate: January : 2023,

Doctorate of Philosophy in Chemical Engineering

Title: Gas Purification Using a State-of-the-Art-Solid-Vapor-Separation-Unit: Modeling and Simulation

Supervisor ofDissertation: Shaheen, A., Al-Muhtaseb.

In spite of the increasing levels of greenhouse gases in the atmosphere and their sever impact on the environment, the demand for natural/bio gas is expected to increase significantly in the coming decades. To cover this demand, the global energy industry is continuously exploiting sour gas reserves located around the world. Nonetheless, sour gas has to be sweetened before the practical utilization of natural or biogas. On the other hand, the combustion of fossil fuels produces flue gases that contain huge amounts of carbon dioxide ($CO_2$) every year. $CO_2$ is a major greenhouse gas, which has negative impact on the environmental systems. Therefore, it is important to reduce or eliminate $CO_2$ from flue gases before being released to the environment.

On the other side, radioactive isotope byproducts (e.g., krypton and xenon) are found in off-gas streams released from nuclear power plants with light water reactors or from fuel reprocessing plants, and have to be separated from the off-gas stream. To our knowledge, so far there are no known processes to separate such noble gases, so this work will be the first to address this issue.

The cryogenic separation technologies have emerged as a new approach to separate carbon dioxide ($CO_2$) and hydrogen sulfide ($H_2S$) from natural gas, and to capture $CO_2$ gas from flue gas streams. To design cryogenic separation equipment, vapor-liquid equilibrium (VLE), solid-liquid equilibrium (SLE), solid-vapor

equilibrium (SVE), and solid-liquid-vapor equilibrium (SLVE) data for the corresponding binary and ternary systems composing the corresponding gas mixtures.

In this study, we successfully develop an empirical correlation model based on the Peng-Robinson equation of state (PR EoS), with fugacity expressions, that is able to describe the SLVE behaviors for the ternary systems of $CH_4$-$CO_2$-$H_2S$ (resembling a sample natural gas mixture), $N_2$-kr-Xe (resembling noble gases in nitrogen), and $N_2$-$O_2$-$CO_2$ (resembling flue gas mixtures) over wide ranges of pressures and temperatures. Additionally, and based on this model, an equilibrium stage separation unit was modeled and used to construct phase diagrams of the solid-fluid regions for the above-mentioned systems. The results showed that separating the unwanted gases in the solid–vapor equilibrium (SVE) region by selective freezing (solidification) is efficient and results in high recovery rates, the recovery of acid gases (such as $CO_2$) could exceed 99%. Based on that, and by implementing the model developed, a state-of-the art solid-vapor (SV) separation unit was modeled using the Aspen Custom Modeler (ACM) software. The SV unit was then simulated by importing the ACM code into an Aspen Plus simulator; and its performance was studied and analyzed. The SV separation unit offers some key advantages over the traditional technologies (such as amine scrubbing units);including lower energy requirements, less capital costs, lower maintenance and operation expenses and the avoidance of contaminating the gases with other components (such as solvents). In natural gas sweetening, the developed SV unit consumes only ~27% of the energy required by the amine sweetening unit; while for $CO_2$ capture from flue gases, it saves about half of the energy needed by traditional units. For separating noble gases from nitrogen, the SV unit also achieved high recoveries, especially for xenon gas; however the operating temperature would be too

low, thus requiring high energy for cooling.

# DEDICATION

*This dissertation is lovingly dedicated*

*To my grandparents Aisha Ababneh and Salim Ababneh*

*May Allah have mercy on them,*

*to my parents Zakariya Ababneh and Radieh Obeidat,*

*my lovely wife Haya Abu Mater, my brother and sister*

*,my beautiful son Rayyan, my grandmother Aisha Al-Khatib, and*

*my advisors Prof. Al-Muhtaseb*

*Without their endless love, support, prayers, and encouragement*

*with the grace of Allah Almighty*

*it would not have been made possible*

*I am truly thankful for having you all in my life.*

# ACKNOWLEDGMENTS

Starting with the Name of Allah, the Most Beneficent, the Most Merciful; and prayers and peace be upon our Prophet Muhammad, the Messenger of Allah and all his family and companions. First and foremost, praise be to Allah who provided me with health, knowledge and competence until I reached the end of this PhD journey.

I would like to acknowledge the support of Qatar University for providing all the needs to achieve the requirements of this dissertation

I would like to express my sincere gratitude to my advisor Prof. Shaheen Al-Muhtaseb for the continuous support of my PhD study and related research during the last four years, for his patience, motivation, and immense knowledge. His great motivation, curiosity and approach have been fundamental not only for this Ph.D study and research, but also for my future career.

I would like also to extend my sincere appreciation to Dr. Ahamd Al-Nouss and Prof. Karimi for their help, and collaborative support in this work. I extend my appreciation to the faculty and members of the Department of Chemical Engineering for their support in this research.

Last but not the least, I would like to express my deep thanks and gratitude to my parents, brothers and sister for their encouragements and support; and special thanks to my wife and son for their patience and spiritual support throughout this journey

TABLE OF CONTENTS

# LIST OF TABLES

# LIST OF FIGURES

ABBREAVATION

| | |
|---|---|
| $\hat{f}_i^F$ | Fluid phase fugacity of component *i* in the mixture |
| $\hat{f}_i^S$ | Solid phase fugacity of component *i* in the mixture |
| $\dot{n}_{Feed}$ | Molar flow rates of the feed stream |
| $\dot{n}_{Liquid}$ | Molar flow rates of the liquid stream |
| $\dot{n}_{Solid}$ | Molar flow rates of the solid stream |
| $\dot{n}_{Vapor}$ | Molar flow rates of the vapour stream |
| $\widehat{\varphi}_{0i}^{Sat}$ | Fugacity coefficient of the solid component in the mixture at temperature T |
| $\widehat{\varphi}_i^F(T, P, x^F)$ | Fugacity coefficient of the component *i* in the fluid mixture of molar composition |
| $\dot{H}$ | Enthalpy rate |
| $M_{Calculated}$ | Calculated property (M) value |
| $M_{Exp.}$ | Experimental property (M) value |
| $P_{0i}^{Sat}(T)$ | Saturation/sublimation pressure of the solid forming component at the temperature *T* |
| $P_m$ | Melting pressure |
| $P_t$ | Triple point pressure |
| $T_m$ | Melting temperature |
| $T_t$ | Triple point temperature |
| $v_{0i}^S$ | Solid molar volume of the component *i*. |
| $x^F$ | Molar compositions of component in the fluid phase |
| $x_i$ | Molar fraction of component *i* in liquid phase |

| | |
|---|---|
| $y_i$ | Molar fraction of component *i* in vapor phase |
| $\mu_i^F$ | Chemical potential of the component *i* in the fluid phase |
| $\mu_i^S$ | Chemical potential of the component *i* in solid phase |
| $\Delta h_i^{sub}$ | Molar enthalpy of sublimation of component $i$ |
| $\Delta h_m$ | Enthalpy change of melting |
| $\Delta H_f$ | Enthalpy of fusion |
| $\Delta H_{sub}$ | Enthalpy change at sublimation. |
| $\Delta c_p$ | Change of the heat capacity upon the transition from the solid phase to liquid phase |
| $\Delta v^{S-L}$ | Solid−liquid molar volume difference |
| $\Delta v$ | Change in molar volume upon transition from the solid phase to the liquid phase |
| *a* | Parameter of attractive forces between molecules |
| AAD | Average absolute deviation |
| ACM | Aspen custom modeler |
| ANN | Artificial neural networks |
| *b* | Solid covolume |
| *c* | Liquid covolume |
| CCC-CFG | Compressed flue gas cryogenic carbon capture with compressed flue gas |
| CCC-ECL | Cryogenic carbon capture with an external cooling loop |
| CFZ | Controlled freezing zone |
| *d*, *k*, *q* and *r* | Fitting parameters |

| | |
|---|---|
| DIPA | Diisopropanolamine |
| $F$ | Feed amount or feed flow rate |
| $g$ | Minimum Gibbs free energy |
| GHG | Greenhouse gases |
| $H$ | Enthalpy |
| $k_{ij}$ | Equation of state interaction parameter |
| $L$ | Liquid phase amount or flow rate |
| LNG | Liquefied natural gas |
| MAD | Mean absolute deviation |
| MDEA | N-methyldiethanolamine |
| MRD | Mean relative deviation |
| $N$ | Number of experimental data points |
| NRTL | Non-random two-liquid model |
| P | Pressure |
| PR EoS | Peing-Robinson equation of state |
| PR-HV | Peng Robinson-Huron-Vidal mixing rule |
| PSRK | Soave–Redlich–Kwong |
| $\dot{Q}$ | Cooling/heating rate |
| QP | Quadruple point |
| $R$ | Universal gas constant |
| $S$ | Solid phase amount or flow rate |
| $S$ | Entropy |
| SLE | Solid-liquid equilibrium |
| SLVE | Solid-liquid-vapor equilibrium |
| SVE | Solid-vapor equilibrium |

| | |
|---|---|
| $T_{exp}$ | Experimental temperature |
| TPC | Time projection chamber |
| $T_{pred}$ | Predicted value of temperature |
| $v_0$ | Molar volume of $CO_2$ in the hypothetical subcooled liquid state |
| $V$ | Vapor phase amount or flow rate |
| VLE | Vapor-liquid equilibrium |
| WIMP | Weakly interacting massive particle |
| $Z_i$ | Mole fraction of component *i* in the feed |

# CHAPTER 1: INTRODUCTION

In 2019, natural gas accounted for about 25% of the global primary energy consumption [1], and it is expected to increase by 33% throughout the next 30 years [2]. This anticipated increase is due to the discovery of new natural gas and gas condensate fields around the world, in addition to the fact that natural gas has a lower carbon footprint than coal or petroleum products [3]. The increased demand for natural gas and the strictest targets for the share of renewable fuels in the global energy consumption led to an increasing interest in the use of biogas as an alternative source of energy [4]. Natural gas and biogas consist mainly of methane ($CH_4$), carbon dioxide ($CO_2$), hydrogen sulfide ($H_2S$), along with possible traces of water and other pollutants like ammonia, and particulates [5]. It is estimated that 40% of the proven natural gas fields are sour with high $CO_2$ and $H_2S$ contents, which could be as high as 70% [6], [7]. Such acid gases reduce the energy density of the natural gas significantly; hence, lowering its usefulness and selling price. In addition to that, the high content of $CO_2$ and $H_2S$ can result in corrosion and clogging of pipelines and equipment of liquefaction plants [8]. Thus, the natural gas industry has to look for innovative solutions that make the exploitation of such sour gas reserves economically viable.

Carbon dioxide ($CO_2$) has reached an alarming concentration level in the atmosphere. Carbon dioxide resulting from the combustion of fossil fuels accounts for the largest share of global anthropogenic GHG emissions [9]. This has increased the global mean surface-temperature by ~1 °C from the pre-industrial era levels [10]. In order to decelerate or stop the global warming phenomena, the demand for cleaner energy sources has increased. Hydrogen sulfide ($H_2S$) is a colorless component commonly found in natural gas. it is highly corrosive and it caused many failures of pipelines and pressure vessel in the oil and gas industry [11]. In addition to that, $H_2S$ is

a very poisonous and flammable gas with an odor similar to that of rotten eggs [12]. The $H_2S$ removed from sour gas can be a precursor for the production of elemental sulfur, and organosulfur compounds such as methanethiol, ethanethiol, and thioglycolic acid [13].

Flue gases resulting from the combustion of fossil fuels are among the major sources of carbon dioxide ($CO_2$) and other greenhouse gases emitted to the atmosphere [14]. Flue gases are a mixtures of water vapour ($H_2O$), nitrogen ($N_2$), particulates, heavy metals and acid gases (such as $CO_2$ and $H_2S$). Additionally, in case of incomplete combustion, flue gases contain carbon monoxide (CO) and volatile organic compounds (VOCs) [15]. The typical composition of flue gases emitted from natural gas-fired power plants is 8-10% $CO_2$, 18-20% $H_2O$, 2-3% $O_2$, and 67-72% $N_2$ [16].

Generally, there are three main techniques for carbon capture from flue gases: post-combustion, oxy-combustion, and pre-combustion [17]. Figure 1-1 illustrates the three approaches toward carbon capture in energy industry [18]. In the pre-combustion approach, a fossil fuel is converted to syngas (a mixture of $H_2$ and CO gases) by the means of gasification or reforming processes [19]. Advantages of pre-combustion include the high concentration of $CO_2$, hence the process equipment can be smaller and different solvents may be used; which makes the process less energy intensive compared to post-combustion techniques [18]. However, it requires high capital costs needed for the fossil-fuel-conversion equipment [20]. In the oxy-fuel combustion process, fuel or natural gas are combusted in a pure oxygen environment instead of using atmospheric air, therefore the resulted flue gas would have higher $CO_2$ concentrations since there is no nitrogen to dilute it [21]. On one hand, this technology significantly reduces the cost and the energy needed for carbon capture. On the other hand, the need for an air separation unit to produce an oxygen-rich atmosphere sharply

increases the overall capital cost [19].

In the post-combustion approach, $CO_2$ is sequestrated from the flue gas stream after the complete combustion of fuels [22]. Post-combustion technologies are also used to remove sour gases from natural gas. Post-combustion technologies can be easily integrated with most existing fossil-fuel operated plants or natural gas sweetening units. However, the main drawback of this approach is the relatively low $CO_2$ concentration in the flue gas, which increases the separation difficulty [17]. The most widely used post-combustion carbon capture technology in the industry is the solvent (e.g., amine)-based absorption technology. Nonetheless, this technology suffers from the high-energy requirements to regenerate and reuse the required solvent and the high maintenance and operation costs [23]. The cryogenic separation technologies have caught the attention of engineers and scientists as a new alternative technology to capture $CO_2$ from flue gas mixtures, and remove sour gases from natural gas. The cryogenic separation offers few advantages over the solvent-based absorption technology; including the lower environmental footprint, eliminating the need for solvents (which eliminates the possibilities of product contaminations) and the lower cost to build and operate [24]. The cryogenic separation is a physical process, which relies on the differences in volatility between sour gases and the other gases in flue/natural gas to separate the carbon dioxide and hydrogen sulfide in a different phase at very low temperatures [5]. The cryogenic separation techniques could be divided into conventional methods (e.g., liquid–vapor separation), nonconventional methods (e.g., solid–vapor separation) [25], and hybrid methods [8]. Depending on the technology utilized, the solid formation could be desirable or avoidable. For example, the Controlled Freezing Zone $(CFZ)^{TM}$ technology depends on the solid formation to improve the separation process [26].

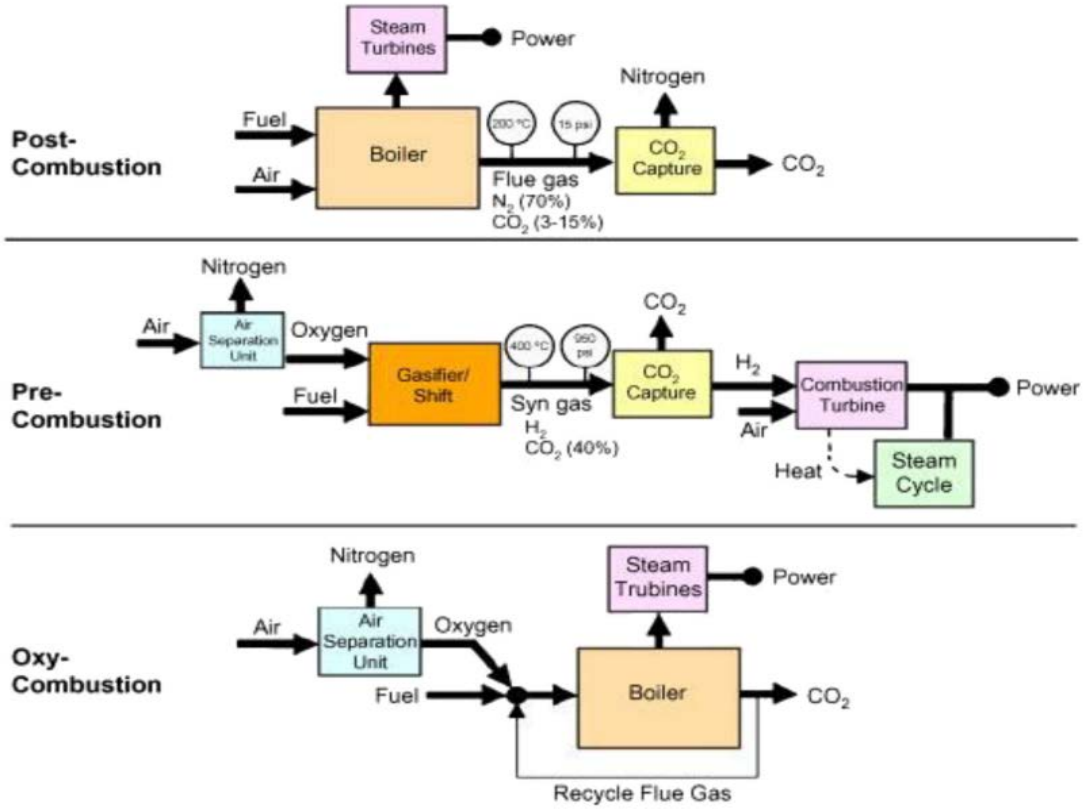


Figure 1-1: The three main approaches for $CO_2$ capture [18].

The most widely used conventional method is the cryogenic distillation, which operates at very low temperatures and high pressures in order to separate $CO_2$ from other components based on the differences in their boiling temperatures, where the carbon dioxide is removed either in a high-pressure gas phase or in a liquid phase. Despite the effectiveness of conventional cryogenic methods in separating concentrated $CO_2$ stream, it is considered an expensive-to-operate technology due to the high energy required to reach high pressures, and the necessity of avoiding solids formation [25]. Nonconventional methods benefit from anti-sublimation or solidification to improve the separation process and reduce the energy requirements [27]. Nonconventional methods usually operate at lower temperatures compared to cryogenic distillation, at which $CO_2$ will solidify. Even though these sources discuss only the solidification of $CO_2$, $H_2S$ removal by solidification is similar. Nonconventional technologies include;

cryogenic packed beds [28], moving packed beds [29], Stirling coolers [30], cryogenic carbon capture with an external cooling loop (CCC-ECL) [31], and compressed flue gas cryogenic carbon capture with compressed flue gas (CCC-CFG) [31]. Hybrid methods combine conventional and nonconventional methods into a single-unit operating system to overcome the disadvantages of conventional methods and produce better or similar results at lower cost than nonconventional technologies [8]. Examples on hybrid methods include the Controlled Freezing Zone (CFZ) technology [7], Cryocell-based separation [32] and condensed contaminant centrifugal separation [31].

Cryogenic distillation has been used in the air separation industry for many decades, where gaseous oxygen and nitrogen are produced in large quantities [33]. Krypton and xenon are noble gases that are found naturally in air [34]. They can also be found as byproducts of fission nuclear reactions [35], and radioactive isotopes of krypton and xenon are found in off-gas streams from nuclear power plants with light water reactors or from fuel reprocessing plants [36]. They were also found in the xenon dark matter project, which uses xenon in a dual-phase time projection chamber (TPC) for the direct detection of weakly interacting massive particle (WIMP). However, $^{85}$Kr (which can be naturally present with xenon) has to be separated in order to maintain the performance of their detector [37]. Therefore, it is important to develop techniques to separate these two components from their mixtures, and one of these techniques is cryogenic separation.

### 1.1. Scope and Objectives

To design low-temperature separation processes' units and equipment, experimental or predicted data of vapor-liquid equilibrium (VLE), solid-liquid equilibrium (SLE), solid-vapor equilibrium (SVE), and solid-liquid-vapor equilibrium (SLVE) are needed. These data will aid in developing accurate and suitable

thermodynamic models, which can predict pressure, temperature and phase compositions of corresponding phase equilibria.

This dissertation aims to:

1- Develop a thermodynamic model that can describe the solid-liquid-vapor (SLV) phase equilibria for the ternary system of $CH_4$-$CO_2$-$H_2S$ (representing sour natural gas stream) over wide ranges of pressure (5-30 bars) and temperatures (130 to 200 K)..

2- Develop a thermodynamic model that can describe the solid-liquid-vapor (SLV) phase equilibria for the ternary system of Kr-Xe-$N_2$ over specific ranges of pressures and temperatures (1-45 bar and 80-180 K, respectively)

3- Develop a thermodynamic model, that is able to describe the SLVE and SVE behaviors for the flue gas ternary system of $N_2$-$O_2$-$CO_2$ at pressures ranging from 1 to 45 bar and temperatures ranging from 80 to 180 K model a solid-vapor (SV) separation unit for the three above-mentioned ternary systems using Aspen Custom Modeler (ACM) software.

4- Export the modeled unit to Aspen Plus environment, and integrate into various process flow diagram; natural gas sweetening process, carbon dioxide capture process from industrial flue gas, and the process of separating noble gases from nitrogen.

5- Compare the performance of the modeled SV separation unit to conventional –common technologies such as amine scrubbing.

## 1.2 Novelty and contribution

By developing the thermodynamic models to describe the solid-fluid equilibria for the ternary systems; natural gas, flue gas, and noble gases in nitrogen; it would be possible for the first time to construct phase diagrams that accurately determine solid-fluid phase regions for each of these systems. Additionally, developing such models accurately helps researchers and the professionals in industries by providing them with a useful tool that allows the prediction of the ternary solid-fluid phase equilibrium behaviors as well as the separation applications of such mixtures without the need for experimental data, which in turn expands their potentials and optimizes their budget and time.

The modeled SV separation unit, which is the first of its kind in the literature, lays the basis for its further development for $CO_2$ capture from flue gases, natural sweetening, and noble gas separation from nitrogen. Furthermore the SV separation unit has the potential to be further developed for more applications in the energy and chemical industries, such as natural gas hydrates and air components separation.

# CHAPTER 2: BACKGROUND AND LITERATURE REVIEW

Since this dissertation is mainly dealing with three different systems; i.e., sour natural gas, $CO_2$-rich flue gas, and noble gases in nitrogen, this chapter is divided into three different sections that address each of these systems.

## 2.1 Natural gas system ($CH_4$- $CO_2$-$H_2S$)[1]

The objective of this section is to review the solid-liquid-vapor equilibrium (SLVE) for the acid gases in natural/bio gas; which involves the binary systems of $CH_4$-$CO_2$, $CH_4$-$H_2S$ and $H_2S$-$CO_2$ as well as the ternary system of $CH_4$-$H_2S$-$CO_2$. It will cover the published experimental data, which include the SLVE locus curve and the composition of each phase at that point.

Experimental data available for the SLVE locus involving $CH_4$, $CO_2$ and $H_2S$ are limited in the literature. This section will give an overview of the experimental data for the binary systems of $CH_4$-$CO_2$, $CH_4$-$H_2S$ and $H_2S$-$CO_2$ as well as the ternary system of $CH_4$-$H_2S$-$CO_2$.

The experimental SLVE data of the binary system $CH_4$-$CO_2$ comes mainly from four different studies by Donnelly and Katz [38], Pikaar [39], Sterner [40] and Davis et al. [41]. Donnelly and Katz [38] determined the SLVE locus by varying the $CO_2$ content within the $CH_4$-$CO_2$ mixtures and finding the phase envelope using a glass windowed pressure cell. They prepared six mixtures with $CO_2$ concentrations from 0% (pure $CH_4$) to 88% and tested them at temperatures up to 215.3 Kelvin. Pikaar [39] investigated the SLVE locus in a temperature range from 143.15 to 203.15 Kelvin, with $CO_2$ concentrations between 1% and 20%. He noticed a variation between his results and

[1] This section was taken from the published article: H. Ababneh and S. A. Al-Muhtaseb, "A Review on the Solid-Liquid-Vapor Phase Equilibria of Acid Gases in Methane," Greenh. Gases Sci. Technol., vol. 12, no. 4, pp. 566–579, 2022, doi: 10.1002/ghg.2161.

those of Donnelly and Katz at low temperatures, and concluded that the results of Donnelly and Katz maybe inaccurate at temperatures lower than 206.15 Kelvin. Sterner measured the SLVE locus at temperatures lower than the critical temperature of pure $CH_4$ [40]. Davis et al. [41] measured the SLVE locus starting from the triple point of $CO_2$ up to a temperature of 97.54 Kelvin. Their measurements covered a wide range of temperatures and included the vapor and liquid phase compositions over the locus line. Figure 2-1a compares the results for the four sets of experimental data. On the other hand, only Davis et al. [41] reported the compositions of different phases at the SLVE locus of the binary system $CH_4$-$CO_2$. They confirmed that the solid phase consists of pure $CO_2$, while the other two phases (vapor and liquid) contain both components. The liquid and vapor phase compositions were measured in the temperature ranges from 129.65to 201.26 Kelvin and from 140.93 to 205.71 Kelvin, respectively. Figure 2-1b illustrates the composition of carbon dioxide in liquid and vapor phases. Experimental data for this binary system cover a wide range of temperature and pressure; and laboratory data available are close to each other as seen in Figure 2-1. Table 2-1 summarizes the experimental data for the SLVE equilibrium of $CH_4$-$CO_2$ system.

From Figure 2-1a it is clear that most of the experimental data follow the same SLVE locus curve trend, where the pressure will increase with temperature, until reaching a pressure peak value at a temperature of around 202 Kelvin, and then it will drop down reaching the triple point of $CO_2$. Within the SLVE locus curve envelop, two phases will be present; vapor and solid. While around this envelop liquid phase will be present as only liquid phase, liquid/solid phase or liquid/vapor phase.

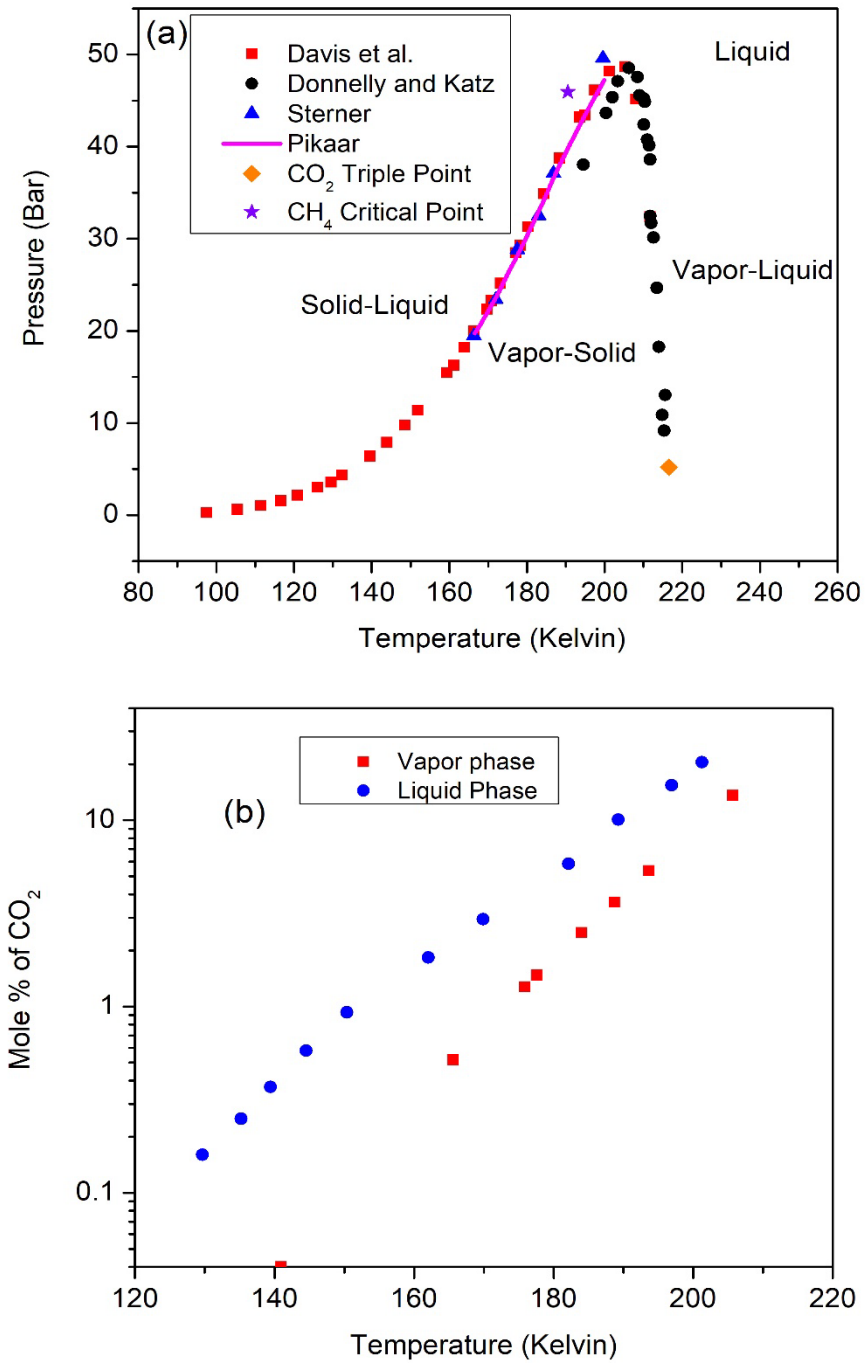


Figure 2-1: Experimental data available for the binary system $CH_4$-$CO_2$ in terms of (a) SLVE locus [41][38][40][39], $CO_2$ triple point [42], $CH_4$ critical point [43] and (b) corresponding $CO_2$ compositions in the liquid and vapor phases (while solid phase is pure $CO_2$) [41].

While laboratory data covering the vapor-liquid equilibrium of the binary system $CH_4$-$H_2S$ are abundant [44]–[46], experimental data covering the SLVE of this system are limited. The main study covering the thermodynamics of this system was conducted by Kohn and Kurata [47]. They developed an experimental setup for determining the solid phase behavior of the $CH_4$-$H_2S$ system, six mixtures of methane and hydrogen sulfide were tested, the system temperature was varied from -300 to 300 °F (88.7-422 Kelvin), and pressures reaching up to 2000 psia (137.9 bar). For this binary system, there are two SLVE loci; the $SL_1VE$ locus and the $SL_2VE$ locus (where $L_1$ is the liquid phase that is rich with $CH_4$ and $L_2$ is the liquid phase that is rich with $H_2S$), where the solid phase consists of pure hydrogen sulfide. The $SL_1VE$ and $SL_2VE$ loci meet at the quadruple point (QP) at which four phases are present, i.e., $SL_1L_2VE$. The results obtained for the SLVE locus of this binary system are shown in Figure 2-2. Within these point and below the QP point, two phases are only present: a pure solid $H_2S$ phase and a vapor phase (which consists of both components). Table 2-1 lists the experimental data available for this binary system, it could be noticed that more works might be needed to confirm and expand the laboratory data available.

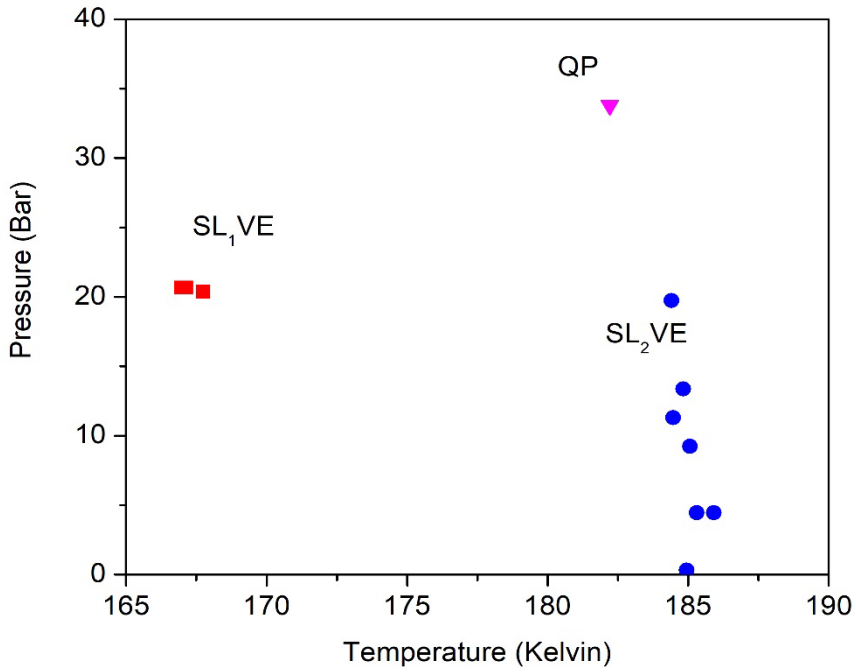


Figure 2-2: Measured Pressure-Temperature SLVE locus of the binary system CH4-H2S [47].

Similar to the $CH_4$-$H_2S$ binary system, there are many experimental studies covering the VLE of the $CO_2$-$H_2S$ system [48]–[50]. However, only the study by Sobocinski and Kurata [51] covered the SLVE of this binary system. They have conducted an experimental investigation that covered the region from the critical locus of the mixture to the SLVE region. Seven mixtures were tested individually to determine the phase diagrams and the compositions of each phase at the specified conditions. It was observed that SLVE locus is at temperatures lower than triple point of either pure $CO_2$ and $H_2S$, which was explained by the formation of a eutectic mixture (with a composition of 12.5 mole% $CO_2$ for all mixtures). Figure 2-3a illustrates the SLVE locus of the $CO_2$-$H_2S$ binary system, which ends up near to the triple point of $CO_2$ (216.58 Kelvin, 5.185 bar [42]). Below this line, both vapour and solid phases are found. Above this line, liquid phase can be present with either solid or vapour phases.

Figure 2-3b shows the composition of the vapour and liquid phases alongside the SLVE locus, where the solid phase consisted of pure $CO_2$ [51]. The experimental data for the $CO_2$-$H_2S$ system found in Figure 2-3 and Table 2-1 is limited. Therefore, more research is recommended to be done for the experimental determination of the SLVE locus for this system.

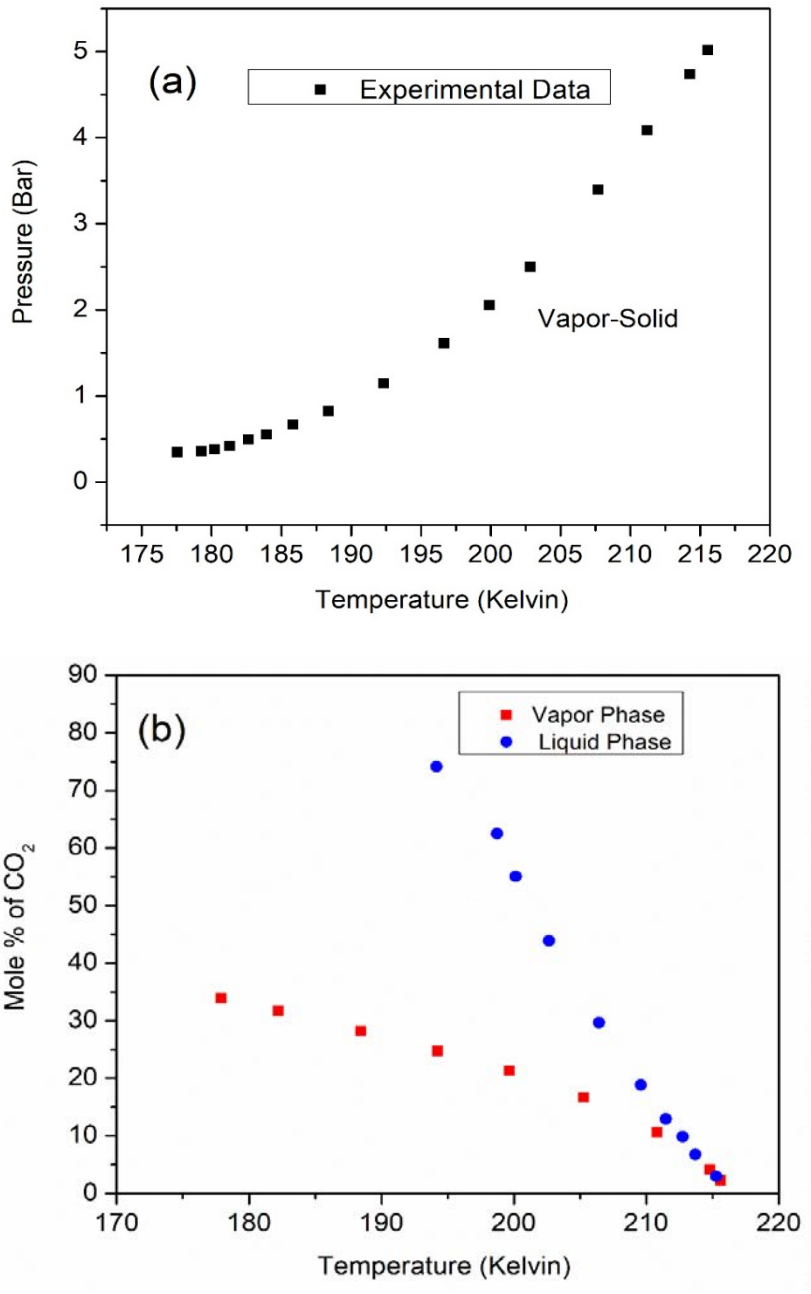


Figure 2-3: Experimental Data (symbols) available for the binary system $CO_2$-$H_2S$ in terms of (a) SLVE pressure-temperature locus and (b) corresponding $CO_2$ compositions in the liquid and vapor phases [51].

Experimental data, which covers the solid phase in the $CH_4$-$CO_2$-$H_2S$ ternary system are rare and have limited temperature and pressure ranges. Langé et al. [6] designed an experimental procedure to obtain the *T-P-x-y* data for the region in which

the SLVE locus exists for different compositions of this ternary system. However, their study covered only the region that contains solid $CO_2$ phase, and the temperature and pressure ranges were very limited (from 199.44 to 207.59 Kelvin and 14.599 to 43.212 bar, respectively). Théveneauet al. [52] utilized a visual synthetic laboratory technique to determine the freezing point of 5 different compositions of the ternary system $CH_4$-$CO_2$-$H_2S$. Table 2-2 lists the mole% of each component in these mixtures, where $Z_i$ is the overall composition of component *i* in the mixture. However, this study also covered very limited ranges of temperature and pressure (192-210 Kelvin and 18.48-22.24 bar, respectively). Similar to the two binary systems $CH_4$-$H_2S$ and $CO_2$-$H_2S$, the ternary system of the $CH_4$-$CO_2$-$H_2S$ available in the literature are limited (Table 2-1), and more work is needed to expand our knowledge and develop more accurate phase envelopes for such system.

Table 2-1: Summary of the experimental data for SLV loci of different binary and ternary systems of $CH_4$, $CO_2$ and $H_2S$.

| Mixture | Temperature range (Kelvin) | Pressure range (Bar) | Reference |
|---|---|---|---|
| $CH_4$-$CO_2$ | 194.5-215.3 | 9.17-48.54 | Donnelly and Katz [38] |
| | 143.15 to 203.15 | 19.74-47.23 | Pikaar [39] |
| | 166.33-199.6 | 19.47-49.61 | Sterner [40] |
| | 97.54-211.71 | 0.28-48.68 | Davis et al. [41] |
| $CH_4$-$H_2S$ | 167.1-184.9 | 0.32-20.68 | Kohn and Kurata [47] |
| $CO_2$-$H_2S$ | 177.9-215.6 | 0.35-5.02 | Sobocinski and Kurata [51] |
| $CH_4$-$CO_2$-$H_2S$ | 199.44 to 207.59 | 24.04-43.21 | Langé [6] |
| | 192-210 | 18.48-22.24 | Théveneauet [52] |

Table 2-2: Compositions of the five mixtures tested for solidification point [52].

| Mixture | $Z_{CH4}$ | $Z_{CO2}$ | $Z_{H2S}$ | P (bar) | $T_{exp}$ (Kelvin) |
|---|---|---|---|---|---|
| 1 | 0.7993 | 0.2007 | 0 | 22.24 | 209.80 |
| 2 | 0.7603 | 0.1899 | 0.0498 | 21.86 | 202.33 |
| 3 | 0.7192 | 0.1806 | 0.1002 | 18.48 | 196.85 |
| 4 | 0.6802 | 0.1701 | 0.1497 | 19.74 | 194.32 |
| 5 | 0.6395 | 0.1604 | 0.2001 | 21.23 | 192.26 |

Pascal et al. [3] have used a visual synthetic experimental method to find the solidification point for five compositions of the ternary mixture CH4-CO2-H2S. The compositions of these mixtures are listed in Table 2-3.

Table 2-3: Temperatures of solidification for various compositions of th ternary mixture $CH_4$-$CO_2$-$H_2S$ [3].

| Mixture | $Z_{CH4}$ | $Z_{CO2}$ | $Z_{H2S}$ | P (MPa) | $T_{exp}$ (Kelvin) |
|---|---|---|---|---|---|
| 1 | 0.7993 | 0.2007 | 0 | 2.224 | 209.80 |
| 2 | 0.7603 | 0.1899 | 0.0498 | 2.186 | 202.33 |
| 3 | 0.7192 | 0.1806 | 0.1002 | 1.848 | 196.85 |
| 4 | 0.6802 | 0.1701 | 0.1497 | 1.974 | 194.32 |
| 5 | 0.6395 | 0.1604 | 0.2001 | 2.123 | 192.26 |

## 2.2 Flue gas system ($N_2$-$O_2$-$CO_2$)[2]

The equilibrium data involving a solid phase for the binary system $N_2$-$CO_2$ are few and limited. The SVE of this binary system was studied experimentally by Sonntag and Van Wilen [53] and Smith et al. [54], while SLE studies included those of Rest et al. [55], Yakimenko et al. [56], and Fedorova [57]. Figure 2-4 shows the composition of the vapor phase in the SVE region of the binary system $N_2$-$CO_2$ as obtained by by Sonntag and Van Wilen [53]. SLVE experiments were conducted by Schweitzer [58] and Fandino et al. [59]. Figure 2-5 shows the SLVE locus for the binary system $N_2$-$CO_2$ reported by Schweitzer [58].

To the best of our knowledge, no published SVE or SLVE experimental data are available the binary system $O_2$-$CO_2$; whereas the only available equilibrium data that involves a solid phase is SLE data [55], [57], [60], [61]. On the other hand, no solid formation is anticipated within practical operating conditions for the binary system $O_2$-$N_2$. Thus, only VLE data of this system are considered.

[2] This section was taken from the article currently under review: H. Ababneh, A. AlNouss, and S. A. Al-Muhtaseb, "Carbon Capture from Post Combustion Flue Gas Using a State-of-the-Art, Anti-Sublimation, Solid-Vapor Separation Unit"

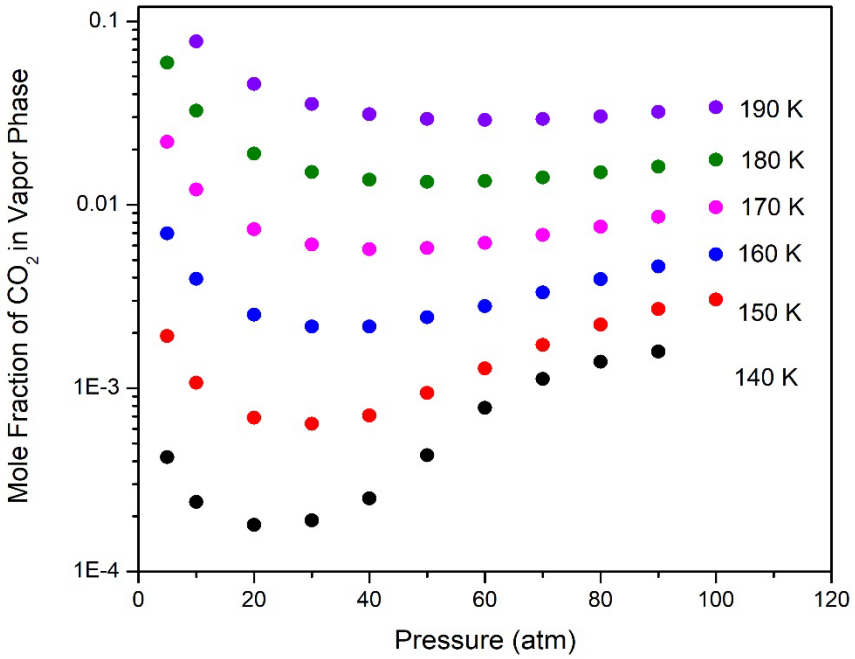


Figure 2-4: Carbon deoxide composition in the vapor phase in SVE region for the binary system $N_2$-$CO_2$ as reported in [53].

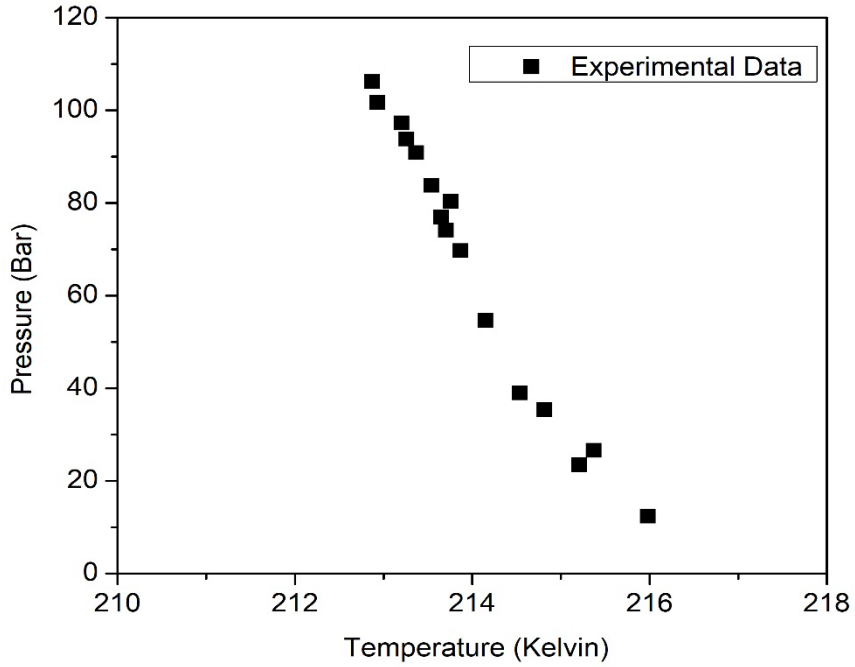


Figure 2-5: Experimental data for the SLVE locus of the binary system $N_2$-$CO_2$ as obtained by Schweitzer [58].

### 2.3 Noble gases in nitrogen system ($N_2$-Kr-Xe)[3]

Indeed, the experimental data for the SLVE of the ternary system Kr-Xe-$N_2$ are very limited in the literature. Nonetheless, Teller and Knapp [36] studied the solubility of solid Kr and Xe in liquid nitrogen. For the binary system of Kr-$N_2$, the SLVE locus was obtained in the temperature range of (71.81-115.77 K) [36], while for the Xe-$N_2$ binary system, it was tested at two temperature ranges (from 91.04 to 127.29 K and from 153.6 to 161.36 K) [36]. Moreover, they obtained the SLVE locus and the phase compositions for the ternary system Kr-Xe-$N_2$ at a pressure of 6 bar and over a limited temperature range (from 98.48 to 104.9 K) [36]. Experimental solid-liquid equilibrium (SLE) data could be found for the binary systems of Kr-Xe [62] and Kr-$N_2$ [63]. Additionally experimental SLVE data for the binary system of Kr-Xe could be found in [63].

[3] This section was taken from the published article: H. Ababneh and S. A. Al-Muhtaseb, "Prediction of solid-liquid-vapor phase equilibria of noble gases in nitrogen," Arab. J. Chem., vol. 15, no. 6, p. 103866, 2022, doi: 10.1016/j.arabjc.2022.103866.

# CHAPTER 3: METHODOLOGY[4]

In order to simulate the solid-fluid equilibrium behaviors of the different phases encountered in gas separation processes, and to design the corresponding separation equipment; thermodynamic properties of different gases in the liquid and vapor phases, as well as solid phase formation conditions have to be determined. A thermodynamic model able to describe the vapor, liquid and solid phases of the different gas mixtures is developed to calculate and determine accurately the needed properties.

This study was conducted in different stages. The first stage was to choose appropriate thermodynamic mathematical model to represent each of the three different systems covered. The second stage was to program a code of this thermodynamic model into Aspen Custom Modeler (ACM) V11, which is a process and equipment model development and simulation environment that is based on a programming language code (in the background) that is specific to chemical engineering applications, and involves built-in details of chemical components, their thermophysical properties and process thermodynamics. ACM allows the user to design and build customized models or equipment. So, instead of writing codes, the user write engineering equations that describes such models or equipment, and the ACM provides a powerful tool to execute these models to simulate and optimize continuous, batch, or semi-batch processes [64]. In order to test the model and confirm its accuracy; the model predictions for the different binary mixtures are compared to the experimental data available in the literature. Following that, the ACM model was executed at specified number of conditions where experimental data is available for the ternary systems.

---

[4] This chapter was taken from the published article: H. Ababneh and S. Al-Muhtaseb, "An Empirical Correlation-Based Model to Predict Solid-Fluid Phase Equilibria and Phase Separation of the Ternary System CH4-CO2-H2S," J. Nat. Gas Sci. Eng., vol. 94, p. 104120, 2021, doi: https://doi.org/10.1016/j.jngse.2021.104120.

In this chapter, the model used to represents equilibrium models involving solid and fluid phases for the binary and ternary systems is discussed alongside the models and approaches used in different studies published in the literature are reviewed.

## 3.1 Modelling

There are three major approaches to model the solid-fluid phase equilibria. The first approach utilizes equations of state (EoS) for calculating the liquid and vapor phase fugacities, along with an independent model for the fugacity of the solid phase. The first approach could be further classified according to the model used to estimate the solid phase fugacity; such as the empirical correlation model [65], thermodynamic integration model [66], and Gibbs free energy EoS model [67]. The second approach depends on using an EoS for calculating the fugacities of the three phases the same time [68]. A completely different approach was used by Ali et al. [69] to predict the SLVE locus curve , where they developed a predictive model that utilizes artificial neural networks (ANN), and the ANN predictions were compared to the experimental data.

This study develops an empirical correlation model based on Peng-Robinson equation of state (PR EoS), with fugacity expressions, that is able to describe the solid-fluid phase equilibria for the different ternary systems discussed in this work.

## 3.2 Empirical correlation model

At the phase equilibrium condition of a multicomponent system, the chemical potentials of each component(s) in the two or three coexisting phases (S: solid phase, V/L: vapour and/or liquid phase) at the same temperature ($T$) and pressure ($P$), i.e.,

$$\mu_i^S(T,P) = \mu_i^F(T,P,x^F) \qquad (3\text{-}1)$$

where $\mu_i^S$ is the chemical potential of the component $i$ in a pure solid phase and $\mu_i^F$ is the chemical potential of the same component in the coexisting fluid phase (vapour or

liquid) with specified molar compositions, $x^F$. In the case of the reference state being the ideal gas, Eq. 3-1 can be replaced by [70]:

$$\hat{f}_i^S(T,P) = \hat{f}_i^F(T,P,x^F) \qquad (3\text{-}2)$$

where the solid phase and fluid phase fugacities of component i ($\hat{f}_i^S$ and $\hat{f}_i^F$) can be found from Equations 3-3 and 3-4, respectively [65]:

$$\hat{f}_i^S(T,P) = \widehat{\varphi}_{0i}^{Sat}\left(T, P_i^{Sub}\right)\ P_{0i}^{Sat}(T)\ exp\left[\frac{v_{0i}^S}{RT}\left(P - P_{0i}^{Sat}(T)\right)\right] \qquad (3\text{-}3)$$

$$\hat{f}_i^F(T,P,x^F) = x_i^F \widehat{\varphi}_i^F(T,P,x^F)P \qquad (3\text{-}4)$$

where $P_{0i}^{Sat}(T)$ is the saturation/sublimation pressure of the solid forming component at the specified temperature *T*, $\widehat{\varphi}_{0i}^{Sat}\left(T, P_i^{Sub}\right)$ is the fugacity coefficient of the solid component at temperature *T* and the saturation pressure $P_{0i}^{Sat}$, $\widehat{\varphi}_i^F(T,P,x^F)$ is the fugacity coefficient of the component *i* in the fluid mixture of molar composition $x^F$ at the temperature *T* and pressure *P*, and $v_{0i}^S$ is solid molar volume of the component *i*.

In order to use Equations 3-2 through 3-4 for SLVE calculations, an appropriate EoS is selected alongside an equilibrium equation, which estimates the saturation/sublimation pressure of the solid forming component at the given temperature. In this work, Ping-Robinson equation of state (PR EoS) is used [71] as illustrated in appendix A**.**

### 3.3 Aspen Custom Modeler and models export

This section illustrates the basic steps used to program the code for the developed models into the ACM and then export it to the Aspen Plus environment.

1- A code that programs the developed models is written according to the ACM style. Figure 3-1 shows a simple example of the code used for predicting the SLV locus of the binary system $CH_4$-$CO_2$.

2- The ACM code is executed, and its predictions are collected and compared to experimental data published in the literature as discussed in the following chapters.

3- The ACM model is expanded to account for energy balance calculations. Figure 3-2 shows an example of a full model of the Solid-Vapor separation unit utilized in this work.

4- The ACM model is exported into the Aspen Plus environment as shown in Figure 3-3. The exported unit will appear in Aspen Plus as a standard separation unit (like the ones already built-in the original Aspen Plus environment), and thus the process flow sheet is constructed as usual.

```
Model CFZFlash
  // <parameter name> as <parameter type> (<default>, description:"<description>");
  // <variable name>  as <variable type> (default, <spec>, description:"<description>");
  // <submodel name>  as <model type> (<submodel variable> = <variable name>,...);
  // <structure name> as external <structure type>("<default instance>");
  // <port name>      as <Input or Output> <port type>;
  // <equation_name> : <expression1> = <expression2>;
  // Call (<output argument list>) = <procedure name>(<input argument list>);
  P as pressure (description:"Temperature", value:38.75, spec:Fixed);
  T as temperature (description:"Temperature", value:-88.43, spec:Free);

  Y(ComponentList) as molefraction (description:"Vapor Phase Mole Fraction ", value:1/size(ComponentList), spec:Free);
  X(ComponentList) as molefraction (description:"Liquid Phase Mole Fraction", value:1/size(ComponentList), spec:Free);
  Xs (ComponentList)as molefraction (description:"Solid Phase Mole Fraction", value:0, spec:Fixed);
  Psat as pressure (description:"Solid phase saturation pressure");
  PhiV(ComponentList) as fuga_vap (description:"Fugcity Coff Vapor Phase");
  PhiL(ComponentList) as fuga_liq (description:"Fugcity Coff Liquid Phase");
  h_in  as enth_mol (description:"Feed Enthlpy");
  h_Vi as enth_mol (description:"Vapor phase Enthlpy");
  h_Li  as enth_mol (description:"Liquid Phase enthalpy");
  h_Si as enth_mol (description:"Solid Phase Enthalpy");

  call (h_Vi) = pEnth_Mol_Vap (T, P, y) ComponentList;
  call (h_Li) = pEnth_Mol_Liq (T, P, X) ComponentList;
  call (h_Si) = pEnth_Mol_Sol (T, P, Xs) ComponentList;
  Call (PhiV) = pFuga_Vap( T, P, Y ) ComponentList;
  Call (PhiL) = pFuga_Liq( T, P, X ) ComponentList;
  Psat = 10 ^ (6.81228 - (1301.679/((T+273.15) - 3.494)));

  Eqn_Eql1: Y(["CH4"]) * PhiV(["CH4"]) = X(["CH4"])*PhiL(["CH4"]);
  Eqn_Eql2: Y(["CO2"]) * PhiV(["CO2"]) = X(["CO2"])*PhiL(["CO2"]);
  Eqn_Eql3: Xs(["CO2"]) * Psat = X(["CO2"])*PhiL(["CO2"])*P;

  Eqn_Xsum: Sigma(X) = 1;
  Eqn_Ysum: Sigma(Y) = 1;

  End
```

Figure 3-1: Example ACM code programmed to predict the SV locus of the $CH_4$-$CO_2$ binary system.

Figure 3-2: Full ACM model for the proposed SV separation unit.

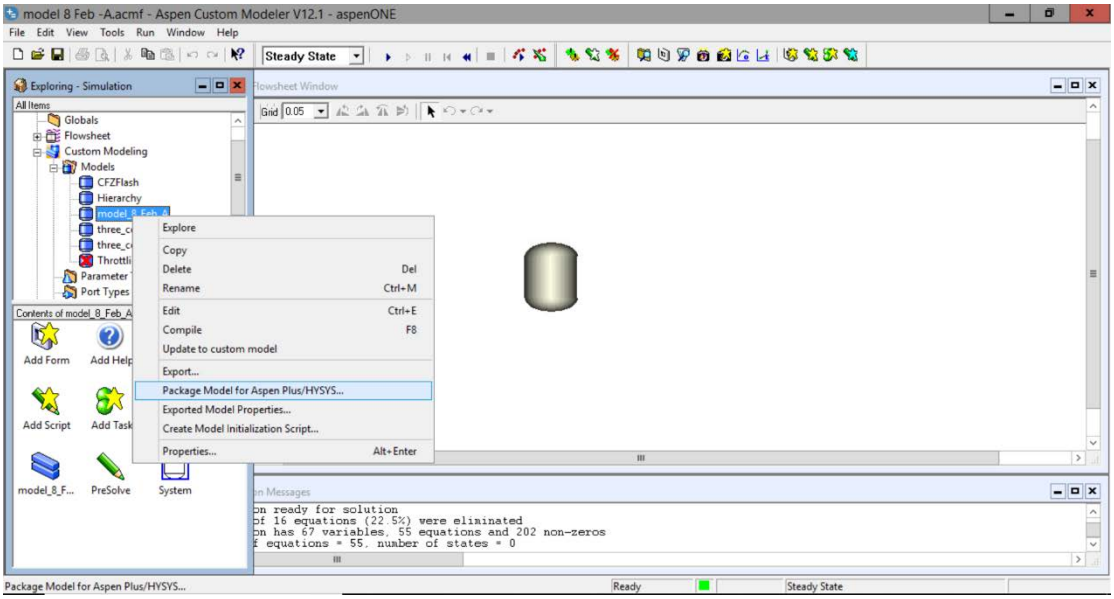


Figure 3-3: Exporting the ACM model into the Aspen Plus environment.

# CHAPTER 4: NATURAL GAS SYSTEM ($CO_2$-$CH_4$-$H_2S$)[5]

In this chapter the model suggested in the previous chapter was first used to describe the binary systems of $CH_4$-$CO_2$, $CO_2$-$H_2S$ and $CH_4$-$H_2S$; and was then expanded in a predictive manner to describe the ternary system of $CH_4$-$CO_2$-$H_2S$. The interaction parameters for each binary systems are optimized by comparing the model results to the experimental data available in the literature. While the ternary system results are tested for the solidification points of 5 different mixtures and compared to the experimental data available in the literature. Finally, the developed model results are compared to other models and suggested by other studies published in the literature.

The main objective of this chapter is construct phase diagrams for the binary and ternary components consisting the natural gas ($CO_2$-$CH_4$-$H_2S$).

## 4.1 Modeling of the binary and ternary systems consisting the natural gas

### 4.1.1 Modelling the Binary System of $CH_4$-$CO_2$

The SLVE phase equilibrium at the pressure-temperature (PT) locus curve of the $CH_4$-$CO_2$ system depends on estimating the fugacity of these two components in each phase. To do so, we employ the PR EoS (see section Appendix A) with the sublimation pressure equation of $CO_2$ obtained from Span and Wagner [72] as shown in Equation 4-3. The full model for calculating the fugacities of $CO_2$ would be:

[5] This chapter was taken from the published articles: H. Ababneh and S. Al-Muhtaseb, "An Empirical Correlation-Based Model to Predict Solid-Fluid Phase Equilibria and Phase Separation of the Ternary System CH4-CO2-H2S," J. Nat. Gas Sci. Eng., vol. 94, p. 104120, 2021, doi: https://doi.org/10.1016/j.jngse.2021.104120

H. Ababneh and S. A. Al-Muhtaseb, "A Review on the Solid-Liquid-Vapor Phase Equilibria of Acid Gases in Methane," Greenh. Gases Sci. Technol., vol. 12, no. 4, pp. 566–579, 2022, doi: 10.1002/ghg.2161.

$$\hat{f}_{CO_2}^{V} = y_{CO_2}\hat{\varphi}_{CO_2}^{V}P \quad (4\text{-}1)$$

$$\hat{f}_{CO_2}^{L} = x_{CO_2}\hat{\varphi}_{CO_2}^{L}P \quad (4\text{-}2)$$

$$\hat{f}_{CO_2}^{S} = x_{CO_2}\,\hat{\varphi}_{CO_2}^{Sub}\left(T, P_{CO_2}^{Sub}\right)\; P_{CO_2}^{Sub}\; exp\left[\frac{v_o^S}{RT}(P - P_{CO_2}^{Sub}\right] \quad (4\text{-}3)$$

$$\ln\left(\frac{P_{CO_2}^{Sub}}{P_t}\right) = \frac{T_t}{T}\left[-14.740846\left(1-\frac{T}{T_t}\right) + 2.4327015\left(1-\frac{T}{T_t}\right)^{1.9} + -5.3061778\left(1-\frac{T}{T_t}\right)^{2.9}\right] \quad (4\text{-}4)$$

where ($T_t = 216.592$ K, $P_t = 0.51795$ MPa) are triple point conditions of pure $CO_2$.

The fugacities of $CH_4$ can be obtained from:

$$\hat{f}_{CH_4}^{V} = y_{CH_4}\hat{\varphi}_{CH_4}^{V}P \quad (4\text{-}5)$$

$$\hat{f}_{CH_4}^{L} = x_{CH_4}\hat{\varphi}_{CH_4}^{L}P \quad (4\text{-}6)$$

At the SLVE locus, where the solid phase is assumed to consist of pure $CO_2$. Hence, the phase equilibrium equations for $CO_2$ are given by Equations 4-7 and 4-8.

$$\hat{f}_{CO_2}^{V} = \hat{f}_{CO_2}^{L} \quad (4\text{-}7)$$

$$\hat{f}_{CO_2}^{V} = \hat{f}_{CO_2}^{S} \quad (4\text{-}8)$$

whereas the phase equilibrium equation for $CH_4$ is given by

$$\hat{f}_{CH_4}^{V} = \hat{f}_{CH_4}^{L} \quad (4\text{-}9)$$

The accuracy of the model predictions depends on optimizing the interaction parameter ($k_{ij}$) within the EoS. Thus, several values for the interaction parameter of $CH_4$-$CO_2$ system were collected from the published literature. For example, $k_{ij}$= 0.1 (sourced from Nikolaidis et al. [65]), $k_{ij}$= 0.1187 (sourced from Stringari et al [73]), and $k_{ij}$= 0.12 (found in Nasir et al. [74]). The model predictions are compared to the experimental data found in Davis et al [41]. The model will be used to estimate the

pressure and the composition of each phase at the locus temperature, and the average squared error of these predictions is calculated according to Equation 4-10 [75].

$$Error = \frac{\Sigma\left(\frac{M_{Exp.}-M_{Calculated}}{M_{Exp.}}\right)^2}{N} \qquad (4\text{-}10)$$

where $M$ is the property (such as pressure or composition), and $N$ is the number of experimental data points. The $k_{ij}$ value that results in correlated binary data with the least error in pressure and composition (according to Equation 4-10) will be deemed as an optimum interaction parameter; and thus will be adopted for predicting the ternary system equilibria.

### 4.1.2 Modelling the Binary System of $CO_2$-$H_2S$

Similar to the $CH_4$-$CO_2$ system, the model is tested for the $CO_2$-$H_2S$ binary system at the SLVE locus, and the optimum interaction parameter is determined. At the SLVE locus for the $CO_2$ solidification in the binary system of $CO_2$-$H_2S$, the phase equilibrium equations for $CO_2$ are described by Equations 4-7 and 4-8; whereas the phase equilibrium equation for $H_2S$ is given by:

$$\hat{f}^V_{H_2S} = \hat{f}^L_{H_2S} \qquad (4\text{-}11)$$

where the fugacities of $CO_2$ can be estimated using Equations 4-1 to 4-4, and the fugacities of $H_2S$ are estimated from

$$\hat{f}^V_{H_2S} = y_{H_2S}\hat{\varphi}^V_{H_2S}P \qquad (4\text{-}12)$$

$$\hat{f}^L_{H_2S} = x_{H_2S}\hat{\varphi}^L_{H_2S}P \qquad (4\text{-}13)$$

Again, several values of the binary interaction parameter between $H_2S$ and $CO_2$ are utilized for correlating their binary phase equilibrium data that were collected from the published literature. Utilized values involve those reported in literature (such as $k_{ij}$ = 0.0974 sourced from Ramdin et al. [76], $k_{ij}$ = 0.099 sourced from Li [50], and $k_{ij}$ = 0.095 found in Chapoy et al. [49]), and others (i.e., $k_{ij}$ = 0.0101, $k_{ij}$ = 01050, $k_{ij}$ = 0.1100,

and $k_{ij}$ = 0.1200) that were tested to determine the optimum value for this interaction parameter. The optimum interaction parameter is determined by minimizing the error according to Equation 4-10.

### 4.1.3 Modelling the Binary System of $CH_4$-$H_2S$

In an independent study conducted by Lange et al. [45], they found a non-temperature dependent value for the interaction parameter ($k_{ij}$ =0.058) for the SLVE of the binary system $CH_4$-$H_2S$. This value was found to provide satisfactory description of the phase equilibria of the $CH_4$-$H_2S$ system from 70 K up to the critical temperature of $H_2S$. No other studies were found to report interaction parameters for this binary system. Thus, this interaction parameter value will be chosen as the starting point to find the optimum interaction parameter value between $CH_4$-$H_2S$ according to the aforementioned approach. For this binary system, there are two SLVE loci; the $SL_1VE$ locus and the $SL_2VE$ locus (where $L_1$ is the liquid phase that is rich with $CH_4$, while $L_2$ is the liquid phase that is rich with $H_2S$). These two loci meets at the quadruple point (QP) at which four phases are present, i.e., $SL_1L_2VE$.

At the $SL_1VE$ or $SL_2VE$ (i.e., when only one liquid phase is present), the phase equilibrium equations for $H_2S$ can be obtained from Equations 4-11 and 4-14.

$$\hat{f}_{H_2S}^{V} = \hat{f}_{H_2S}^{S} \qquad (4\text{-}14)$$

where the fugacities of $H_2S$ in the vapor and liquid phases are estimated from Equations 4-12 and 4-13, respectively; and the fugacity of $H_2S$ in the solid phase is obtained from Eq. 4-15 [77].

$$\hat{f}_{H_2S}^{S} = x_{s-H_2S}\hat{\varphi}_{H_2S}^{Sub}\left(T, P_{H_2S}^{Sub}\right)P_{H_2S}^{Sub} \qquad (4\text{-}15)$$

where the sublimation pressure of $H_2S$ ($P_{H_2S}^{Sub}$) can be estimated (in cm Hg) in terms of temperature (in Kelvin) as [77]

$$\log_{10}(P_{H_2S}^{Sub}) = 7.22418 - \frac{118.0}{T} - 0.196426\,T + 0.0006636T^2 \quad (4\text{-}16)$$

The equilibrium equation of $CH_4$ is presented in Equation 4-9, and the fugacities of $CH_4$ in the vapor and liquid phases can be estimated using Equations 4-5 and 4-6, respectively.

At the quadruple point (QP), the phase equilibrium equations for $CH_4$ are:

$$\hat{f}_{CH_4}^{V} = \hat{f}_{CH_4}^{L1} \quad (4\text{-}17)$$

$$\hat{f}_{CH_4}^{V} = \hat{f}_{CH_4}^{L2} \quad (4\text{-}18)$$

Whereas the phase equilibrium equation for $H_2S$ is:

$$\hat{f}_{H_2S}^{V} = \hat{f}_{H_2S}^{L1} \quad (4\text{-}19)$$

$$\hat{f}_{H_2S}^{V} = \hat{f}_{H_2S}^{L2} \quad (4\text{-}20)$$

$$\hat{f}_{H_2S}^{V} = \hat{f}_{H_2S}^{S} \quad (4\text{-}21)$$

### 4.1.4 Modelling the Ternary System ($CH_4$-$CO_2$-$H_2S$)

To study the SLVE for the ternary system ($CH_4$-$CO_2$-$H_2S$), an equilibrium stage separation unit will be modeled as described, where a feed stream consisting of the three components (in a specific overall composition) is separated at a certain temperature and pressure into three phases (vapor, liquid and solid). This ternary system ($CH_4$-$CO_2$-$H_2S$) can have two solid phases (namely, a $CO_2$ solid phase and an $H_2S$ solid phase) over certain ranges of temperature and pressure. It is to be noted that these two solid phases do not always coexist over the entire ranges of pressure and temperature. In this case, two different regions are determined: V-$S_1$-$S_2$ (vapor- solid $CO_2$-solid $H_2S$), and V-L-$S_1$ (vapor- liquid-solid $CO_2$); where $S_1$ and $S_2$ refer to the distinct solid phases of pure $CO_2$ and pure $H_2S$, respectively, and each of these two solid phases is assumed to consist of a pure component. It is to be noted that other possible phase combinations (e.g., V-L-$S_1$-$S_2$, V-L-$S_2$, L-$S_1$, L-$S_2$, L-$S_1$-$S_2$) are not present in the

studied ranges of pressure and temperature due to the inequality of chemical potentials of components in these phases at the specified conditions, which prevents their coexistence at equilibrium.

The system is modeled as an equilibrium stage separation unit, while assuming that the feed amount ($F$) with different feed compositions ($Z_i$). The material balance equations used for the first case (V-L-$S_1$) are:

Total Material Balance: $$F = V + L + S_{CO_2} \quad (4\text{-}22)$$

Material Balance on $CO_2$: $$Z_{CO_2}F = y_{CO_2}V + x_{CO_2}L + S_{CO_2} \quad (4\text{-}23)$$

Material Balance on $CH_4$: $$Z_{CH_4}F = y_{CH_4}V + x_{CH_4}L \quad (4\text{-}24)$$

The corresponding phase equilibrium equations for $CO_2$ are given in Equations 4-7 and 4-8, for $CH_4$ is given in Equation 4-9; and for $H_2S$ is given in Equation 4-11. Additionally, the fugacity values for $CO_2$, $CH_4$ and $H_2S$ can be obtained from Equations 4-1 through 4-3, 4-5 through 4-6 and 4-12 through 4-13, respectively.

For the second case (V-$S_1$-$S_2$), the vapour phase will be present with the absence of liquid phase; and each solid phase is assumed to consist of either pure $CO_2$ or pure $H_2S$. As a result, $CH_4$ will be present only in the vapour phase. The corresponding material balance equations are:

Total Material Balance: $$F = V + S_{CO_2} + S_{H_2S} \quad (4\text{-}25)$$

Material Balance on $CO_2$: $$Z_{CO_2}F = y_{CO_2}V + S_{CO_2} \quad (4\text{-}26)$$

Material Balance on $H_2S$: $$Z_{H_2S}F = y_{H_2S}V + S_{H_2S} \quad (4\text{-}27)$$

The corresponding equilibrium equations for $CO_2$ and $H_2S$ are given by Equations 4-8 and 4-14, respectively. Furthermore, the fugacity values of $CO_2$ in vapour and solid phases can be obtained from Equations S.1 and S.3, respectively; and those

of $H_2S$ in the vapour and solid phases can be obtained from Equations S.11 and S.14 respectively.

Three phase transition scenarios (the first appearance of vapour phase, the first appearance of $S_2$ phase and the first appearance of $S_1$ phase) are investigated. The region where the vapour phase first appears resembles a dew-point region. At that condition, the amount of the output vapour stream ($V$) in material balances is assumed to be zero; and the set of equations is solved at constant pressure to determine the temperature and compositions of other output streams. Similarly, to find the line where the phase $S_2$ appears (i.e., phase transition between V-$S_1$-$S_2$ and V-L-$S_1$), $S_{H_2S}$ was set to equal zero at the specified pressure. Finally, the condition when the solid phase (namely, $S_1$) starts to appear (i.e., the transition line between V-L-$S_1$ and V-L) was found by setting the value of $S_{CO_2}$ to be zero at the specified pressure. These scenarios allowed determining the various distinct phase regions for this ternary system.

After that, a number of points within each region are tested by solving the appropriate set of equations as presented previously. The performance of the equilibrium stage separation was evaluated by calculating the purity of $CH_4$ in the vapour phase, the recovery of $CH_4$ in the vapour phase, the recovery of $CO_2$ in the solid phase, and recovery of $H_2S$ in either solid or liquid phases. To test the model performance, the feed amount ($F$) is assumed to equal 1 mole; and three sets of feed compositions were investigated using this model at different conditions. The first set is: $Z_{CH4}$=0.80, $Z_{CO2}$=0.15, $Z_{H2S}$=0.05 (denoted as Case A), the second is: $Z_{CH4}$=0.80, $Z_{CO2}$=0.10, $Z_{H2S}$=0.10 (denoted as Case B), and finally $Z_{CH4}$=0.50, $Z_{CO2}$=0.30, $Z_{H2S}$=0.20 (denoted as Case C).

**4.2 Results and Discussion**

### 4.2.1 Optimization of Binary Interaction Parameters

The optimum interaction parameter ($k_{ij}$) for the binary system $CH_4$-$CO_2$ was obtained as described in section 4.1.1. Figure 4-1a compares the model predictions to the experimental SLVE pressure-temperature data available in the literature [41], while Figures 4-1b further compares the distribution of $CO_2$ between phases as a function of temperature. Table 3-1 shows the calculated average squared errors between model predictions at the specified $k_{ij}$ values and the experimental data in terms of pressure and $CO_2$ composition. It could be noticed that $k_{ij}$ = 0.1200 has the best results as it produces the lowest sum of errors, hence providing best correlation to the experimental data. Thus, it is recommended to use this interaction parameter value between $CH_4$ and $CO_2$ for any further calculations involving these two components. It could be concluded from Figure 4-1 that the model predictions can describe experimental data available in the literature very well, hence indicating the possibility of building over this ACM model for modelling other systems involving these two components, such as the ternary system $CH_4$-$CO_2$-$H_2S$.

Table 4-1: Effect of selected interaction parameter on the average squared errors in predicting SVLE pressures and $CO_2$ compositions in the binary system: $CH_4$-$CO_2$.

| $k_{ij}$ | Error in Pressure | Error in $x_{CO_2}$ | Error in $y_{CO_2}$ | Sum of errors |
|---|---|---|---|---|
| 0.1000 | 0.0017 | 0.0451 | 0.0668 | 0.1136 |
| 0.1187 | 0.0297 | 0.0115 | 0.0711 | 0.1123 |
| 0.1200 | 0.0010 | 0.0143 | 0.0668 | 0.0821 (min) |
| 0.1250 | 0.0023 | 0.0208 | 0.0715 | 0.0946 |

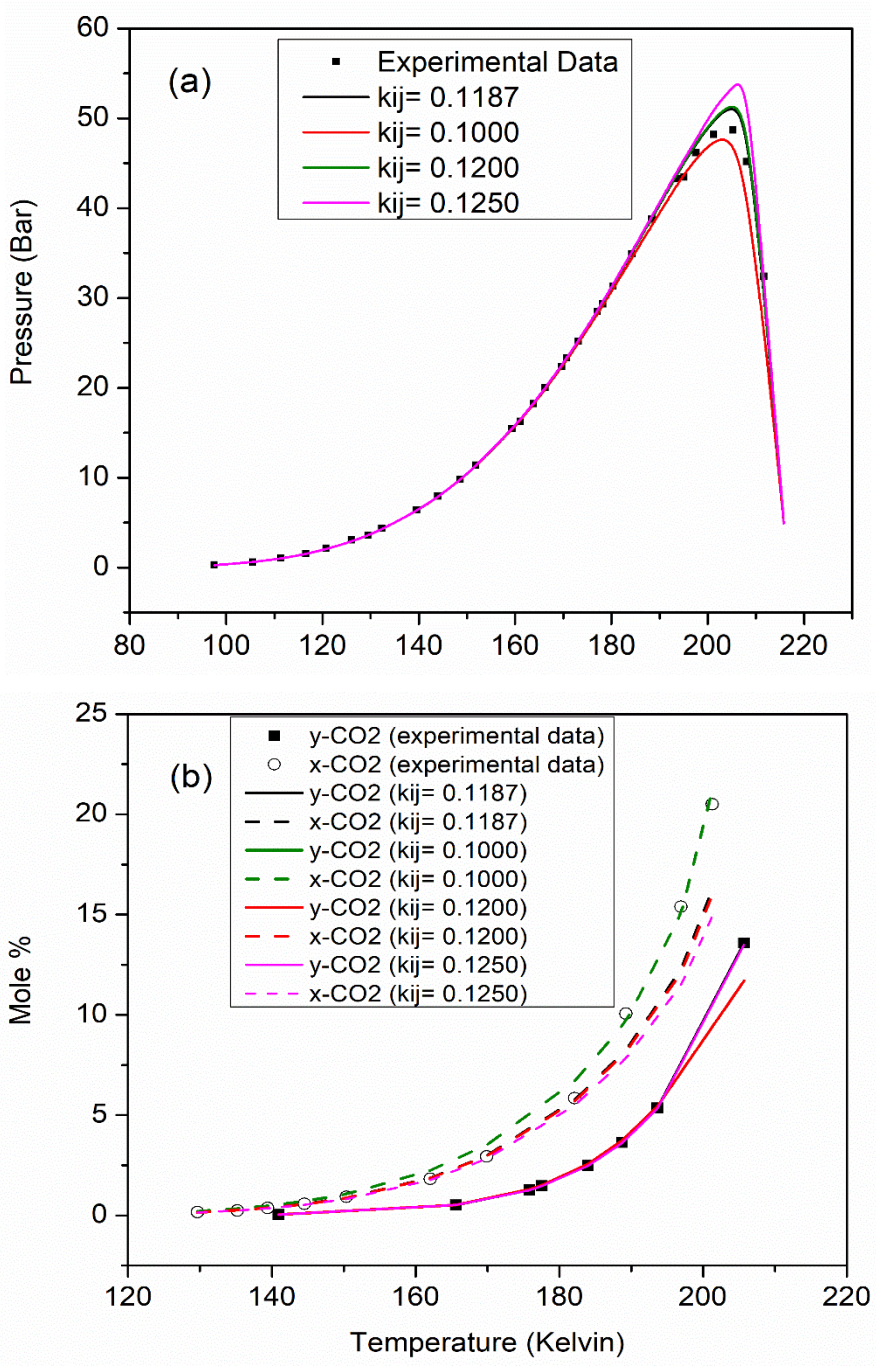


Figure 4-1: Comparison of model predictions and experimental data for the binary system of $CO_2$ and $CH_4$. Subfigures show the effect of temperature on equilibrium (a) pressure and (b) composition of $CO_2$ in each phase.

The optimum interaction parameter ($k_{ij}$) for the binary system $CO_2$-$H_2S$ was obtained as described in section 4.1.2. Table 3-2 shows the calculated average squared errors between model predictions at the specified $k_{ij}$ values and experimental data in

terms of pressure and $H_2S$ compositions [51]. From Table 3-2, it is concluded that the $k_{ij}$ =0.1100 produces the least sum of average squared errors when compared to the other values. Thus, $k_{ij}$ =0.1100 is considered as an optimum interaction parameter for this binary system, and will be adopted for further calculations involving the components $H_2S$ and $CO_2$. Once again, the model proved successful in predicting the SLVE Pressure-Temperature locus and compositions as seen in Figure 4-2.

Combining the results of the two binary systems ($CO_2$-$CH_4$ and $H_2S$-$CO_2$) produces Figure 4-3, which is calculated at the optimum interaction parameter found for each binary system. Figure 4-3 shows that the loci curves of the models meets at the estimated triple point of pure $CO_2$ (215.8 K, 4.9 bar), which is slightly different from the actual triple point of $CO_2$ (216.5 K, 5.2 bar) [78], which is slightly different from the actual triple point of $CO_2$ (216.5 K, 5.2 bar) [78].

Table 4-2: Effect of selected interaction parameter on the average squared errors in predicting SVLE pressures and $H_2S$ compositions in the binary system: $H_2S$-$CO_2$

| $k_{ij}$ | % Error in Pressure | %Error in $x_{H_2S}$ | %Error in $y_{H_2S}$ | %Sum of errors |
|---|---|---|---|---|
| 0.0950 | 0.26 | 4.06 | 11.47 | 15.79 |
| 0.0974 | 0.25 | 4.02 | 11.13 | 15.40 |
| 0.0990 | 0.25 | 4.02 | 10.9 | 15.17 |
| 0.1010 | 0.25 | 4.04 | 10.6 | 14.89 |
| 0.1050 | 0.24 | 4.18 | 10.10 | 14.52 |
| 0.1100 | 0.24 | 4.57 | 9.29 | 14.10 (min) |
| 0.1200 | 0.23 | 6.28 | 8.56 | 15.07 |

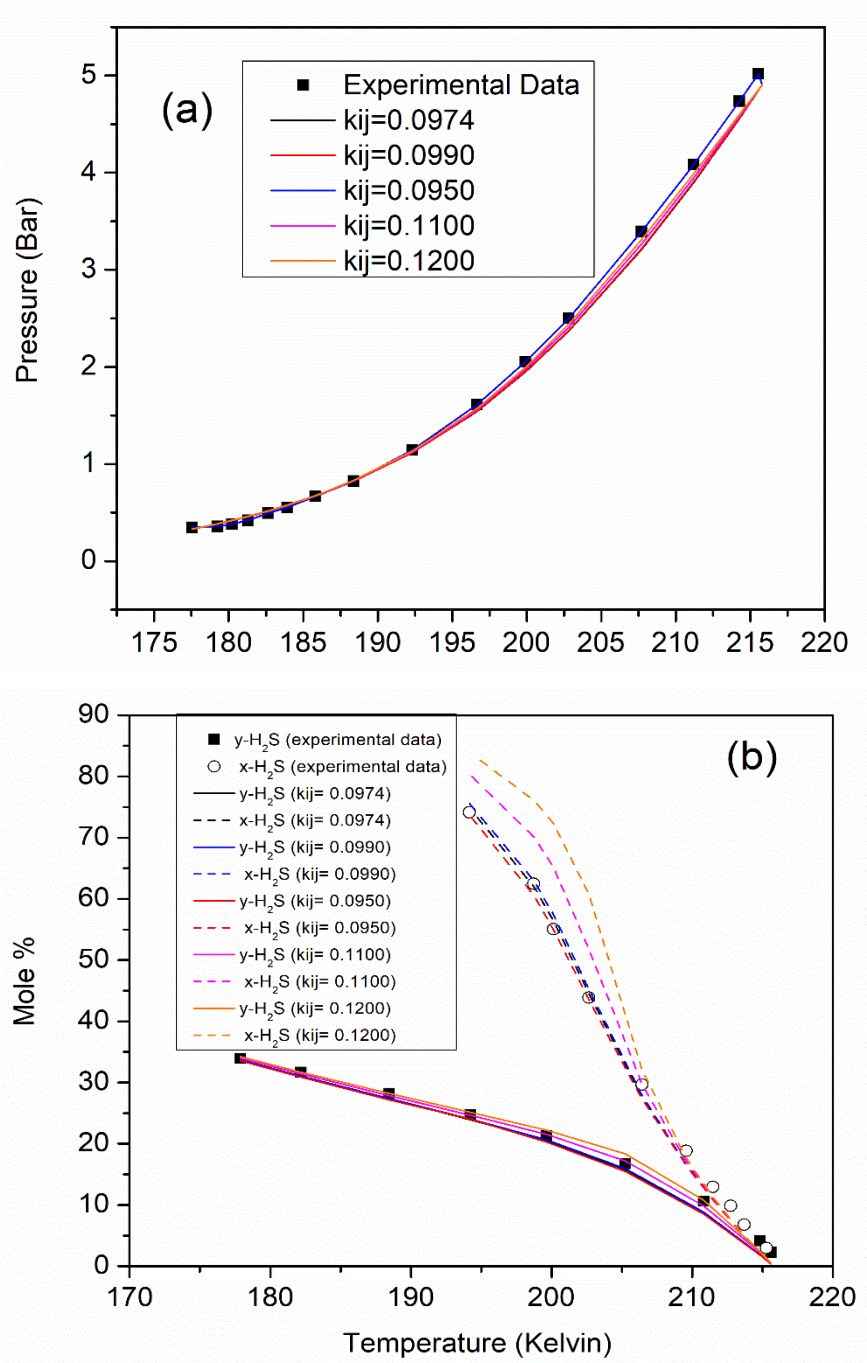


Figure 4-2: Comparison of model predictions and experimental data for the binary system of $CO_2$ and $H_2S$. Subfigures show the effect of temperature on equilibrium (a) pressure and (b) composition of $H_2S$ in each phase.

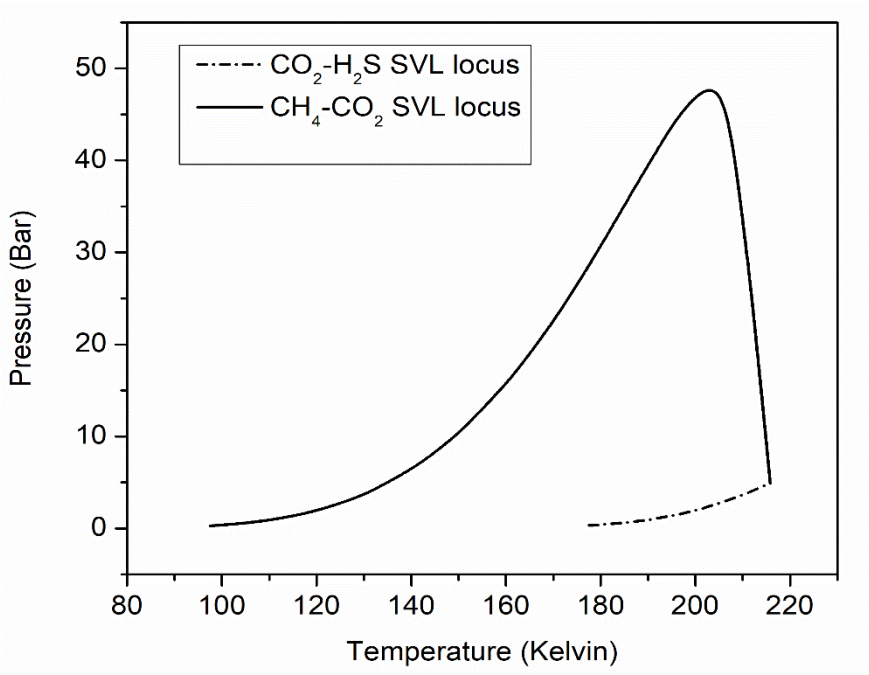


Figure 4-3: Combined SLVE P-T loci correlations for the binary systems of $CH_4$-$CO_2$ and $CO_2$-$H_2S$

The optimum interaction parameter ($k_{ij}$) for the binary system $CH_4$-$H_2S$ was obtained as described in section 4.1.3. Table 3-3 shows the calculated average squared errors between model predictions at the specified $k_{ij}$ values and experimental data [47] in terms of SLVE pressures and Quadruple point (QP) pressure. It is concluded that the $k_{ij}$ =0.058 results in the least sum of average squared errors. Thus, it is considered as an optimum interaction parameter for this binary system, and will be adopted for further calculations involving the components $H_2S$ and $CH_4$. Similar to the previous two systems, the model proved to be successful in predicting the SLVE Pressure-Temperature locus for this binary system as illustrated in Figure 4-4.

Table 4-3: Effect of interaction parameter on the average squared errors in predicting SLVE pressures and the quadruple point pressures in the binary system: $H_2S$-$CH_4$

| $k_{ij}$ | Error in QP | Error in $SVL_1E$ | Error in $SVL_2E$ | (Sum of errors)/3 |
|---|---|---|---|---|
| 0.100 | 9.351 | 1.002 | 287.248 | 99.200 |
| 0.070 | 11.790 | 0.864 | 221.656 | 78.103 |
| 0.058 | 15.664 | 1.824 | 155.581 | 57.690 (min) |
| 0.040 | 25.616 | 3.592 | 252.336 | 93.848 |

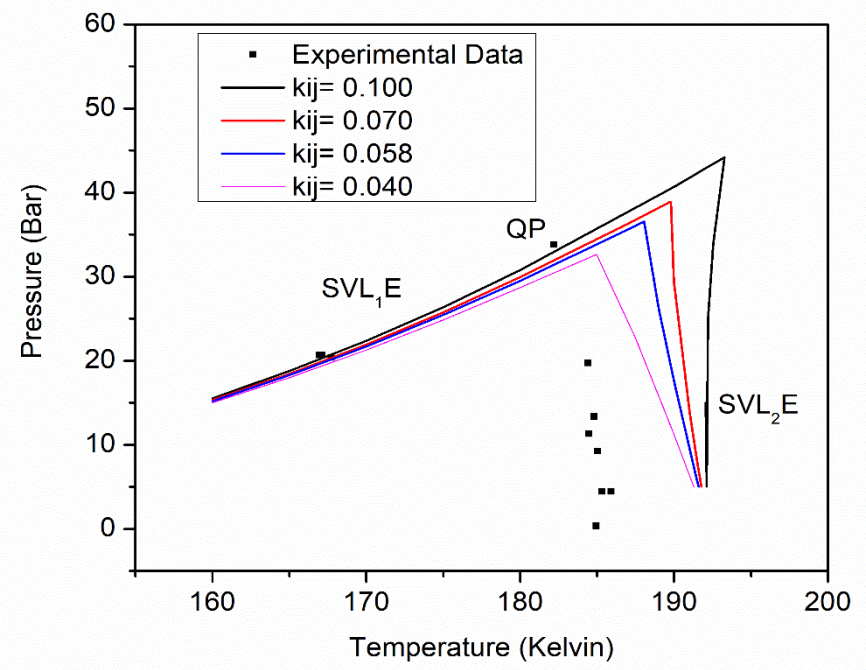


Figure 4-4: Comparison of model predictions and experimental data for the effect of temperature on equilibrium behavior of the binary system of $CH_4$ and $H_2S$. Symbols before and after QP correspond, respectively, to $SVL_1E$ and $SVL_2E$.

### 4.2.2 Modelling Results of the Ternary System: $CH_4$-$CO_2$-$H_2S$

Théveneau et al. [52] have used a visual synthetic experimental method to find the solidification point for five compositions of the ternary mixture $CH_4$-$CO_2$-$H_2S$. The

compositions of these mixtures are listed in Table 3-4. These data were also predicted in this work using the previously presented model with the optimized interaction parameters between each pair of components as determined in the previous section. The Mean Absolute Deviation (MAD) (Eq. 4-28) between the measured and predicted solidification temperatures is 2.86 K and the Mean Relative Deviation (MRD) (Eq. 4-29) is 1.44%, indicating that the model has successfully predicted the solidification temperature for a these mixtures.

$$MAD = \frac{1}{N}\sum\left|U_{cal} - U_{exp}\right| \qquad (4\text{-}28)$$

$$MRD = \frac{100}{N}\sum\left|\frac{U_{cal}-U_{exp}}{U_{exp}}\right| \qquad 4\text{-}29)$$

Where *U* is the property, *cal* is the value estimated by the model, and *exp* is the experimental data.

Table 4-4: Comparison between experimental and predicted temperatures of solidification for various compositions, and errors in predicted temperatures

| Mixture | $Z_{CH4}$ | $Z_{CO2}$ | $Z_{H2S}$ | P (MPa) | $T_{exp}$ (Kelvin) | $T_{pred}$ (Kelvin) |
|---|---|---|---|---|---|---|
| 1 | 0.7993 | 0.2007 | 0 | 2.224 | 209.80 | 213.03 |
| 2 | 0.7603 | 0.1899 | 0.0498 | 2.186 | 202.33 | 203.74 |
| 3 | 0.7192 | 0.1806 | 0.1002 | 1.848 | 196.85 | 200.05 |
| 4 | 0.6802 | 0.1701 | 0.1497 | 1.974 | 194.32 | 197.62 |
| 5 | 0.6395 | 0.1604 | 0.2001 | 2.123 | 192.26 | 195.43 |
| MAD (K) | | | | 2.86 | | |
| MRD (%) | | | | 1.44% | | |

Since the model has proved to be sufficiently accurate and reliable, the model was run to study the SLVE and separation performances for the 3 different of

compositions (cases A, B and C) as mentioned in section 4.1.4 and listed in Table 3-5. Table 3-5 also indicate that the corresponding composition ratios of $CO_2/CH_4$, $H_2S/CH_4$ and $H_2S/CO_2$ follow the trends B<A<C, A<B<C and A<C<B, respectively. The phase diagrams (Pressure-Temperature diagram) for the three cases are shown in Figures 4-5a, 3-5b, and 3-6c respectively; while Figure 4-6d shows the overlaid phase diagrams of three cases on the same graph. Figures 4-6a, 4-6b, and 4-6c also show the points tested to collect data for compositions, recovery, and products distribution.

Table 4-5: $CO_2/CH_4$, $H_2S/CH_4$ and $H_2S/CO_2$ ratios for each case of the feed.

| Case | $Z_{CH4}$ | $Z_{CO2}$ | $Z_{H2S}$ | $CO_2/CH_4$ | $H_2S/CH_4$ | $H_2S/CO_2$ |
|---|---|---|---|---|---|---|
| A | 0.80 | 0.15 | 0.05 | 0.1875 | 0.0625 | 0.333 |
| B | 0.80 | 0.10 | 0.10 | 0.1250 | 0.1250 | 1.000 |
| C | 0.50 | 0.30 | 0.20 | 0.6000 | 0.4000 | 0.667 |

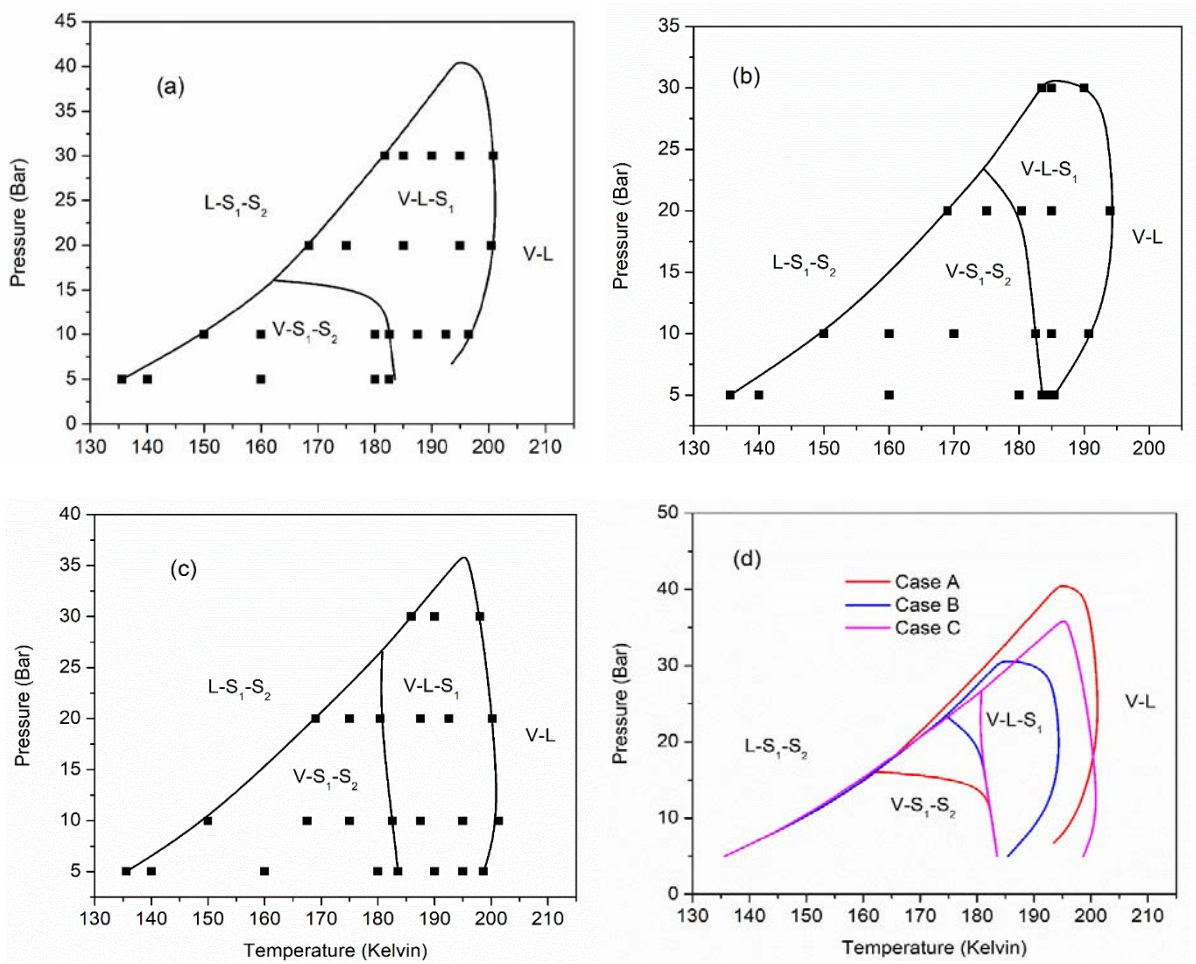


Figure 4-5: Pressure-Temperature phase diagrams for (a) Case A, (b) Case B, (c) Case C, and (d) comparison of the three cases. Symbols (■) indicate points tested to collect data for compositions, recovery, and products distribution for the cases listed in Table 3-5.

By studying the phase diagrams for the three cases, it could be noticed that the line between the L-$S_1$-$S_2$ and V-$S_1$-$S_2$/V-L-$S_1$ regions (indicating the first appearance of the vapour phase) follows the same trend for the three cases till the point where the three regions (L-$S_1$-$S_2$, V-$S_1$-$S_2$, and V-L-$S_1$) regions meet, which indicates the point where the four phases (V-L-$S_1$-$S_2$) coexist. After that point the lines behave differently for each case. From Figure 4-5d and Table 4-5, it could be concluded that increasing the ratio of $H_2S/CH_4$ in the feed (which follows the sequence A<C<B) results in a smaller V-L-$S_1$ region (that follows the sequence A>C>B); with a lower temperature for coexistence of these four phases; where this temperature follows the sequence A<B<C (following the $H_2S/CH_4$ composition ratio). Similarly, the trend of the V-L-$S_1$/V-L equilibrium lines (which resemble the melting condition of the solid phase) trend is governed by the $H_2S/CO_2$ ratio, where it can be seen that the melting temperatures sequence is (B<C<A); which follows the opposite sequence of $H_2S/CO_2$ ratio (B>C>A). In other words, lower $H_2S/CO_2$ ratios would move the curve to the right (higher melting temperature at the same pressure). The $H_2S/CH_4$ ratio (which follows the order A<B<C) also impacts the V-$S_1$-$S_2$/ V-L-$S_1$ equilibrium line. Higher $H_2S/CH_4$ ratios in the feed would move the line upward (vertically) and make the V-$S_1$-$S_2$ region larger. This phenomenon could be explained by the fact that $H_2S$ solidification temperature is higher than that of $CH_4$, thus increasing its amount in the feed would move the line to higher temperature.

The effect of temperature on vapour phase compositions of $CH_4$ and $CO_2$ at different pressures are shown in Figures 4-6a, 4-6b and 4-6c for cases A, B and C, respectively. In general, higher temperatures result in reducing $y_{CH_4}$, and increasing $y_{CO_2}$ and $y_{H_2S}$. However, higher pressures at the same temperature increases $y_{CH_4}$ and reduces $y_{CO_2}$ and $y_{H_2S}$. Overall, highest $CH_4$ purities in the vapour phase can be

obtained when reducing temperature and or pressure. Furthermore, the effect of feed composition has a negligible effect on $y_{CH_4}$ and $y_{CO_2}$ at the same temperature and pressure.

The effects of temperature and pressure on the liquid phase composition are shown in Figure 4-7. On one hand, temperature has insignificant impact on $x_{CH_4}$ except at high pressure (30 Bar), where high temperature would result in reducing $x_{CH_4}$ significantly. On the other hand, increasing the pressure at constant temperatures increases $x_{CH_4}$. Furthermore, $x_{CO_2}$ and $x_{H_2S}$increase when increasing either pressure or temperature. Furthermore, it seems that the feed composition has no significant impact on the $x_{CH_4}$ value, while increasing the $H_2S/CH_4$ ratio (which follows the sequence A<B<C) will results in higher $x_{CO_2}$ and lower $x_{H_2S}$ at the same pressure and temperature. To study the performance of the equilibrium stage separation; the effects of temperature and pressure on the recovery of $CH_4$ in the vapour phase, the recovery of $CO_2$ in the solid phase, and the recovery of $H_2S$ in the liquid/solid phases are investigated as shown in Figures 4-8 and 4-9, and 4-10, respectively. The recovery of a component in a certain phase is calculated as the ratio of the moles of that component in the specified phase relative to the moles of that component in the feed mixture.

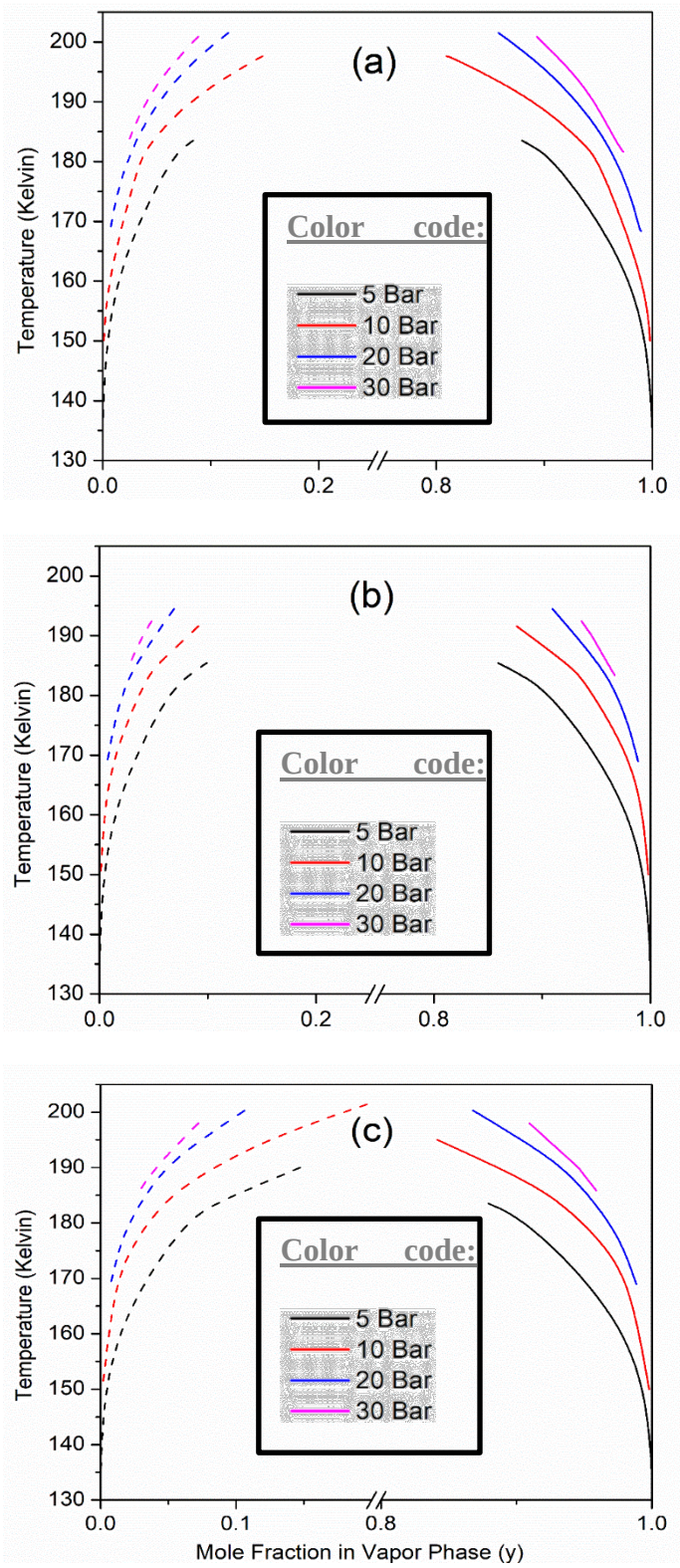


Figure 4-6: Effects of temperature and pressure on the vapor phase compositions of $CH_4$ (solid lines) and $CO_2$ (dashed lines) in Cases (a) A, (b) B and (c) C. Different colors indicate pressure values as illustrated in the legends.

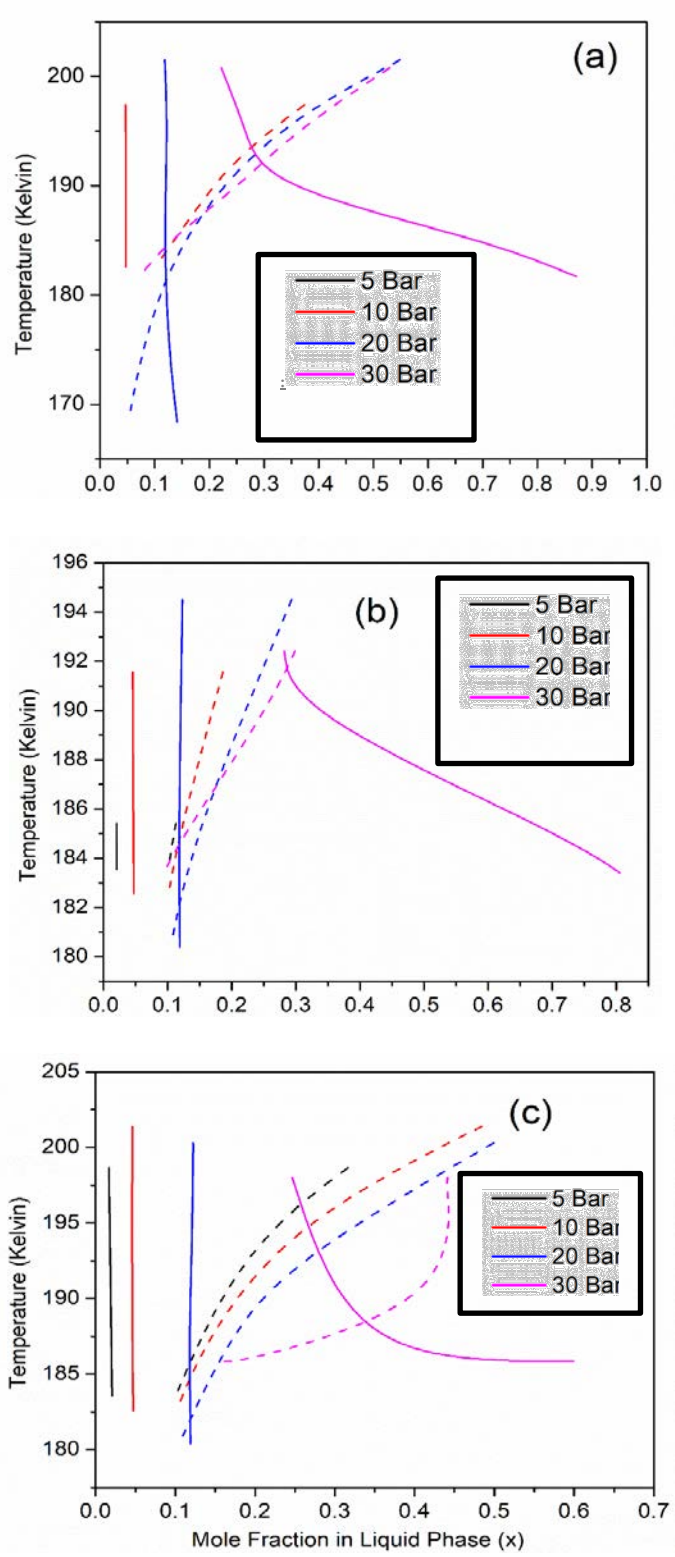


Figure 4-7: Effects of temperature and pressure on the liquid phase compositions of $CH_4$ (solid lines) and $CO_2$ (dashed lines) in Cases (a) A, (b) B and (c) C. Different colors indicate pressure values as illustrated in the legends.

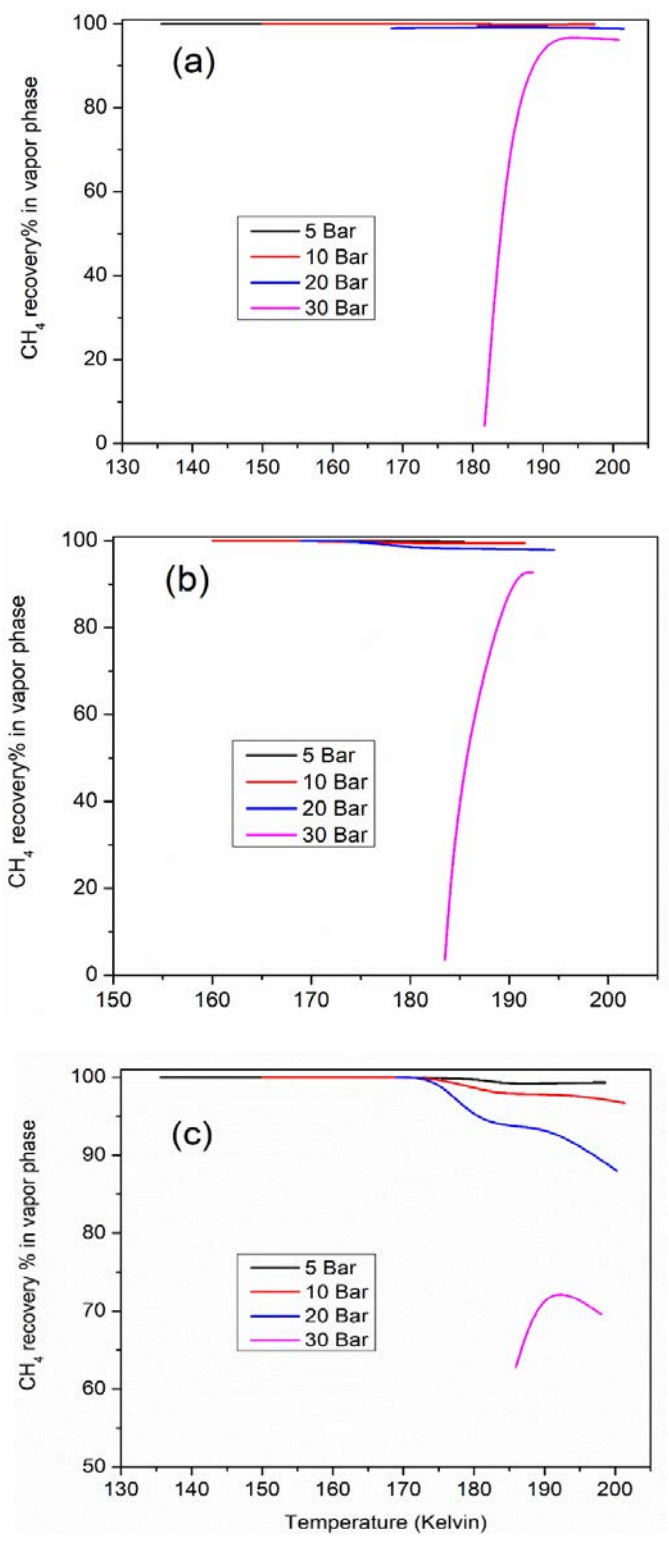


Figure 4-8: Effects of temperature and pressure on the vapor-phase recovery (%) of $CH_4$ in Cases (a) A, (b) B and (c) C. Different colors indicate pressure values as illustrated in the legends.

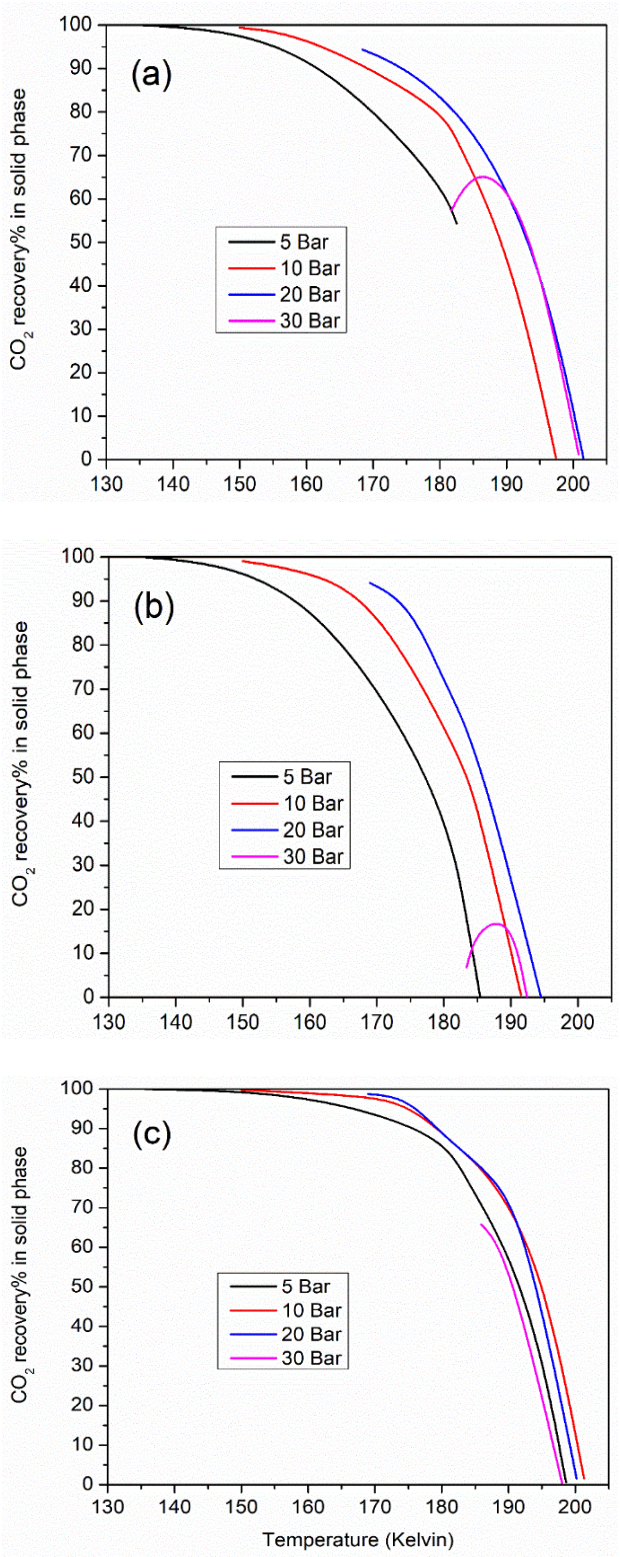


Figure 4-9: Effects of temperature and pressure on the solid-phase recovery of $CO_2$ in Cases (a) A, (b) B and (c) C. Different colors indicate pressure values as illustrated in the legends.

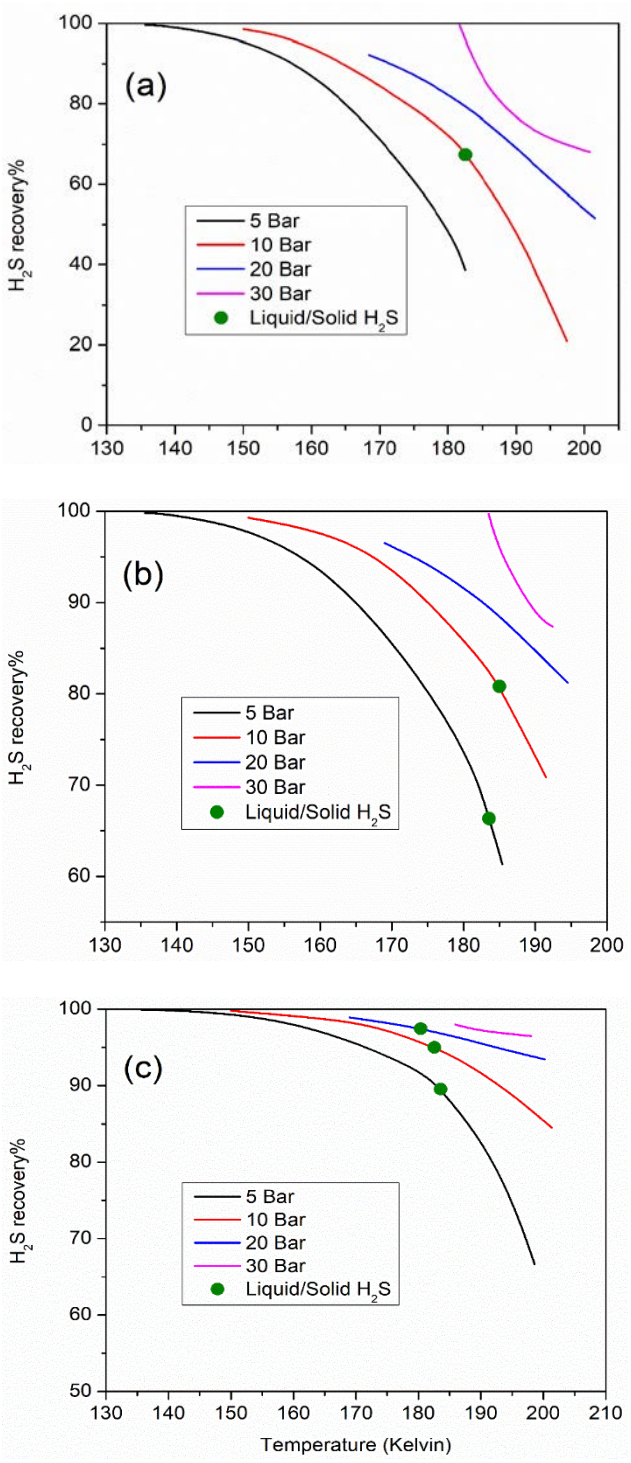


Figure 4-10: Effects of temperature and pressure on the recovery of $H_2S$ in solid and liquid phases in Cases (a) A, (b) B and (c) C. Symbols (●) indicate the transition points between solid and liquid phases at each pressure. Different colors indicate pressure valu

Figure 4-8 shows that the $CH_4$ recovery in the vapor phase does not change significantly with operating temperatures and pressures; except at high pressure (30 Bar) and low temperature (<190 K); where it drops to ~0% at ~180K. This could be attributed to the fact that the vapor phase amount drops significantly at these conditions as seen later in Figure 4-11, despite the fact that that $y_{CH_4}$ increases with the increase in temperature and pressure. Overall, the $CH_4$ recovery in the vapor phase exceeded 90% in all cases expect the one mentioned above, and will be 100% in the operating region of $VS_1S_2$ . The feed composition has a minimal impact on the $CH_4$ recovery in the $VS_1S_2$ region (low temperatures and pressures); whereas in the $VLS_1$ region, increasing the $H_2S$ ratio in the feed will reduce the recovery of $CH_4$ in the vapor phase.

Figure 4-9 shows that the $CO_2$ recovery in the solid phase decreases when increasing temperatures. However, at a constant temperature, it increases when increasing in the operating pressure up to pressure of 20 bar, after which the $CO_2$ recovery will decrease. Having more $CO_2$ in the feed (higher $CO_2$ /$CH_4$ ratio) will improve the $CO_2$ recovery in the solid phase noticeably at the same operating conditions.

Figure 4-10 illustrates the $H_2S$ recovery in the three studied cases in liquid and solid phases. Overall, it is clear that the $H_2S$ recovery increasing when reducing the operating temperature and/or increasing the operating pressure. Therefore, higher operating pressures will improve the separation of both $CO_2$ (in the solid phase) and $H_2S$ (in solid and liquid phase) but it will decrease $CH_4$ recovery in the vapor phase. Thus, it is important to determine the priorities in separation to determine the desired separation conditions. The feed composition has no clear impact on the $H_2S$ recovery in the liquid phase. However, the model predictions indicate that higher $H_2S/CH_4$ ratios in the feed will improve the recovery of $H_2S$ in the solid phase. In general, the best

region to separate the ternary system components can be the region of $VS_1S_2$ at the highest possible pressure and temperature.

Figure 4-11 illustrates the impact of temperature and pressure on the *V/F* and $S_{CO_2}/F$ phase ratios resulting from each of the studied cases. Increasing the temperature will increase *V/F* ratio, but it will decrease $S_{CO_2}/F$, $S_{H_2S}/F$ and *L/F* phase ratios. The relationship between the pressure and the produced phase ratios is opposite; increasing pressure lowers the *V/F* ratio and increases the $S_{CO_2}/F$, $S_{H_2S}/F$ and *L/F* phase ratios. Increasing the $CO_2/CH_4$ ratio in the feed will raise the produced $S_{CO_2}/F$ ratio (i.e., it will follow the sequence B<A<C) . Similarly, increasing the $H_2S/CH_4$ ratio will increase the produced $S_{H_2S}/F$ ratio (i.e., it will follow the sequence A<B<C). Figure 4-11c shows that case C has the lowest *V/F* ratio compared to other two cases at similar operating conditions, this might be explained by the lowest $CH_4$ composition in the feed compared to the other two cases (0.5 vs. 0.8). Furthermore, there was no clear relation between the feed compositions and the produced *L/F* phase ratios.

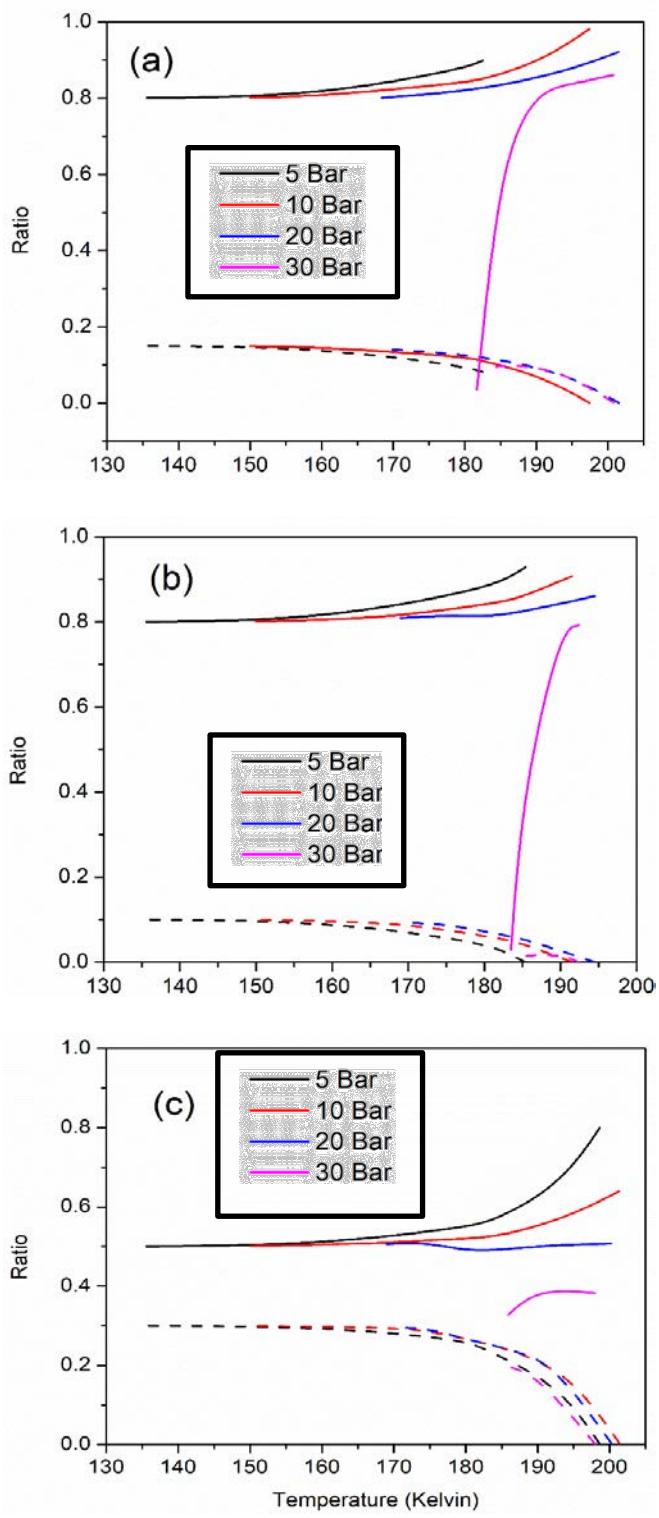


Figure 4-11: Effects of temperature and pressure on the V/F and $S_{CO2}$/F phase ratios (solid and dashed lines, respectively) in Cases (a) A, (b) B and (c) C. Different colors indicate pressure values as illustrated in the legends.

### 4.3 Comparison with other modeling approaches for binary system $CH_4$-$CO_2$

#### 4.3.1 Coupling EoS with specific models of solid phase fugacity approach

Nikolaidis et al. [65] have used an empirical correlation model to represent the equilibrium of the $CH_4$-$CO_2$ system. At equilibrium, the solid-phase fugacity of any compound equals the fugacity of that compound in the two coexisting fluid phases, as mentioned in Equation 2. Where the solid phase and fluid (vapor or liquid) phase fugacities of component *i* ($\hat{f}_i^S$ and $\hat{f}_i^F$, respectively) can be found from Equations 3 and 4, respectively; and the solid phase consists of pure component *i*.

To utilize Equations 2-4, Nikolaidis et al. [65] used three different equations of state (EoS) for determining the fugacities of vapor and liquid phases; namely, the Peng-Robinson (PR) EoS, Soave-Redlich-Kwong (SRK) EoS, and the Perturbed-Chain Statistical Associating Fluid Theory (PC-SAFT) EoS. Each of these equations included an interaction parameter between $CO_2$ and $CH_4$, $k_{ij}$, that was altered to optimize the model estimations of the experimental data. Overall, it was found that utilizing the PR EoS with $k_{ij}$=0.100 resulted in the least error of model estimations compared to the experimental data [38][41], with an average absolute deviation (AAD) (as defined in Eq. 4-4) of 2.19%. Figure 4-12a shows their estimated SLVE locus as generated using the PR EoS against experimental data [38][41]. To avoid crowding, only the data from Davis et al. [41] and Donnelley and Katz [38] were presented in Figure 4-12 since they cover the widest ranges of temperatures and pressures.

$$\%AAD = \frac{100}{N}\sum_{i=1}^{N}\left|\frac{P_i^{\text{calculated}} - P_i^{\text{experimental}}}{P_i^{\text{experimental}}}\right| \qquad (4\text{-}30)$$

where *N* is the number of experimental data points.

Yang et al. [79] studied the SLVE behaviour of this system by combining the PR EoS with Eq. 4-31 to find the fugacities of fluid and solid phases, receptively. They found that the optimum value for the interaction parameter $k_{ij}$ is 0.123, which is similar

to the value found by Ababneh and Al-Muhtaseb. However, the study of Yang et. al. covered a limited range of temperature (170-202 Kelvin) for the SLVE equilibrium. Their model predictions are compared to the experimental data [38][41] in Figure 4-12b.

$$ln\varphi^{S}_{pure} = ln\left(\varphi^{L}_{pure}\right) - \frac{\Delta H_f}{RT_m}\left[\frac{T_m}{T} - 1\right] + \frac{\Delta c_p}{R}\left[\frac{T_m}{T} - 1 + ln\left(\frac{T}{T_m}\right)\right] - \frac{\Delta v(P-P_m)}{RT} \quad (4\text{-}31)$$

where $R$ is the universal gas constant, $T$ is temperature, $\varphi^{L}_{pure}$ is the fugacity coefficient of the pure component in the liquid phase, and $P_m$ is the reference pressure (triple point pressure for $CO_2$). For a pure component at $P_m$, $T_m$ is the melting temperature, $\Delta H_f$ is the enthalpy of fusion, $\Delta c_p$ is the change of the heat capacity upon the transition from the solid phase to liquid phase; and $\Delta v$ is the change in molar volume upon transition from the solid phase to the liquid phase.

Riva et al. [4] proposed to calculate the solid phase fugacity of $CO_2$ by Eq. 4-32 and 4-33. This model is based on the numerical continuation method (NCM) of Rodriguez-Reartes et al. [80]. The AAD of the corresponding predictions when compared to the experimental data was found to be 1.94% [41]. Figure 4-12a compare the model predictions with experimental data [38] [41].

$$\hat{f}_i^S(T, v_0) = \hat{f}_i^L(T, 1, v_0)\exp(U) \quad (4\text{-}32)$$

$$U(T,P) = \frac{\Delta v^{S-L}}{RT}\left[-1.0819\times10^{-9}\left(1-\frac{T_t}{T}\right) + 3.5919\times10^{-6}\left(\frac{T_t}{T} - 1 + \ln\frac{T}{T_t}\right) + 4.2722\times10^{-6}\left(\frac{T}{2T_t} - 1 + \frac{T_t}{2T}\right) + \frac{T_t}{T}(\mathrm{P} - P_t)\right] \quad (4\text{-}33)$$

where $v_0$ ($m^3$/mol) is the molar volume of $CO_2$ in the hypothetical subcooled liquid state at T (Kelvin) and P (MPa). Furthermore, $T_t$ and $P_t$ are the triple-point temperature (in Kelvin) and pressure (in MPa); and $\Delta v^{S-L}$ is the solid−liquid molar volume difference of $CO_2$ (in $m^3$/mol).

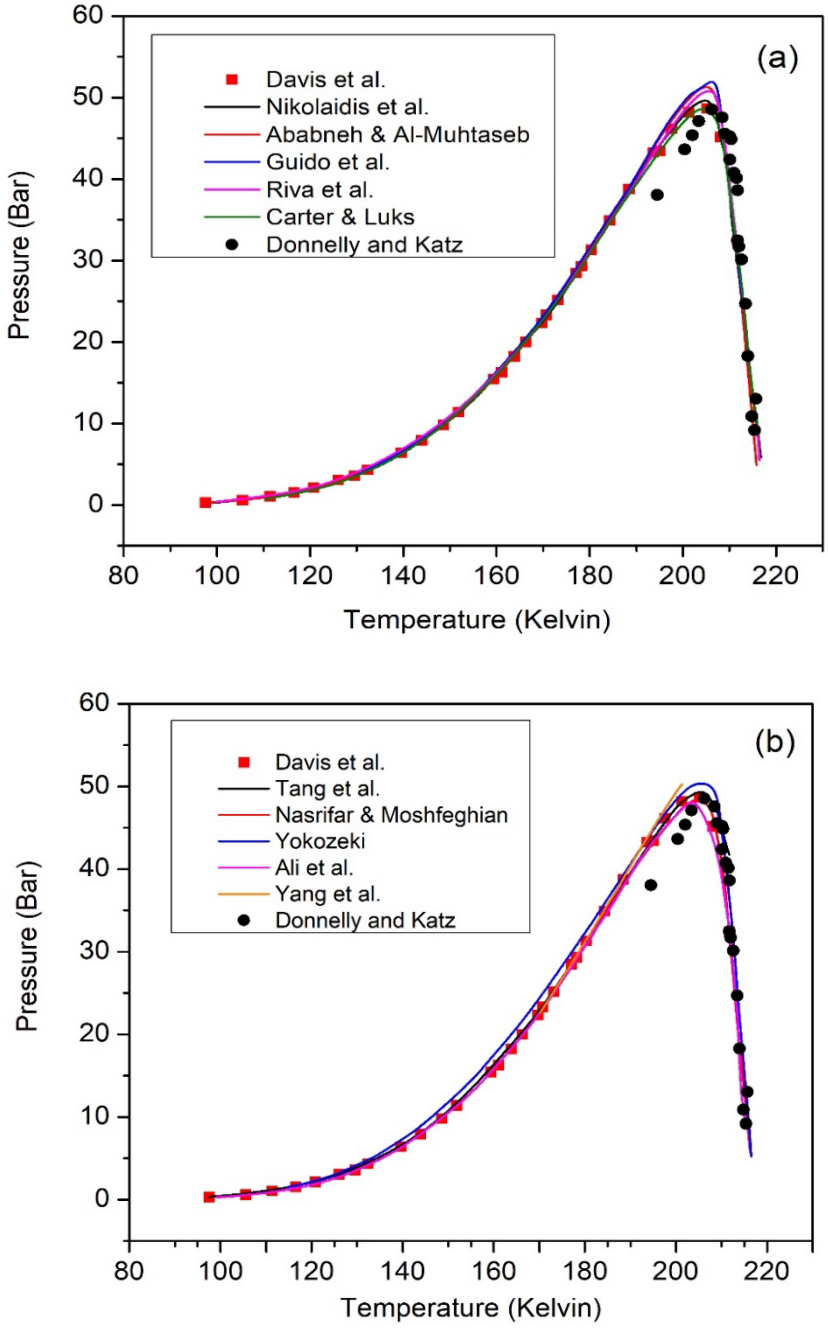


Figure 4-12: Comparison between models predictions (lines) with laboratory data (symbols) [38] [41] for the SLVE of the system $CH_4$-$CO_2$ system. Comparisons are divided between two subfigures to avoid overcrowding (a) [41] [65][23][81][4][82] (b) [83][84][85] [69].

Carter and Luks used a mathematical artifice to predict the solid $CO_2$ fugacity, and it was combined with the SRK EoS to find the SLVE locus [82]. The mathematical

artifice was developed by Prausnitz et al. [86] as shown in Eq. 4-34. The interaction parameter $k_{ij}$ in the EoS was varied between 0.10 and 0.13, and the results were compared to experimental data [41][38] as shown in Figure 4-12a.

$$\ln\frac{f}{f_s} = \frac{(H-H_s)-(H-H_{s,t})}{RT} - \frac{(S-S_t)-(S-S_t)}{R} \qquad 4\text{-}34)$$

where the subscripts *s* and *t* indicate the solid phase and triple point, respectively. *S* is the entropy, and *f* is the fugacity of liquid or gas phase of the pure component.

Similarly, Guido et al. [81] proposed a method based on each of the PR and SRK equations of state to predict the SLVE. Eq. 4-35 was used to calculate the fugacity of the solid $CO_2$ phase starting from the liquid phase fugacity. Their SLVE locus predictions (using the SRK EoS) are shown in Figure 4-12a.

$$\ln\frac{f^S(T,P)}{f^L(T,P)} = \frac{\Delta h_m}{RT_m}\left(1-\frac{T_m}{T}\right) - \frac{\Delta C_P(T_m-T)}{RT} - \frac{\Delta C_P}{R}\ln\frac{T_m}{T} \qquad (4\text{-}35)$$

where $\Delta h_m$ is the enthalpy change of melting, $\Delta C_P$ is the change of heat capacity between liquid and solid phases. Superscripts *s* and *L* indicate the solid and the liquid phases, respectively; and subscript *m* denotes the melting point.

Tang et al. estimated the solid $CO_2$ fugacity by first calculating the minimum Gibbs free energy ($g$) by an algorithm that involves a stability variable of vapour or liquid phases, which was developed using composition-independent correlations of solid−vapour and solid−liquid equilibria as the initial estimation for the phase fraction, and then plugging its value in Eq. 4-36 [83]; where the superscripts *s*, and *0* represent the solid and ideal gas phases, respectively. The resulted SLVE locus curve compared to the experimental data [38][41] , with an AAD of 1.98%, is also shown in Figure 4-12b.

$$f^s = f^0 exp\left[\frac{g^s-g^0}{RT}\right] \qquad (4\text{-}36)$$

Nasrifar and Moshfeghian developed a relation for the solid fugacity of $CO_2$ based on the triple point of carbon dioxide as seen in Eq. 4-37 [84]. This equation, coupled with the Nasrifar-Bolland (NB) EoS, was used to predict the SVE and SLVE loci for $CH_4$-$CO_2$ system. Figure 4-12b shows the results obtained by the model compared to the data by Davis et al.[41] and Donnelley and Katz [38] .

$$f^s(T,P) = f^s(T_t,P_t)\ exp\left[\frac{v^s(P-P_t)}{RT} - \frac{\Delta H_{sub}}{RT}\left(1-\frac{T}{T_t}\right)\right] \qquad (4\text{-}37)$$

where $v^s$is the molar volume of the solid phase and $\Delta H_{sub}$is the enthalpy change at sublimation.

### 4.3.2 Using EoS for vapor, liquid and solid phases approach

Yokozeki proposed an analytical EoS that is capable of representing the three phases: vapor, liquid, and solid [85]. Eq. 4-38 shows the pressure explicit form of this equation.

$$P\ (T,v) = \frac{RT}{v-b}\left(\frac{v-d}{v-c}\right)^k - \frac{a}{v^2+qbv+rb^2} \qquad (4\text{-}38)$$

where *c*, *b*, *a* are the liquid covolume, the solid covolume, and a parameter of attractive forces between molecules, respectively; while *d*, *k*, *q* and *r* are fitting parameters. While the results of Yokozeki were in good agreement with the experimental pressure-temperature locus data [41] as seen in Figure 4-12b, the issue with this model is that its predictions assume the presence of methane (up to 3%) in the solid phase, which is unrealistic. Furthermore, Yokozeki's model [85] has successfully described the experimental composition data of Davis et al. [41] as seen in Figure 4-13. However, there is an apparent deviation between the model predictions and experimental data at high temperatures, which could be explained by the fact the model assumes a presence of methane in the solid phase, even at higher temperatures; thus altering the model calculations for the other two phases. On the other hand, the model developed in this

study resulted in better predictions for the experimental data in the vapor phase as shown in Figure 4-13, which could be attributed to their assumption that the solid phase consists of pure $CO_2$, in agreement with experimental observations. On the other hand, both model showed good agreemt with experimental data in the liquid phase.

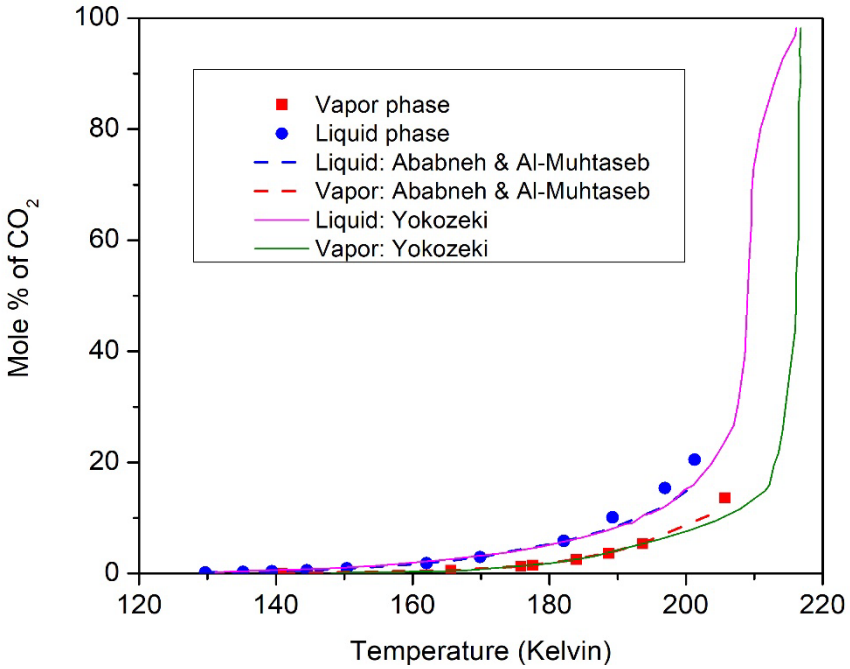


Figure 4-13: Model predictions (lines) compared to experimental data (symbols) [41] for the distribution of $CH_4$ and $CO_2$ in the liquid and vapor phases [23][85].

### 4.3.3 Using artificial neural networks (ANN)

Ali et al. [69] utilized a different approach to predict the SLVE locus for the $CH_4$-$CO_2$ binary system. An artificial neural network (ANN) was developed by the following procedure: Data collection and pre-processing, creating and optimizing the ANN design, training the ANN using the previously collected data sets and finally comparing predictions to the experimental data for validation. When compared to Davis et al data [41], the ANN predictions resulted in an AAD% of 0.1447% as seen in Figure 4-12b. While the ANN had excellent results, it is seen as a unnecessary tool in the presence of simpler thermodynamics models, which are able to produce similar

results. The complication of ANN could be a more useful technique in case of complicated systems, which cannot be described easily by simple mathematical models. However, in this case it does not appear to make a case for itself. Table 3-6 compares the model AAD values to the experimental data.

Table 4-6: Comparison between the model AAD values for the different studies predicting SLV locus of the $CH_4$-$CO_2$ system

| **Model** | **AAD%** | **Experimental data compared** |
|---|---|---|
| Nikolaidis et al. [65] | 2.19% | Davis et al. [41], Donnelly and Katz [38] |
| Ababneh & Al-Muhtaseb [23] | 2.14% | Davis et al. [41] |
| Riva et al. [4] | 1.94% | Davis et al. [41] |
| Tang [83] | 1.98% | Davis et al. [41] |
| Yokozeki [85] | 2.05% | Davis et al. [41]* |
| Ali et al. [69] | 0.1447% | Davis et al. [41] |

* As reported in Riva et al. [4]

Table 4-6 clearly shows that the model developed in this study has results comparable to other models found in the literature. However, unlike most of the other models that only predicted SLV locus of this binary system, the model developed here was also used to predict the distribution of $CO_2$ in the different phases.

### 4.4 Comparison with other modeling approaches for binary system $CH_4$-$H_2S$

Only a limited number of studies attempted to model the SLVE of the $CH_4$-$H_2S$ binary System using the first two approaches. These studies are highlighted below according to the corresponding approach.

#### 4.4.1 Coupling EoS with specific models of solid phase fugacity approach

As discussed in the previous sections, This have used an empirical correlation model to represent the $CH_4$-$H_2S$ SLVE locus.

#### 4.4.2 Using EoS for vapor, liquid and solid phases approach

Langè et al. have studied the phase equilibrium behavior of the system $CH_4$-$H_2S$, at temperatures ranging from 70 Kelvin up to the critical temperature of $H_2S$ (373.1 Kelvin) and pressures up to 25 bar [45]. Phase diagrams for this binary system at the SLVE locus have been found using the solid-liquid-vapor equation of state proposed by Yokozeki [85].

Figure 4-14 shows the results of these two studies compared to the experimental data [47]. From Figure 4-14, it is clear that the correlations of Lange et al. are more accurate than those predicted in this study, which could be explained by the fact that Yokozeki's EoS does not consider the solid phase to be pure $H_2S$, which gives the equation more flexibility in predicting the locus curve, thus resulting in better representative correlations.

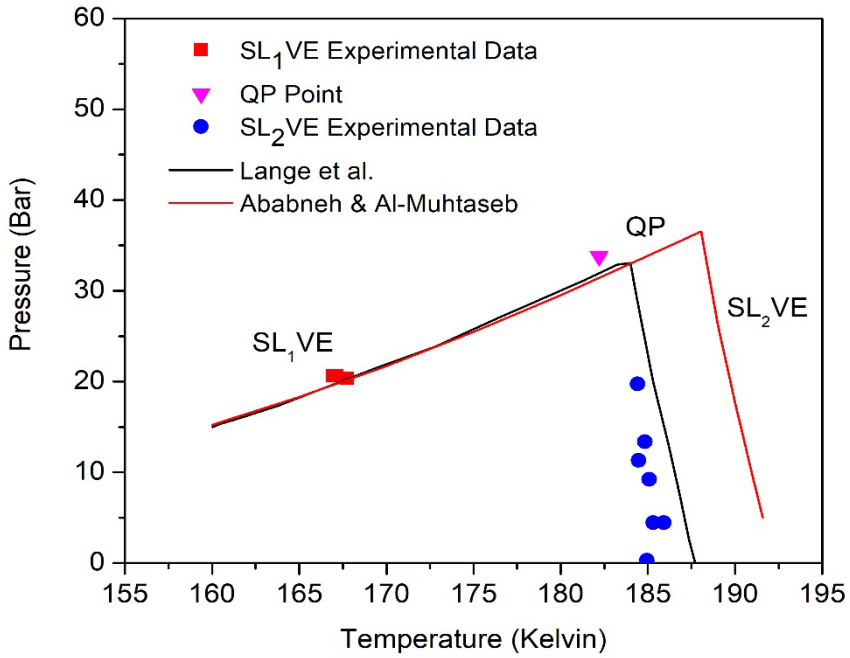


Figure 4-14: Comparison between model predictions (lines) [45] [23] and laboratory data (symbols) [47] for the SLVE locus of the methane-hydrogen sulfide system.

### 4.5 Comparison with other modeling approaches for binary system $CO_2$-$H_2S$

Little work has been done on modelling the SLVE locus of $CO_2$-$H_2S$ system. The main modelling efforts were focused on the VLE of this binary system [87]–[89]. The only study that addressed the SLVE of this system was by Ababneh and Al-Muhtaseb [23], where they successfully predicted the SLVE locus curve and the distrbution of $H_2S$ and $CO_2$ between the three phase. They utlized an empirical correlation model in their study , which covered the temperature range slightley above the solidfication point of $H_2S$ within the mixture (from 177.54 Kelvin up to 215.8 Kelvin). Thus, in the studied range of temperature, the solid phase was assumed to consist of pure $CO_2$, and Eq. 2 was used to find the fugacity of the solid $CO_2$ phase. Furthermore, the vapor and liquid phase fugacities were calculated using the PR EoS [71]. The interaction parameter between the two components was optimized to experimental data [51] to a value of 0.11, which resulted in total error of 14.1%. The

total error was calcuated based on the errors in pressure, liquid phase composition, and vapor phase composition comapred to the experimental data by Sobocinski and Kurata [51]. Their results agreed very well with the experimental data as shown in Figures 4-15a and 4-15b.

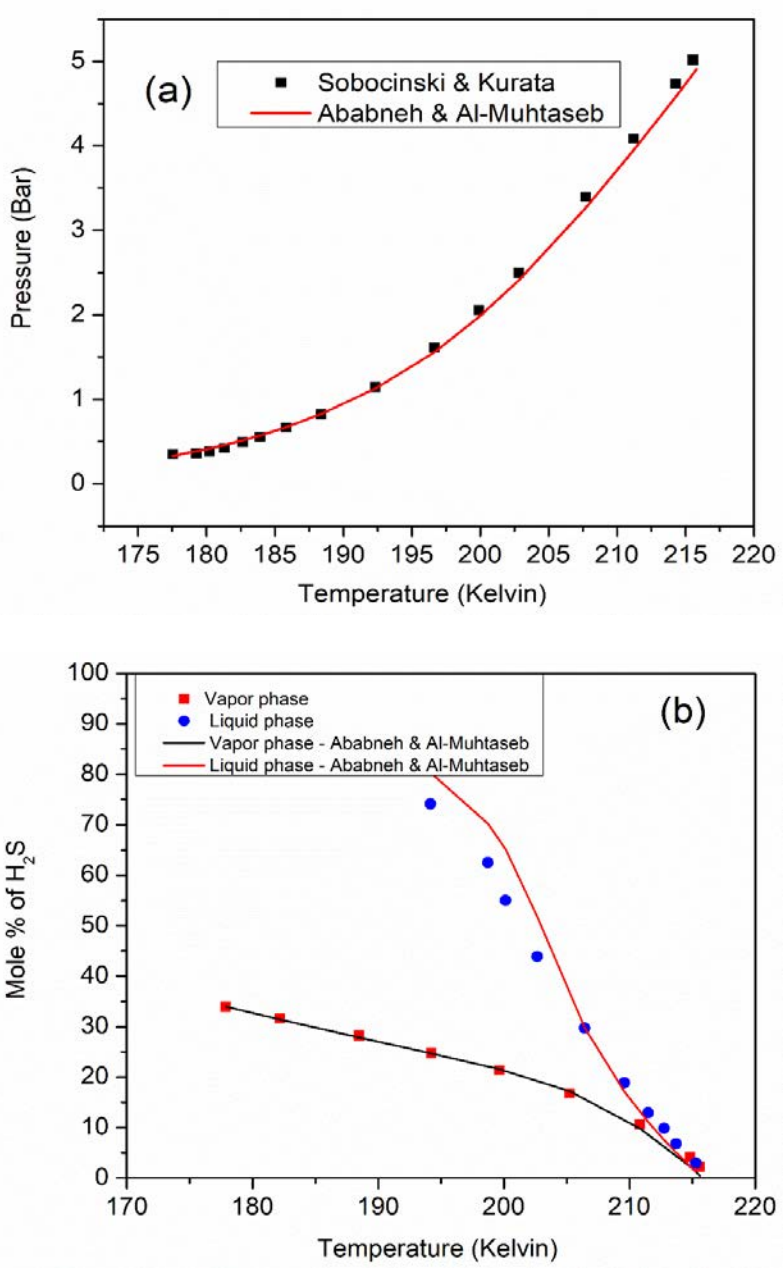


Figure 4-15:Model predictions (lines) compared to the experimental data (symbols) for the binary system $CO_2$-$H_2S$ in terms of (a) the SLVE locus [51][23] and (b) the composition of $H_2S$ in the liquid and vapor phases [51][23].

### 4.6 Comparison with other modeling approaches for ternary System of $CH_4$-$CO_2$-$H_2S$

Theveneau et al. [52] have utilized four equations of state, which are based on the group contribution method; the PPR78 (predictive, 1978 Peng Robinson) EoS [90], the PSRK (Soave–Redlich–Kwong) EoS [91], a semi-empirical EoS, and the PR-HV (Peng Robinson-Huron-Vidal mixing rule) EoS with the NRTL activity model [92]; to predict the $CO_2$ freezing temperatures [52]. Table 3-7 compares the results of this study with the above mentioned studies [52] [23], to the experimental data obtained by Theveneau et al. [52]; where MAD and MRD are defined in Eq. 4-28 and 4-29, respectively. It could be noticed from Table 3-7 that PR-HV/NRTL and this study models have the best predictions of the experimental data.

Table 4-7: Comparison between the different studies for the ternary system of $CH_4$-$CO_2$-$H_2S$

| | | | | | Theveneau et al. [52] | | | |
|---|---|---|---|---|---|---|---|---|
| | Experimental data [52] | | This study | PPR78 [90] | PSRK UNIFAC [91] | PR-HV /NRTL-V [92] | GERG 2008 (REFPROP) [93] | GERG 2008 (REFPROP) with Jager and Span model [67] |
| Mixture | P (MPa) | $T_{exp}$ (Kelvin) | $T_{pred}$ (Kelvin) | $T_{pred}$ (Kelvin) | $T_{pred}$ (Kelvin) | $T_{pred}$ (Kelvin) | $T_{pred}$ (Kelvin) | $T_{pred}$ (Kelvin) |
| 1 | 2.224 | 209.80 | 213.03 | 209.67 | 210.31 | 210.45 | 210.54 | 210.26 |
| 2 | 2.186 | 202.33 | 203.74 | 208.5 | 209.18 | 203.15 | 209.28 | 209.03 |
| 3 | 1.848 | 196.85 | 200.05 | 173.06 | 185.91 | 198.85 | 193.25 | 192.75 |
| 4 | 1.974 | 194.32 | 197.62 | 167.93 | 181.54 | 195.15 | 189.91 | 189.26 |
| 5 | 2.123 | 192.26 | 195.43 | 163.18 | 177.99 | 191.45 | 186.98 | 186.27 |
| MAD (K) | | | 2.86 | 17.11 | 9.07 | 1.02 | 4.2 | 4.46 |
| MRD (%) | | | 1.44% | 8.78% | 4.63% | 0.52% | 2.12% | 2.27% |

# CHAPTER 5: NOBLE GASES-NITROGEN SYSTEM ($N_2$-Kr-Xe)[6]

This chapter is an attempt to utilize a model suggested in chapter 3 to model the SLVE of the ternary system Kr-Xe-$N_2$. The main aim of this chapter is to develop a thermodynamic model that can describe the solid-liquid-vapor (SLV) phase equilibria for the ternary system of Kr-Xe-$N_2$ over specific ranges of pressures and temperatures (1-45 bar and 80-180 K, respectively). The results of the thermodynamic mathematical model developed in this work will be used to determine the phase envelope of the ternary system (Kr-Xe-$N_2$) at a sample overall composition.

## 5.1 Modeling of the binary and ternary systems consisting the noble gases in nitrogen

### 5.1.1 Modelling the Binary System of Krypton-Nitrogen (Kr-$N_2$)

Correlating the SLVE phase equilibrium of the Kr-$N_2$ system depends on estimating the fugacities of these two components in each phase. To do so, we employ the PR EoS along with the following fugacity equations.

$$\hat{f}_{Kr}^{V} = y_{Kr}\hat{\varphi}_{Kr}^{V}P \qquad (5\text{-}1)$$

$$\hat{f}_{Kr}^{L} = x_{Kr}\hat{\varphi}_{Kr}^{L}P \qquad (5\text{-}2)$$

$$\hat{f}_{Kr}^{S} = x_{Kr}\,\hat{\varphi}_{Kr}^{Sub}\left(T, P_{Kr}^{Sub}\right)\; P_{Kr}^{Sub}\; exp\left[\frac{v_o^s}{RT}(P - P_{Kr}^{Sub})\right] \qquad (5\text{-}3)$$

where the solid phase is assumed to consist of pure Kr since the tested temperatures are well above the triple point of nitrogen. The sublimation pressure for Kr is estimated from Eq. 5-4 [94], where *a* and *b* are constants that are listed in Table 5-1.

[6] This chapter was taken from the published article: H. Ababneh and S. A. Al-Muhtaseb, "Prediction of solid-liquid-vapor phase equilibria of noble gases in nitrogen," Arab. J. Chem., vol. 15, no. 6, p. 103866, 2022, doi: 10.1016/j.arabjc.2022.103866

$$\ln P_{Kr}^{Sub}\,(Torr) = \frac{a}{T(K)} + b \qquad (5\text{-}4)$$

The fugacities of $N_2$ can be obtained from:

$$\hat{f}_{N_2}^{V} = y_{N_2}\hat{\varphi}_{N_2}^{V}P \qquad (5\text{-}5)$$

$$\hat{f}_{N_2}^{L} = x_{N_2}\hat{\varphi}_{N_2}^{L}P \qquad (5\text{-}6)$$

At the SLVE pressure-temperature (PT) locus, where the solid phase is assumed to consist of pure Kr, the phase equilibrium equations for Kr are given by Equations 5-7 and 5-8.

$$\hat{f}_{Kr}^{V} = \hat{f}_{Kr}^{L} \qquad (5\text{-}7)$$

$$\hat{f}_{Kr}^{V} = \hat{f}_{Kr}^{S} \qquad (5\text{-}8)$$

Whereas the phase equilibrium equation for $N_2$ is given by Eq. 5-9

$$\hat{f}_{N_2}^{V} = \hat{f}_{N_2}^{L} \qquad (5\text{-}9)$$

Table 5-1: Sublimation pressure equation parameters for Krypton [94].

| Temperature range (K) | *-a* (K) | *b* |
|---|---|---|
| 115.0-107.0 | 1332.30 | 17.8184 |
| 107.0-98.4 | 1334.63 | 17.8413 |
| 98.4-90.2 | 1346.76 | 17.9656 |
| 90.2-73.8 | 1330.73 | 17.7765 |
| 73.8-54.7 | 1399.08 | 18.5731 |

### 5.1.2 Modelling the Binary System of Xenon-Nitrogen (Xe-$N_2$)

The triple point temperatures of xenon (161.1 K) is higher than the critical temperature of nitrogen (126.1 K). Thus, unlike the Kr-$N_2$ system, the SLVE locus line of the Xe-$N_2$ system is discontinued when it reaches near the critical point of nitrogen.

Teller and Knapp [36] studied the composition of the liquid phase in equilibrium with the solid and the vapor phases as a function of temperature for two temperature ranges (namely, from 91.04 to 127.29 K and from 153.6 to 161.4 K). However, although they did not study the composition of the solid phase, it could be expected that nitrogen does not dissolve much, if any, in solid xenon; and that a eutectic point exists close to the triple point of nitrogen. As a result, the solid phase can be assumed to consist of pure Xe. In the modeling of this system, the overall temperature range will be divided into two sub-ranges in accordance to the available experimental data [36] to be used for optimizing the corresponding interaction parameter.

The SLVE pressure-temperature (*PT*) locus curve of the Xe-$N_2$ system depends on estimating the fugacities of these two components in each phase. To do so, we employ the PR EoS to estimate their fugacity coefficients in the vapour and liquid phases, along with the fugacity equations (Equations 5-10 to 5-12) as shown below.

$$\hat{f}_{Xe}^{V} = y_{Xe}\hat{\varphi}_{Xe}^{V}P \qquad (5\text{-}10)$$

$$\hat{f}_{Xe}^{L} = x_{Xe}\hat{\varphi}_{Xe}^{L}P \qquad (5\text{-}11)$$

$$\hat{f}_{Xe}^{S} = x_{Xe}\,\hat{\varphi}_{Xe}^{Sub}\left(T, P_{Xe}^{Sub}\right)\; P_{Xe}^{Sub}\;\; exp\left[\frac{v_o^S}{RT}(P - P_{Xe}^{Sub}\right] \qquad (5\text{-}12)$$

where $P_{Xe}^{Sub}$ is the sublimation/saturation pressure for Xe, which is estimated from Eq. 5-13 [94], where *c* and *d* are constants that are listed in Table 5-2.

$$\ln P_{Xe}^{Sub}\,(Torr) = \frac{c}{T(K)} + d \qquad (5\text{-}13)$$

the fugacities of $N_2$ can be obtained from Equations 5-5 and 5-6.

At the SLVE locus, where the solid phase is assumed to consist of pure Xe. Hence, the phase equilibrium equations for Xe are given by Equations 5-14 and 5-15.

$$\hat{f}_{Xe}^{V} = \hat{f}_{Xe}^{L} \quad (5\text{-}14)$$

$$\hat{f}_{Xe}^{V} = \hat{f}_{Xe}^{S} \quad (5\text{-}15)$$

whereas the phase equilibrium equation for $N_2$ is given by Eq. 5-9.

Table 5-2: Sublimation pressure equation parameter for Xenon [94].

| Temperature range (K) | -*c* (K) | *d* |
|---|---|---|
| 162.0-150.2 | 1856.41 | 17.9236 |
| 150.2-139.0 | 1857.02 | 17.9276 |
| 139.0-127.0 | 1860.70 | 17.9513 |
| 127.0-104.0 | 1836.37 | 17.7526 |
| 104.0-76.2 | 1960.37 | 18.9607 |

### 5.1.3 Modelling the Binary System of Krypton-Xenon (Kr-Xe)

In the modelling of the binary system of Kr-Xe, the SLVE temperature range would start from a point slightly beyond the triple point of Kr. In the specified temperature range, only Xe will solidify. Therefore, the solid phase will consist of only Xe. Mastera [63] has measured the SLVE locus for the Kr-Xe binary system accordingly.

The empirical model developed in this work can be used to predict the SLVE behaviour of this system. The fugacities of Kr in different phases can be calculated via Equations 5-6, whereas those of Xe can be calculated by Equations 14-16. Furthermore, at the SLVE locus for this binary system, the phase equilibrium conditions for Kr and Xe can be described by Equation 11and Equations 18-19, respectively. As explained previously, it is assumed that the solid phase consists of pure Xe within the specified range of temperature.

### 5.3.4 Modelling the Ternary System (Kr-Xe-$N_2$)

In the modelling of this ternary system, it was assumed that only Kr and Xe can solidify since the tested temperature is well above the triple point of $N_2$. However, it was assumed that the solid phase for each component is pure consisting only of this component. Therefore, when both Kr and Xe solidify, they are assumed to form two distinct solid phases. The solid Kr phase will be denoted as $S_2$ while the solid Xe phase will be denoted as $S_3$. Therefore, the fugacities of Kr can be obtained from Equations 5-1 through 5-3, those of Xe can be obtained from Equations 5-10 through 5-12, and those of $N_2$ can be obtained from Equations 5-5 and 5-6. At the SLVE locus for this ternary system, Equations 5-7 and 5-8 describe the phase equilibrium conditions for Kr, Equations 5-14 and 5-15 describe the phase equilibrium conditions for Xe, and Equation 5-9 describes the phase equilibrium condition for $N_2$.

## 5.2 Results and Discussion

### 5.2.1 Correlating the Binary System of Krypton-Nitrogen (Kr-$N_2$)

The interaction parameter ($k_{ij}$) for the binary system Kr-$N_2$ was optimized to the equilibrium equations described in the previous section. Figure 5-1 shows a comparison between the model estimations and experimental data available in the literature [36] at different $k_{ij}$ values in terms of the SLVE PT locus (Figure 5-1a) and the mole fraction of Kr in the liquid phase (Figure 5-1b) as a function of temperature. Table 5-3 shows the effect of tested $k_{ij}$ values on the deviations between the model predictions and the experimental data in terms of pressure and Kr composition.The optimization of the interaction parameter was based on minimizing error as defined in Equation 5-16; and the deviations between model predictions and experimental data were indicated through the mean average deviation (MAD) and mean relative deviation (MRD) as defined by

Equations 4-28 and 4-29, respectively.

$$Error = \left(\frac{U_{exp} - U_{Cal}}{U_{exp}}\right)^2 \quad (5\text{-}16)$$

Overall, it could be concluded that the PR EoS produces best results (with minimum $\sum SSE$) when $k_{ij}$ = 0.03000. Therefore, this value is considered as the optimum interaction parameter for this binary system.

Table 5-3: Effect of tested interaction parameters on the errors in predicting SLVE pressures and Kr composition in the liquid phase for Kr-$N_2$ system when compared to the experimental data [36]. The line with a bold font indicates the optimum interaction parameter (with minimum Σ Error).

| $k_{ij}$ | Error in Pressure | MAD in Pressure (Bar) | MRD in Pressure % | Error in $x_{Kr}$ | MAD in $x_{Kr}$ | MRD in $x_{Kr}$ % | $\sum$ Error |
|---|---|---|---|---|---|---|---|
| **0.05000** | 1.767 | 0.339 | 16.73 | 0.587 | 0.037 | 14.662 | 2.354 |
| **0.03250** | 1.190 | 0.153 | 11.454 | 0.140 | 0.031 | 7.705 | 1.330 |
| **0.03125** | 1.167 | 0.172 | 11.879 | 0.148 | 0.033 | 7.941 | 1.315 |
| **0.03000** | 1.147 | 0.191 | 12.306 | 0.162 | 0.036 | 8.695 | 1.309 (min) |
| **0.02500** | 1.089 | 0.277 | 14.454 | 0.281 | 0.047 | 12.257 | 1.370 |
| **0.01000** | 1.107 | 0.539 | 21.323 | 1.290 | 0.081 | 25.070 | 2.396 |
| **0.00000** | 1.256 | 0.704 | 25.837 | 2.517 | 0.103 | 34.344 | 3.773 |

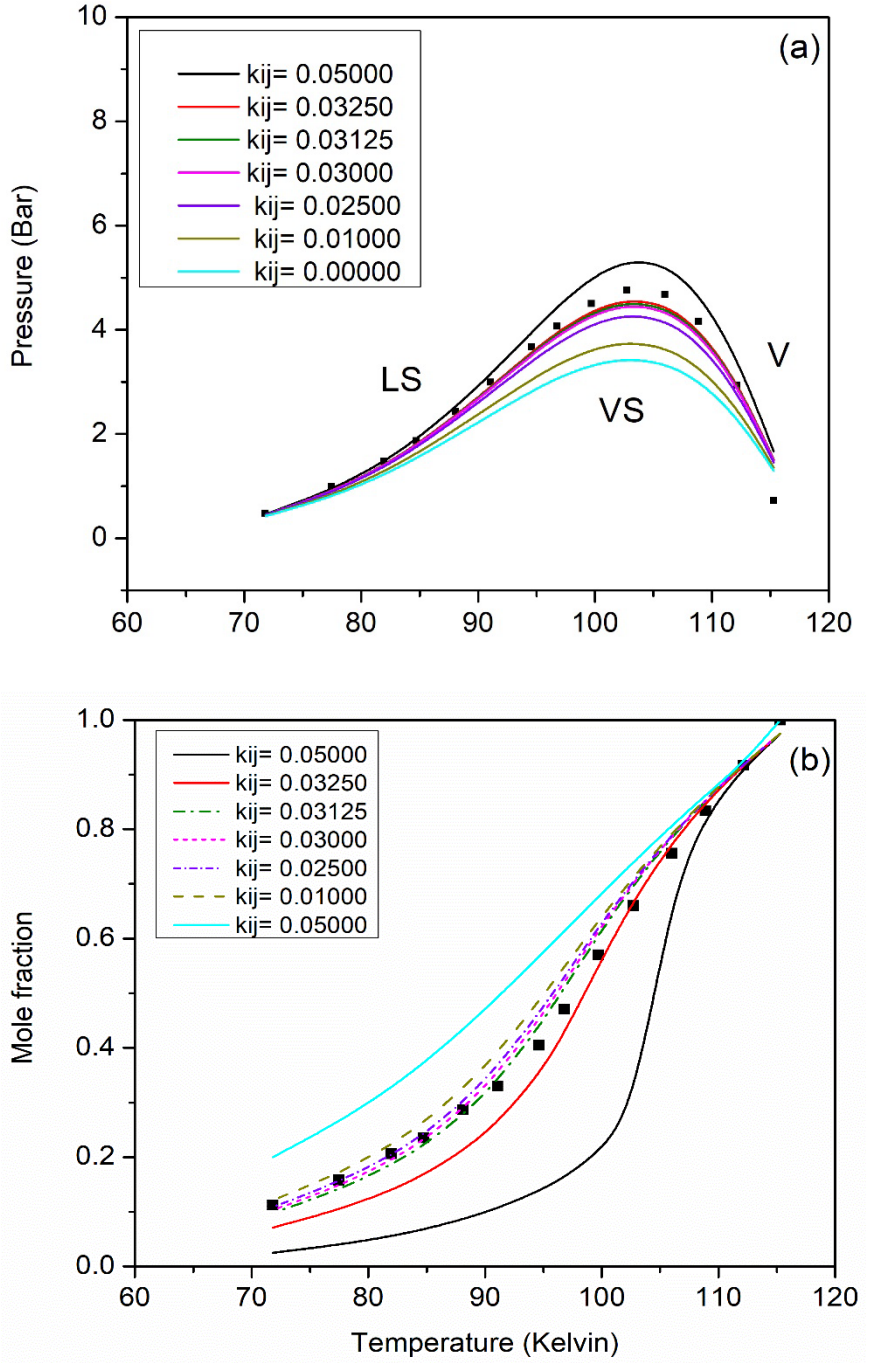


Figure 5-1: Comparison of model predictions (lines) with different kij values to experimental data (symbols) for the binary system Kr-$N_2$ [36]. Subfigures show the effect of temperature on SLVE (a) pressure and (b) composition of Kr in liquid phase

### 5.2.2 Correlating the Binary System of Xenon-Nitrogen (Xe-$N_2$)

The interaction parameter ($k_{ij}$) for the binary system Xe-$N_2$ was optimized as described in Section 5.1.2. Figure 5-2 shows a comparison between the model predictions and the experimental SLVE PT locus data (Figures 5-2a and 5-2b) and mole fraction of Xe in the liquid phase (Figures 5-2c and 5-2d) available in the literature as a function of temperature for both temperature sub-ranges of the available experimental data [36]. Table 5-4 shows the error, MAD and MRD values between model predictions and the experimental data in terms of pressure and Xe composition at the tested $k_{ij}$ values. From Table 5-4 and Figure 5-2, and based on the least sum of error values (minimum $\sum Error$), it could be noticed that optimum interaction parameter for the first temperature range (91.04-127.29 K) is 0.100, while that for the second temperature range (153.6 - 161.36 K) was 0.000.

Table 5-4: Effect of tested interaction parameters on the errors in predicting SLVE pressures and Kr composition in the liquid phase for the binary system Xe-$N_2$ when compared to the experimental data reported by Teller and Knapp [36] . The lines with a bold font indicate the optimum interaction parameter (with minimum $\Sigma$ error).

| $k_{ij}$ | Error in Pressure | MAD in Pressure (Bar) | MRD in Pressure % | Error in $x_{Kr}$ | MAD in $x_{Kr}$ | MRD in $x_{Kr}$ % | $\sum$ **Error** |
|---|---|---|---|---|---|---|---|
| Temperature range 1 (91.04-127.29 K) | | | | | | | |
| 0.000 | 0.080 | 1.705 | 9.412 | 58.668 | 0.046 | 232.431 | 58.748 |
| 0.005 | 0.071 | 1.569 | 8.775 | 44.018 | 0.036 | 195.363 | 44.088 |
| 0.010 | 0.063 | 1.450 | 8.214 | 33.152 | 0.028 | 164.453 | 33.215 |
| 0.020 | 0.052 | 1.252 | 7.264 | 18.782 | 0.018 | 117.842 | 18.834 |
| 0.030 | 0.043 | 1.090 | 6.485 | 10.502 | 0.012 | 85.310 | 10.545 |
| 0.050 | 0.032 | 0.893 | 5.439 | 3.149 | 0.0126 | 54.563 | 3.181 |
| 0.100 | 0.021 | 0.746 | 4.337 | 1.789 | 0.0183 | 42.093 | 1.809 (min) |
| 0.200 | 0.089 | 1.490 | 6.113 | 5.615 | 0.027 | 83.770 | 5.705 |

| $k_{ij}$ | Error in Pressure | MAD in Pressure (Bar) | MRD in Pressure % | Error in $x_{Kr}$ | MAD in $x_{Kr}$ | MRD in $x_{Kr}$ % | $\sum$ **Error** |
|---|---|---|---|---|---|---|---|
| Temperature range 2 (153.6 - 161.36K) | | | | | | | |
| 0.000 | 68.074 | 11.121 | 140.827 | 0.003 | 0.023 | 2.547 | 68.077(min) |
| 0.005 | 72.913 | 8.916 | 144.313 | 0.003 | 0.021 | 2.545 | 72.916 |
| 0.010 | 78.133 | 8.615 | 147.924 | 0.003 | 0.023 | 2.544 | 78.136 |
| 0.020 | 89.843 | 8.078 | 156.275 | 0.003 | 0.023 | 2.540 | 89.846 |
| 0.030 | 103.495 | 7.659 | 166.400 | 0.0029 | 0.0234 | 2.5358 | 103.498 |
| 0.050 | 138.080 | 7.114 | 191.459 | 0.006 | 0.031 | 3.253 | 138.085 |
| 0.100 | 294.079 | 12.975 | 302.090 | 0.003 | 0.023 | 2.431 | 294.082 |
| 0.200 | 5172.607 | 489.364 | 2363.424 | 0.014 | 0.051 | 5.482 | 5172.621 |

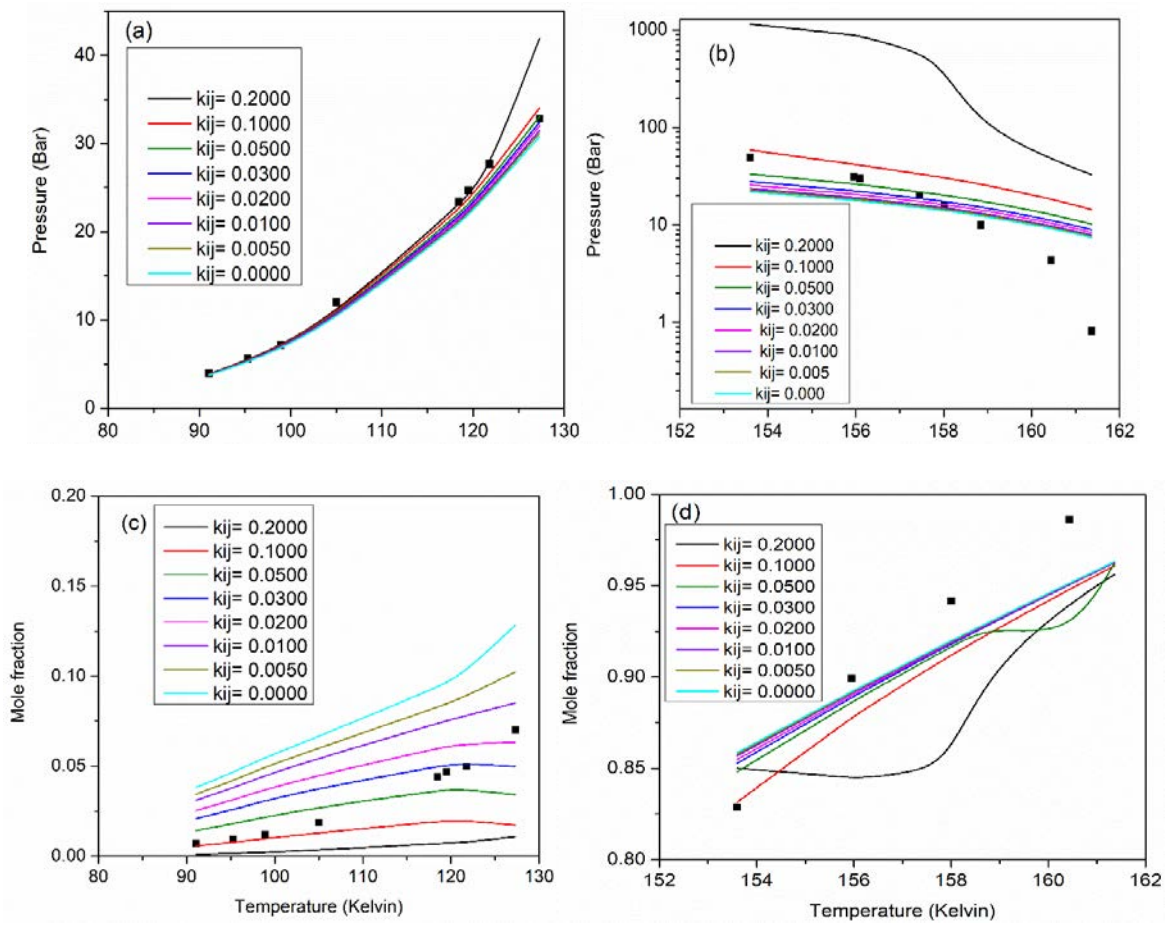


Figure 5-2: Comparison of model predictions (lines) and experimental data (symbols) of the binary system Xe-$N_2$ [36] for the effect of temperature on SLVE (a,b) pressure and (c,d) composition of Xe in liquid phase. The effect of temperature is considered in the ranges of 91.04-127.29 K (a and c) and 153.6 - 161.36K (b and d)

### 5.2.3 Correlating the Binary System of Krypton-Xenon (Kr-Xe)

As described in section 5.1.3, the SLV locus for this binary system was estimated, and the model predictions were compared to the experimental data reported by Mastera [63]. The results are show in Table 5-5. By manipulating the interaction parameter in the PR EoS, it was found that the optimum $k_{ij}$ value for this system is 0.0400 as noted in Table 5-5. Figure 5-3a shows a comparison between the model estimations and experimental data available in the literature [63] for the SLVE pressure-temperature locus, while Figure 3b illustrates the mole fraction of Kr in the liquid phase as a function of temperature. It can be noted from Figure 5-3a that the experimental SLVE locus of this binary system reaches a maximum value at pressure of 1.6 bar. The model predictions were compared to the experimental data as seen from Figure 5-3a, where the model calculations provided a good description of the laboratory data when the interaction parameter value in the EoS was 0.0400, confirming the suitability of our model for representing such systems. Figure 5-3b shows that increasing the temperature would decrease the mole fraction of Kr (i.e., increase the mole fraction of Xe) in the liquid phase. This could be attributed to the fact that raising the temperature would decrease the amount of the solid phase that is formed; and since the solid phase consists of pure Xe; larger amounts of Xe will be present in the liquid phase at higher temperatures. Similar to the PT diagram, the model predictions at $k_{ij}$=0.0400 described well the composition of the liquid phase as seen in Figure 5-3b, however, increasing $k_{ij}$ would cause the results to deviate significantly (such as in the case of $k_{ij}$=0.1000).

Table 5-5: Effect of tested interaction parameters on the errors in predicting SLVE pressures and Kr composition in the liquid phase for Kr + Xe system compared to the experimental data [63] . The line with a bold font indicates the optimum interaction parameter (with minimum ∑Error).

| $k_{ij}$ | Error in Pressure | MAD in Pressure (Bar) | MRD in Pressure % | Error in $x_{Kr}$ | MAD in $x_{Kr}$ | MRD in $x_{Kr}$ % | $\sum$ Error |
|---|---|---|---|---|---|---|---|
| **0.0000** | 0.275 | 0.282 | 19.530 | 0.216 | 0.059 | 20.557 | 0.492 |
| **0.0200** | 0.110 | 0.183 | 13.125 | 0.159 | 0.047 | 17.522 | 0.268 |
| **0.0250** | 0.088 | 0.169 | 12.329 | 0.145 | 0.043 | 16.654 | 0.232 |
| **0.0300** | 0.076 | 0.155 | 11.518 | 0.131 | 0.039 | 15.733 | 0.207 |
| **0.0400** | 0.087 | 0.140 | 10.712 | 0.107 | 0.031 | 13.702 | 0.194 (min) |
| **0.0425** | 0.099 | 0.151 | 11.353 | 0.101 | 0.028 | 13.150 | 0.200 |
| **0.0450** | 0.114 | 0.173 | 12.585 | 0.096 | 0.026 | 12.577 | 0.210 |
| **0.0500** | 0.156 | 0.219 | 15.155 | 0.088 | 0.021 | 11.366 | 0.244 |
| **0.1000** | 1.921 | 0.897 | 58.397 | 0.250 | 0.072 | 18.776 | 2.171 |

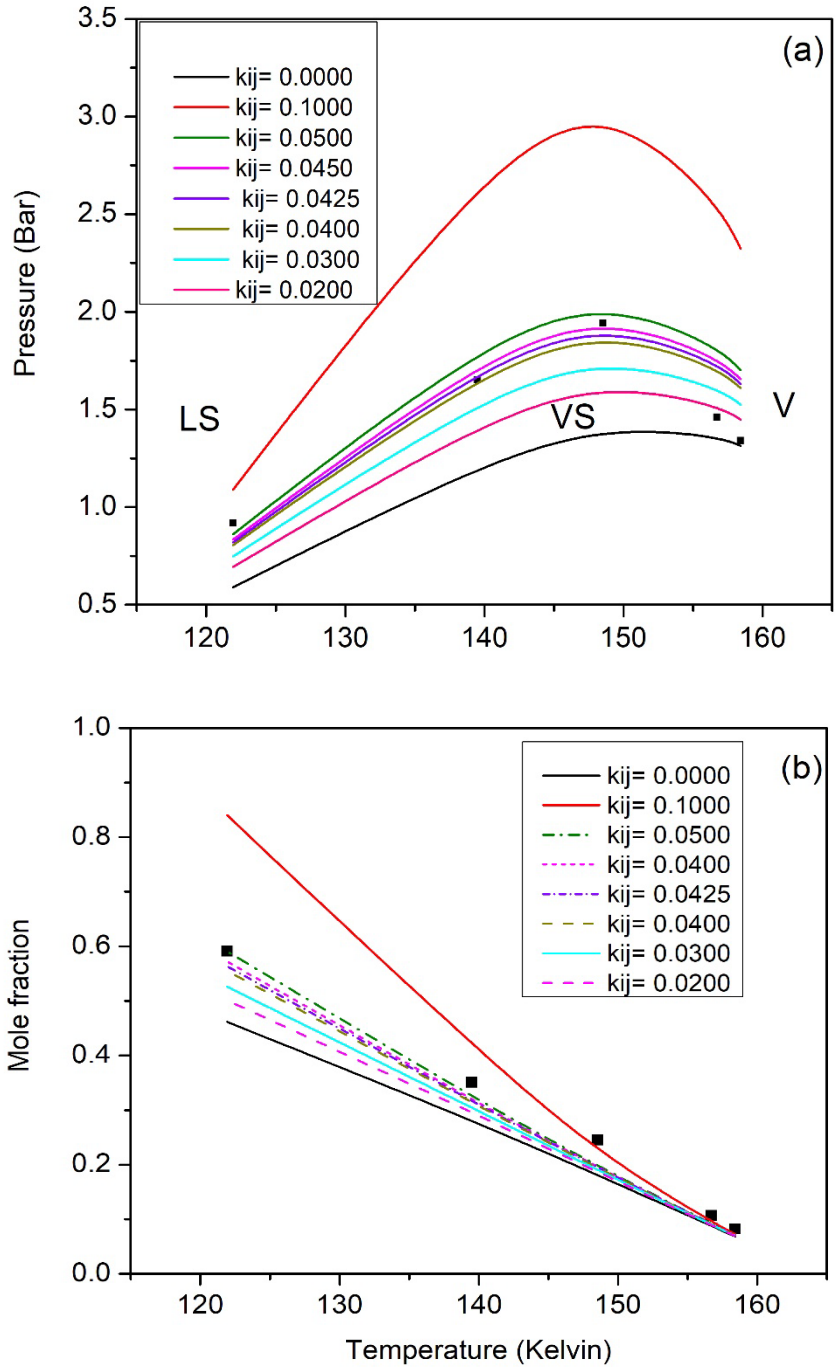


Figure 5-3: Comparison of model predictions with different $k_{ij}$ values (lines) to experimental data (symbols) for the binary system Kr-Xe [63]. Subfigures show the effect of temperature on the SLVE (a) pressure and (b) composition of Kr in liquid phase.

### 5.2.4 Correlating the Ternary System Krypton-Xenon-Nitrogen (Kr-Xe-$N_2$)

Table 5-6 shows the experimental SLVE data obtained by Teller and Knapp [36] for the Ternary system Kr-Xe-$N_2$. These data indicate the composition of the liquid phase in equilibrium with the solid and vapor phases in a Xe-Kr-$N_2$ mixture as a function of temperature for the temperature range of 98.48-105.05 K [36]. It was noticed that there are apparent errors in these published data, where in several rows, the summations of mole fractions do not add up to unity! In some rows, it seems that the decimal point for $x_{Xe}$ may not have been placed correctly. The last column in Table 6 shows an attempt for correcting such errors.

To correlate this ternary system as described in Section 5.1.4, interaction parameters for the constituting binary systems (Kr-$N_2$, Xe- $N_2$ and Kr-Xe) are needed. The interaction parameter chosen for the Kr-$N_2$ binary system is 0.0300, which is the optimum value found in section 5.2.1. Furthermore, since the range of the tested temperature is within the first temperature range for the Xe-$N_2$ binary system described in section 5.2.2, the optimum interaction parameter was set to the value of 0.100. Also, the optimum interaction parameter for the Kr-Xe binary system chosen to be 0.040 as found in section 5.3.3.

As seen in Table 5-6, few experimental points for the ternary system were collected at the same temperature and pressure, with almost equal values of the corresponding compositions. For these points, the average value of the composition was to be compared with the model predictions. Figure 5-4 compares the results of the model predictions of liquid phase compositions to the experimental data presented in Table 5-6 at the optimum values of the interaction parameters

Table 5-6: Experimental liquid phase composition data of the ternary system Kr-Xe-$N_2$ SLVE as reported by Teller and Knapp [36].

| Pressure (Bar) | Temperature (K) | $x_{N_2}$ | $x_{Kr}$ | $x_{Xe}$ | Corrected $x_{Xe}$ |
|---|---|---|---|---|---|
| 6 | 104.9 | 0.4519 | 0.4284 | 0.1192 | 0.1197 |
| 5.99 | 104.61 | 0.4743 | 0.414 | 0.1117 | 0.1117 |
| 5.97 | 104.58 | 0.4731 | 0.4132 | 0.1137 | 0.1137 |
| 6.02 | 105.05 | 0.4438 | 0.4334 | 0.1128 | 0.1228 |
| 6.02 | 105.05 | 0.4592 | 0.4216 | 0.1192 | 0.1192 |
| 6.01 | 102.96 | 0.6446 | 0.2944 | 0.61 | 0.0610 |
| 6.01 | 102.96 | 0.6479 | 0.2922 | 0.599 | 0.0599 |
| 6 | 102.7 | 0.645 | 0.2945 | 0.605 | 0.0605 |
| 6.01 | 100.6 | 0.6619 | 0.2854 | 0.527 | 0.0527 |
| 6.01 | 100.6 | 0.6651 | 0.2828 | 0.52 | 0.0521 |
| 6 | 100.13 | 0.7186 | 0.2385 | 0.429 | 0.0429 |
| 5.99 | 98.55 | 0.8735 | 0.1033 | 0.0232 | 0.0232 |
| 5.99 | 98.6 | 0.8682 | 0.1071 | 0.0247 | 0.0247 |
| 5.99 | 98.6 | 0.8742 | 0.1027 | 0.0231 | 0.0231 |
| 6 | 98.48 | 0.8772 | 0.0994 | 0.0234 | 0.0234 |

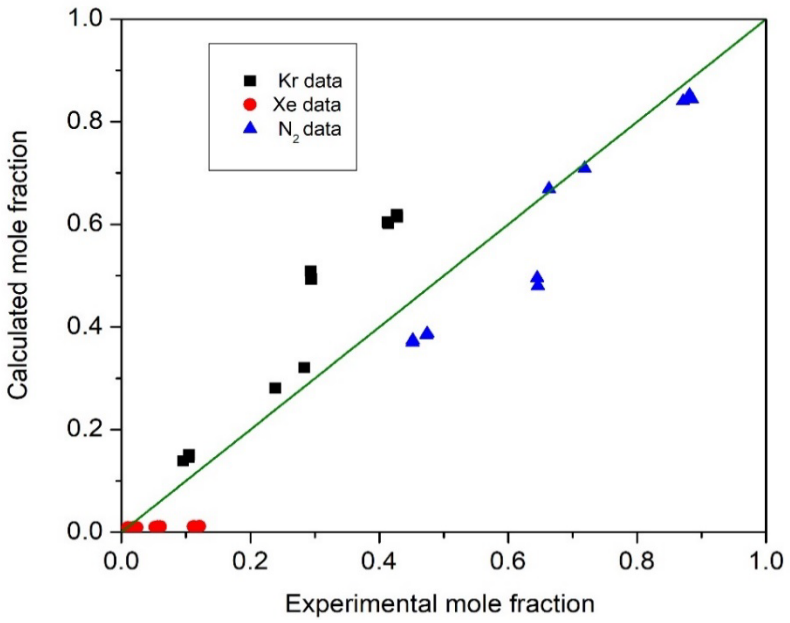


Figure 5-4: Comparing predicted liquid phase compositions to experimental data for the ternary system Kr-Xe-$N_2$ at the optimum interaction parameters [36]

In the absence of extensive and reliable experimental SLVE data for the ternary system Kr-Xe-$N_2$, its phase envelopes are not clear. So, in this section, we attempt to determine the phase envelope for this system on the basis of a single equilibrium separation stage unit similar to the one used in Chapter 4**.** A feed mixture (consisting of 50 mole% $N_2$, 30 mole% Kr and 20 mole% Xe) was tested as an example. Figure 5-5 shows the pressure-temperature SLVE phase envelopes for tested feed mixture, where the solid phases are assumed to consist of either pure Kr (denoted as $S_2$), pure Xe (denoted as $S_3$) or a mixture of Kr and Xe (denoted as $S_2S_3$). It could be noticed that there is a gap in the ternary system SLVE phase envelope. This gap extends from the point (T= 119.96 K, P=19.12 Bar) to the point (T= 177.5 K, P=45 Bar), where these points are close to the critical points of $N_2$ and Xe, respectively; which is similar to the case seen previously in the Xe-$N_2$ binary system. Moreover, it is clear from Figure 5-5 that the envelope of $VS_2S_3$ phases is relatively small, with a maximum point standing at about 2 bar. Therefore, it

seems that the presence of Xe in the system has a significant impact on the solidification behavior of Kr. Although the model has proved to be able to predict the phase envelopes, there is no possible way to confirm its results due to the lack of literature data. Thus, it is recommend that more experimental data or model predictions should be conducted for this system to be compared to the results of this model.

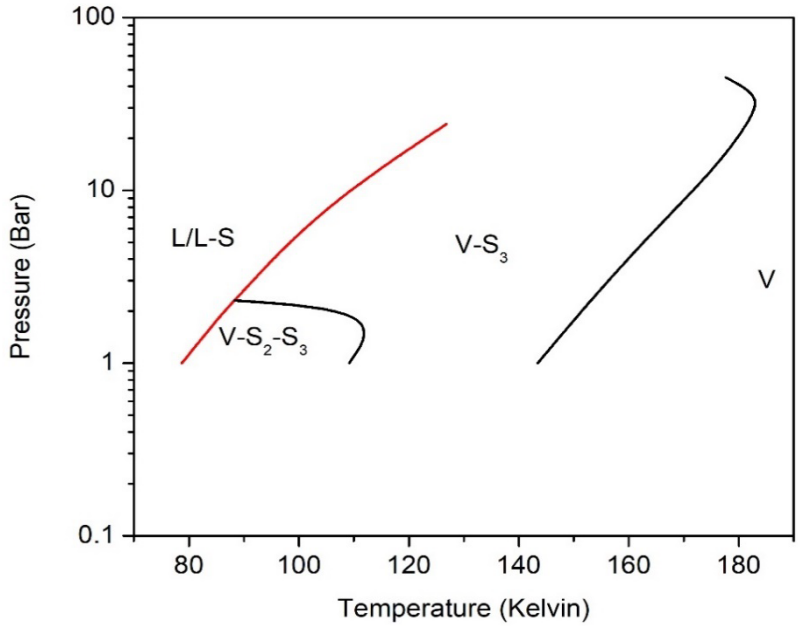


Figure 5-5: SLVE phase envelopes of the ternary system Kr-Xe-$N_2$ for the tested feed mixture.

### 5.3 Comparison with other models for noble gases in nitrogen system

Modeling efforts were done to compensate for the shortage of experimental SLVE data of systems involving such noble gases. Campestrini et al. [95] predicted the SLVE data of the mixtures Ar–Kr, Ar–$CH_4$, $CH_4$–Kr, $N_2$–$O_2$, $N_2$–Ar, and Ar–Xe using the Lennard-Jones solid-liquid-vapor equation of state (LJ-SLV-EoS). However, Campestrini et al. study has not covered the binary system combinations of interest in this work (i.e., the binary systems of Kr-$N_2$, Xe-$N_2$ and Kr-Xe), nor the ternary system of Kr-Xe-$N_2$.

# CHAPTER 6: FLUE GAS SYSTEM ($N_2$-$O_2$-$CO_2$)[7]

The first objective of this chapter is to develop an empirical correlation model based on the Peng-Robinson equation of state (PR EoS), with fugacity expressions, that is able to describe the SLVE and SVE behaviors for the ternary system of $N_2$-$O_2$-$CO_2$ at wide ranges of pressures and temperatures. The model predictions will be compared to the experimental data available in the literature to confirm its accuracy and reliability. The second objective of this chapter is construct a phase envelope for this ternary system, the phase envelope will be in solid-fluid equilibrium regions, in which only $CO_2$ is in the solid phase.

## 6.1 Modeling of the binary and ternary systems consisting the flue gas system

The first stage of this study was to develop a suitable mathematical model to predict and describe the SVE, SLE and SLVE behaviors for binary and ternary system of $N_2$, $O_2$ and $CO_2$. Following that, the model was optimized by fitting its interaction parameter to provide the best match of the experimental data of the corresponding binary systems available in the literature. Then, the model was used with the optimized interaction parameters to predict the corresponding equilibrium data and simulate an SV separation unit that is able to capture $CO_2$ from flue gas stream and collect it in liquid phase. The modelling work was completed using the Aspen Custom Modeler® (ACM) software, which is a process and equipment model development and simulation tool that is compatible with the simulation software packages of Aspen Plus and Aspen Hysys. The ACM has built-in codes, which are specific to chemical engineering applications involving thermodynamic properties such as fugacity and activity coefficients. The ACM has access

[7] This chapter was taken from the article currently under review: H. Ababneh, A. AlNouss, and S. A. Al-Muhtaseb, "Carbon Capture from Post Combustion Flue Gas Using a State-of-the-Art, Anti-Sublimation, Solid-Vapor Separation Unit"

to Aspen components and properties databases, which makes the software suitable for various chemical engineering applications.

In this study. The model descried in Chapter 3 to provide a good description of the SVE and SLVE region of systems involving binary and ternary mixtures involving $CO_2$, $N_2$ and $O_2$. The details of the model are described in the following sections.

### 6.1.1 SLVE modelling of the binary system $O_2$-$CO_2$

At the SLVE for the binary system $N_2$-$CO_2$, the solid phase will consist of pure $CO_2$. Therefore, the equilibrium equations for $CO_2$ are represented in Eqs 4-7 and 4-8, and that for $N_2$ is found in Eq. 6-1.

$$\hat{f}_{N_2}^{V} = \hat{f}_{N_2}^{L} \qquad (6\text{-}1)$$

The fugacity terms for $CO_2$ could be found using Equations 4-1 through 4-4. While nitrogen fugacity terms $\hat{f}_{N_2}^{V}$ and $\hat{f}_{N_2}^{L}$ could be found using Eqs. 6-2 and 6-3.

$$\hat{f}_{N_2}^{V} = y_{N_2}\hat{\varphi}_{N_2}^{V}P \qquad (6\text{-}2)$$

$$\hat{f}_{N_2}^{L} = x_{N_2}\hat{\varphi}_{N_2}^{L}P \qquad (6\text{-}3)$$

### 6.1.2 SLVE modelling of the binary system $O_2$-$CO_2$

Similar to the binary system $N_2$-$CO_2$, the solid phase at the SLVE of the binary system $O_2$-$CO_2$ consists of pure carbon dioxide. Therefore, the phase equilibrium equations for $CO_2$ are described by Eqs 4-7 and 4-8; whereas that for $O_2$ is given by

$$\hat{f}_{O_2}^{V} = \hat{f}_{O_2}^{L} \qquad (6\text{-}4)$$

The fugacities of $CO_2$ can be estimated using Equations 4-1 through 4-4, whereas those of $O_2$ are estimated from

$$\hat{f}_{O_2}^{V} = y_{O_2}\hat{\varphi}_{O_2}^{V}P \qquad (6\text{-}5)$$

$$\hat{f}_{O_2}^{L} = x_{O_2}\hat{\varphi}_{O_2}^{L}P \qquad (6\text{-}6)$$

### 6.1.3 SLVE modelling of the binary system $N_2$-$O_2$

For the binary system $N_2$-$O_2$, no solid phase is present within the studied range of temperature. Therefore, only the vapour and liquid phases are present; and hence no need to optimize the model for the SVE or SLVE of this system. The PR EoS is capable of describing the vapour-liquid equilibria (VLE) of this system; and is already optimized with the interaction parameter $k_{ij}$ value of -0.0119 [96].

### 6.1.4 SLVE modelling of the ternary system $N_2$-$O_2$-$CO_2$

As per the degrees of freedom rule [97] when three components and three coexisting phases are present, the degree of freedom would be 2. Therefore, to study the SLVE locus for the ternary system $N_2$-$O_2$-$CO_2$, an equilibrium stage separation unit was modeled and used to construct the SLVE locus for three different mixtures of the ternary system (i.e., the solid, liquid and vapor phase mixtures). The temperature and pressure of the equilibrium stage separation unit are to be determined in order to determine the state of the corresponding system. The feed stream to the unit is separated at a certain temperature and pressure into either three phases (vapor, liquid and solid) or two phases (vapor and solid) depending on the corresponding conditions. In each case, the solid phase is assumed to consist of pure $CO_2$.

The system is modeled as an equilibrium stage separation unit, while assuming that the feed stream ($F$) consists of the feed compositions ($Z_i$). The material balance equations used for the first case (SLVE) are:

Total Material Balance: $F = V + L + S_{CO_2}$ (6-7)

Material Balance on $CO_2$: $Z_{CO_2}F = y_{CO_2}V + x_{CO_2}L + S_{CO_2}$ (6-8)

Material Balance on $N_2$: $Z_{N_2}F = y_{N_2}V + x_{N_2}L$ (6-9)

The corresponding phase equilibrium equations for $CO_2$ are given in Eqs 4-7 and 4-8, that for $N_2$ is given in Eq.6-1; and that for $O_2$ is given in Eq. 6-4. Additionally, the fugacity terms can be obtained from Equations 4-1 through 4-4 for $CO_2$, from Equations 6-2 and 6-3 for $N_2$ and from Equations 6-5 and 6-6 for $O_2$.

For the second case (VSE), the vapour phase will be present with the absence of liquid phase; the corresponding material balance equations are:

Total Material Balance: $F = V + S_{CO_2}$ (6-10)

Material Balance on $CO_2$: $Z_{CO_2}F = y_{CO_2}V + S_{CO_2}$ (6-11)

Material Balance on $N_2$: $Z_{N_2}F = y_{N_2}V$ (6-12)

The corresponding equilibrium equations for $CO_2$ is given by Eq. 4-8. Furthermore, the fugacity values of $CO_2$ in vapour and solid phases can be obtained from Eqs. 4-1 and 4-3, respectively; and those of $N_2$ and $O_2$ in the vapour phase can be obtained from Eqs. 6-2 and 6-5, respectively

## 6.2 Results and Discussion

### 6.2.1 Correlation of the binary system of $N_2$-$CO_2$

To the our knowledge, the data available by Schweitzer [58] and Fandino et al. [59] are the only experimental data available in the literature for SLVE of the $N_2$-$CO_2$ binary system. The data by Fandino et al. [59] is limited and only include only four points, while the data by Schweitzer include 14 points in the range of 12-130 bar. The studies discussing the SVE of the $N_2$-$CO_2$ binary system include those by Sonntag and Wylen [53], and Smith et al. [54]. The latter study covers the pressure range of 51-200 bar, while

that of Sonntag and Wylen [53] was conducted in the pressure range between 5 and 101 bar. Both studies reported the mole fraction of $CO_2$ in the vapor phase at temperatures between 140K and 190K. Due to their convenient ranges of conditions, our model will be optimized based on the SVE dataset by Sonntag and Wylen [53] in addition to the SLVE data by Schweitzer [58]. Therefore the optimized interaction parameter to be obtained would be applicable for both the SLVE locus and SVE regions. To optimize the model, it was first exported into the Aspen Plus simulator, where the Aspen Plus regression tool was used. The target was to better match the model predictions with data by Schweitzer for the SLVE locus [58] and Sonntag and Wylen [53] for the SVE region by manipulating the interaction parameter $k_{ij}$. The target was to minimize the value of the objective function as built in the Aspen Plus simulator. The objective function equation is described elsewhere [64].

The interaction parameter was varied between -0.1000 and +0.1000; and the results showed that the optimum interaction parameter $k_{ij}$ was +0.0405. Figure 6-1 shows the optimum model predictions versus the experimental data for the SLVE pressure-temperature (PT) locus, while Figure 5 is comparing the model predictions for the mole fraction of carbon dioxide in the vapor phase in the SVE region to laboratory data reported by Sonntag and Wylen [53].

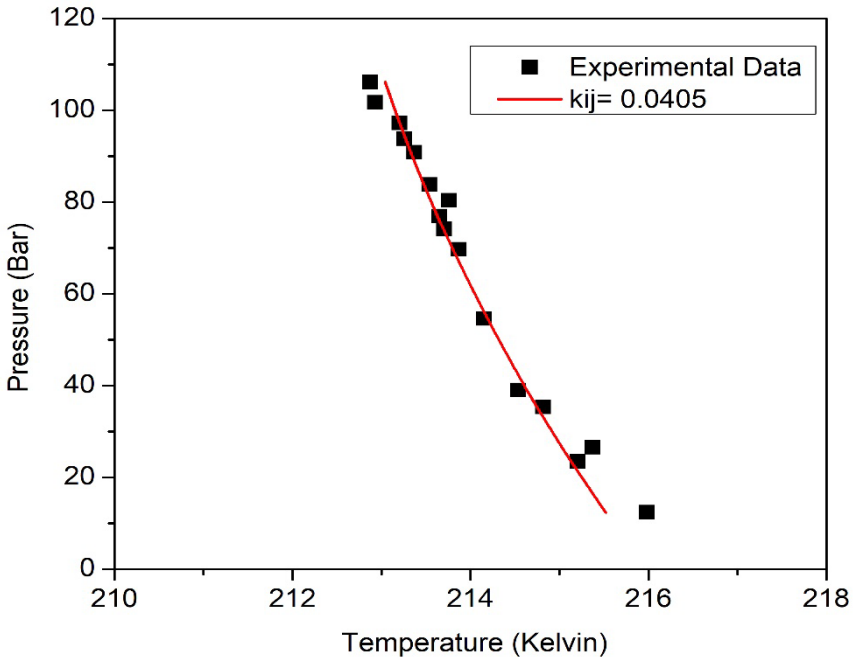


Figure 6-1: Comparison of model correlation of the SLVE PT locus (line) with the optimum kij value to the corresponding experimental data (symbols) for the binary system $N_2$-$CO_2$ [53].

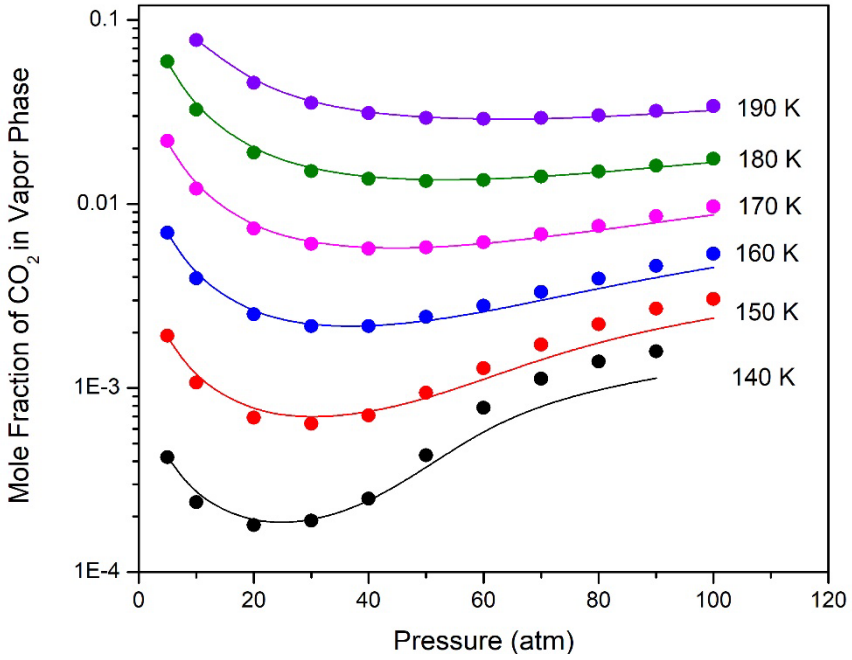


Figure 6-2: Comparison of model predictions (lines) and experimental data (symbols) [53] of the binary system $N_2$-$CO_2$ for the effect of temperature and pressure on composition of vapor phase in the SVE region.

It could be noticed from Figure 6-1 that the model has successfully generated the SLVE locus for the binary $N_2$-$CO_2$ binary system, and it was accurate in matching the experimental results as optimized by Aspen Plus. Figure 6-2 confirms the suitability of the model to represent this binary system in the SVE region; the model predictions for $y_{CO2}$ was accurate and matched the data reported by Sonntag and Wylen [53], especially at high temperatures (>170K) or at low temperatures (140-160K) and low pressures ( <50 atm).

### 6.2.2 Correlation of the binary system of $O_2$-$CO_2$

In the absence of experimental SLVE or SVE data for the binary $O_2$-$CO_2$ system, there is no reliable way to optimize the model to better predict this system behavior. However, to the authors' knowledge, only experimental SLE data is available for this binary system [55], [60], [61]. Riva [98] has regressed these SLE data to find the best

value for the interaction parameter. The PR EoS model was used for estimating the fugacities of vapor and liquid phases. Furthermore, the Zabaloy equation was used for the fugacity of the solid phase [80], but the Zabaloy equation was slightly modified as described therein [98]. This approach, which is almost similar to the approach used in this study, has been used model to the $CH_4$-$CO_2$ system, and the optimum value found by Riva et al. [4] was 0.119, which is very close to the corresponding results in our previous study [23], where the optimum interaction parameter value for the same system using the PR EoS was 0.120. Therefore, it is believed to be safe to use the optimum interaction parameter ($k_{ij}$) found by Riva [98] for the $O_2$-$CO_2$ system, which was 0.160 using the Zabaloy equation, in this study (which uses the PR EoS). Figure 6 shows the SLVE locus predicted by the model described in section 2.3 using this interaction parameter value ($k_{ij}$ =0.160).

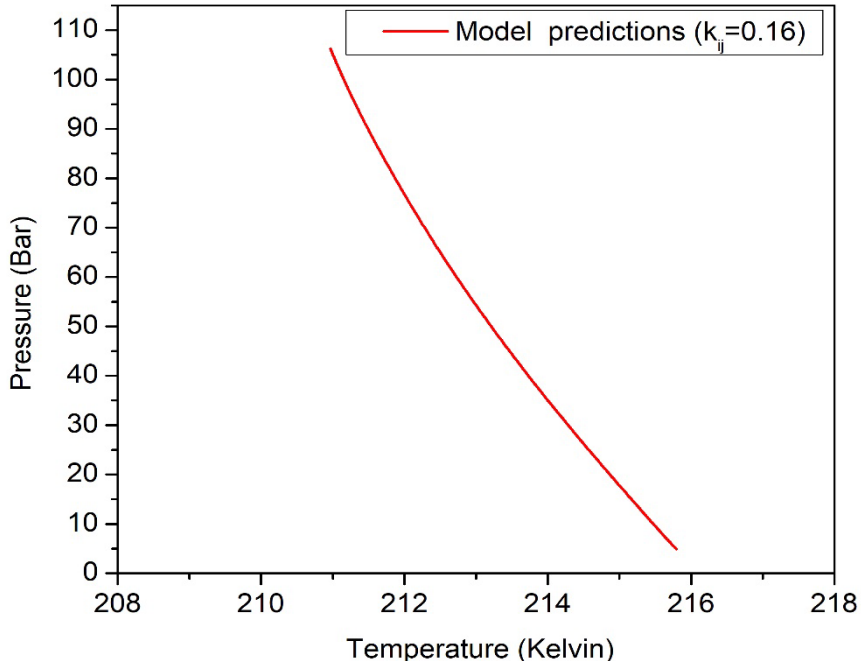


Figure 6-3: Model predictions for SLVE locus of the binary system $O_2$-$CO_2$

### 6.2.3 Predictions of the ternary system $N_2$-$O_2$-$CO_2$

To predict the SLVE and the SVE data for this ternary system as described in Section 2.4, the interaction parameters for the constituting binary systems ($N_2$-$CO_2$, $O_2$-$CO_2$ and $N_2$-$O_2$) are required. As described in the previous sections, the optimum interaction parameters chosen for the $N_2$-$CO_2$ and $O_2$-$CO_2$ binary systems were 0.0405 and 0.160, respectively. Moreover, since the discussed range of temperature in this study (>140K) is well above the triple point temperatures for $N_2$ (63.14 K [99]) and $O_2$ (54.33K [100]), it is not expected to exhibit a solid phase of wither nitrogen or oxygen in the binary system of $N_2$-$O_2$. Therefore, only the VLE of this system is exhibited, where the corresponding optimum interaction parameter ($k_{ij}$ = -0.0119) is used as already found by Sandler [96].

To construct the phase envelope for this ternary system three different feed composition were tested as shown in Table 6-1. Figure 6-4 shows the model-predicted phase diagrams for these three cases, where it is clear that the three different mixtures have almost the same SLVE line. However, the point where the SLVE line meets that of the SVE is quite different for different compositions. This meeting point will shift up or down (in pressure and temperature) depending on the ratio of $Z_{CO2}/Z_{N2}$ in the mixture. As this ratio increases, the meeting point will move down (lower pressure), moving towards the SVE for pure $CO_2$. On the other hand, increasing $Z_{O2}$ within the mixture would move SLVE line for the ternary system towards the SLVE line for binary system of $O_2$-$CO_2$. In general having more concentrations of the $O_2$ and $N_2$ gases would result in having “smaller” vapor-solid region, therefore in the systems where the $CO_2$ concentration is low, extra care should be taken in order to ensure operating within the SVE region.

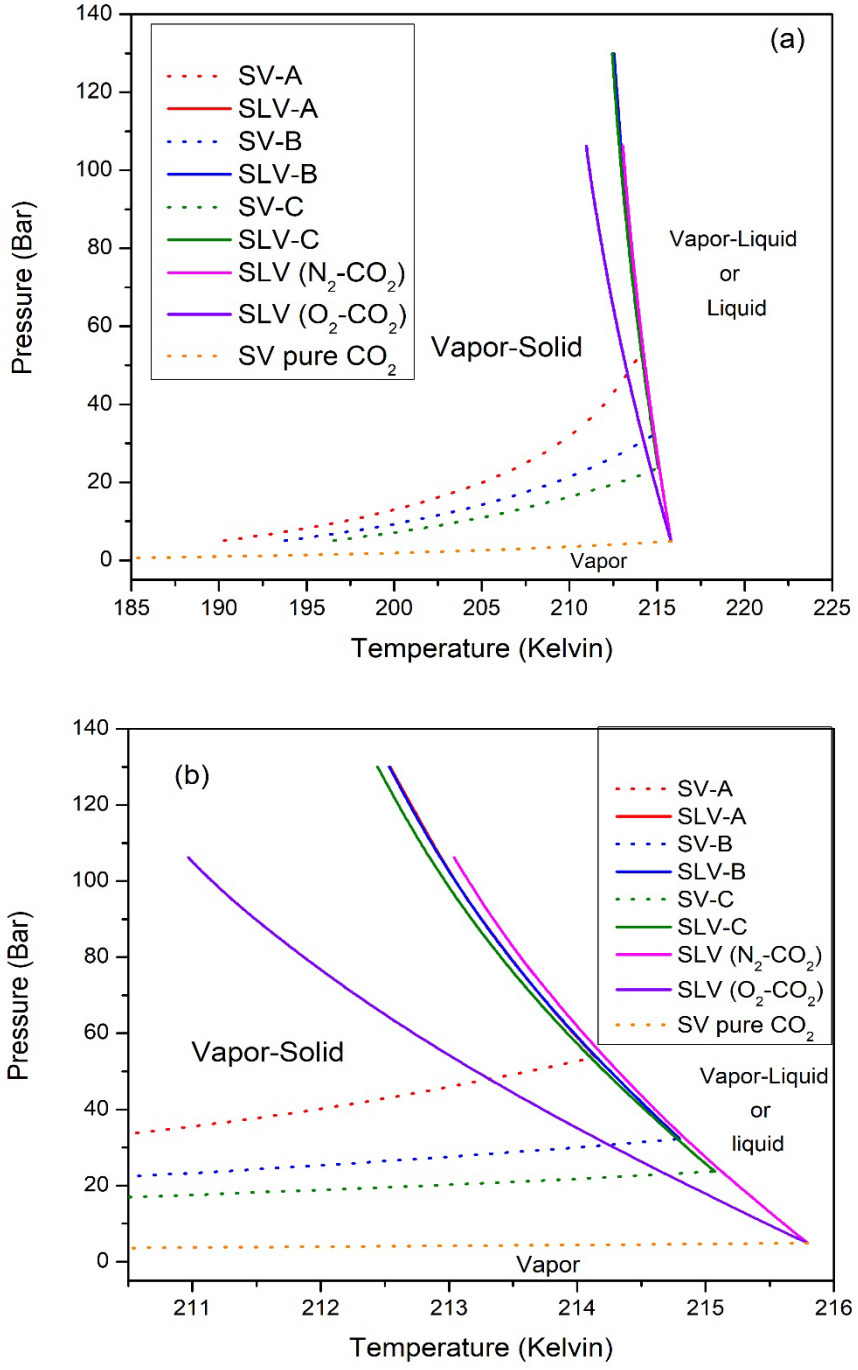


Figure 6-4: Pressure-Temperature phase diagrams for the three cases and compared to SLV locus lines for the binary systems; $N_2$-$CO_2$ and $O_2$-$CO_2$: (a) over the full range of temperature, and (b) zoomed in temperature range 210.5-216K

Table 6-1: Compositions of the feed mixtures utilized to construct the ternary system phase diagrams

| Case | $Z_{N2}$ | $Z_{O2}$ | $Z_{CO2}$ | $Z_{CO2}$ / $Z_{N2}$ | $Z_{CO2}$ / $Z_{O2}$ | $Z_{O2}$ / $Z_{N2}$ |
|---|---|---|---|---|---|---|
| A | 0.80 | 0.05 | 0.15 | 0.1875 | 3.000 | 0.0625 |
| B | 0.75 | 0.05 | 0.20 | 0.2667 | 4.000 | 0.0667 |
| C | 0.67 | 0.08 | 0.25 | 0.3731 | 3.125 | 0.1194 |

### 6.3 Comparison with other models for noble gases in nitrogen system

Not many studies in the published literature have studied the SLVE or SVE of flue gas. A recent study by De Guido and Pellegrini [101] has attempted to predict the SVE for flue gas mixtures using an approach based on the Peng Robinson equation of state [71]. Their proposed model was validated for the SVE data for the binary system $N_2$-$CO_2$, and was later utilized to predict the SVE for the ternary system $N_2$-$O_2$-$CO_2$. While the model proved successful, the study has not discussed SLVE for the systems, and it only considered one mixture of the ternary system (14.0% $CO_2$, 83.0% $N_2$ and 3.0% $O_2$ by mole). In a different study by Baxter et al. [102], a cryogenic $CO_2$ capture (CCC) process from flue gas was proposed by reaching the $CO_2$ anti-sublimation temperatures (-100 to -135 °C), hence converting $CO_2$ from the vapor phase into a solid phase. The process proved effective (with $CO_2$ recovery levels reaching 99%) while being energy-efficient. However, this study has not dealt with the SLVE nor attempted to construct the phase envelope for the ternary mixture $N_2$-$O_2$-$CO_2$. Moreover, it only reported the results of one composition of this ternary mixture.

The results of this model were compared and validated against those obtained by De Guido and Pellegrini [101]. The frost line predicted in this work is compared to that predicted by De Guido and Pellegrini in Figure 6-6a. In this study, it was found

that a part of the frost line (at pressures above 65.4 bar) would be an SLVE locus, while at lower pressures it exhibits an SVE locus line. This result is confirmed by the model as well as the experimental results of the binary system $N_2$-$CO_2$ [58], which is believed to have a similar behavior to this mixture. This is because the composition studied herein has a minimal concentration of oxygen (3%), hence its behavior will not deviate much from that of the binary system $N_2$-$CO_2$. Figure 6-6b compares the PT loci data corresponding to various recoveries of $CO_2$ in the solid phase as predicted by this work (solid line) and by De Guido and Pellegrini (dashed lines). The results prove that both models behave in very similar ways, especially at lower recoveries (90% and 95%). Nonetheless, a noticeable difference between the two models is noticed for the 99% recovery at high pressures. However, in the study of De Guido and Pellegrini, no attempts have been made to optimize the interaction parameters and their interaction parameter values were taken as-is from the Aspen HYSYS® V9.0 process simulator. Therefore, we believe that the results of this study are more accurate since the interaction parameters were optimized, and the frost line is a better representative of similar systems.

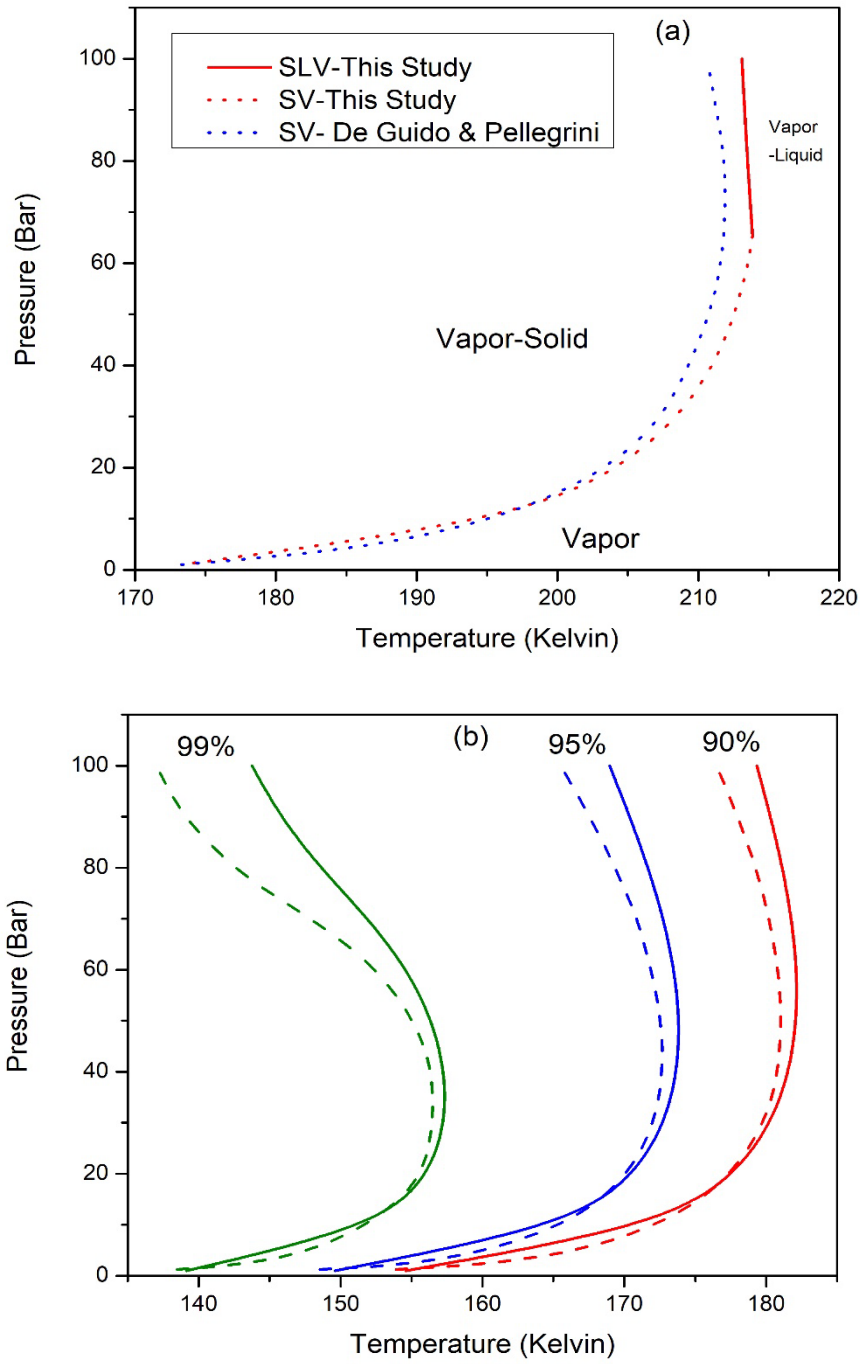


Figure 6-5: Comparison between results of this study and those of De Guido and Pellegrini study [101] for the CO2 recoveries of (a) 0% (frost line) and (b) 90% 95% and 99% recovery . Solid and dashed lines represent this study and the study of De Guido and Pellegrini, respectively [101]

# CHAPTER 7: DESIGN, MODELING, AND SIMULATION OF SV SEPARATION UNIT

The previous chapters developed an empirical correlation model based on the Peng–Robinson equation of state (PR EoS), which was able to describe the solid–liquid–vapour equilibria (SLVE) for the ternary systems of $CH_4$-$CO_2$-$H_2S$, $N_2$-Kr-Xe, and $N_2$-$O_2$-$CO_2$. Additionally, they suggested an equilibrium stage separation unit based on that model to separate sour gases from methane, noble gases from nitrogen and capture dioxide from flue gas. The SLVE and the separation unit were simulated using Aspen Custom Modeler (ACM) software. It was concluded that conducting the separation in the solid–vapor equilibrium (SVE) regions would produce higher-purity products and higher recovery for unwanted gases when compared to the SLVE region. The studies discussing the cryogenic separation using SVE are very limited, Maqsood et al. [103] developed a hybrid cryogenic network for separating $CO_2$ from a $CH_4$-$CO_2$ mixture. The network consists of a packed bed and a cryogenic separator. The study was conducted in vapor–solid (packed bed) vs. vapor–liquid (VL) (cryogenic separator) and vapor–liquid–solid (VLS) (combination of the two units) phase regions. The results indicated that energy consumption was about 37% of the energy required by conventional cryogenic distillation network. However, this study only dealt with the $CH_4$-$CO_2$ binary mixture; but was not expanded to include the binary mixture of $CH_4$-$H_2S$ nor the ternary mixture of $CH_4$-$CO_2$-$H_2S$ gases. Furthermore, the results were not compared to the industry-common amine sweetening process. Tuinier et al. [104] have developed a cyclic process to capture $CO_2$ from flue using cryogenically cooled packed beds. However, in their study, the flue gas mixture consists of $H_2O$, $N_2$, and $O_2$ but have not studied the impact of oxygen in the flue in the mixture. They estimated that cooling duty to recover >99% $CO_2$ from a flue gas (10% $CO_2$, 1% $H_2O$, and 89% $N_2$) is 1.8 MJ/kg $CO_2$. They further developed their process in a different study [105], and used

cryogenic packed beds to capture $CO_2$ from biogas stream. Their study [105] focused on the $CH_4/CO_2$. Their results indicate that the energy duty is 2.9 MJ to recover one kg of methane from a feed consisting of 45 vol % $CO_2$ and 55 vol % $CH_4$. Unfortunately, these studies do not discuss the liquid and solid formation during the process, nor cover the thermodynamic sides of the process.

In this chapter, we build on the conclusion of the previous chapters, and a solid–vapor (SV) separation unit is further developed, with additional energy balance calculations for the unit added to the ACM model. The ACM model is successfully exported to the Aspen Plus environment. The performance of the SV separation unit is analyzed, optimized, and compared to other traditional gas sweetening, and carbon capture separation technologies (such as amine scrubbing), in terms of the product quality, removal ratio of acid gases, and the energy requirements.

### 7.1 Modeling of the SV separation unit

Figure 7-1 shows a schematic diagram of the suggested separation unit. It involves two scenarios; the first involves an expansion valve on the feed stream leading to directly to the separation unit, while the second has no expansion valve. The expansion valve (i.e., the first scenario) is needed when the original feed is in liquid phase, and thus evaporation is required. On the other hand, the second scenario (without an expansion valve) will correspond to cases when the original feed is already in the gas phase. The separation unit involves a solid–vapor equilibrium (SVE) separation zone and a heated melting tray beneath the SVE zone.

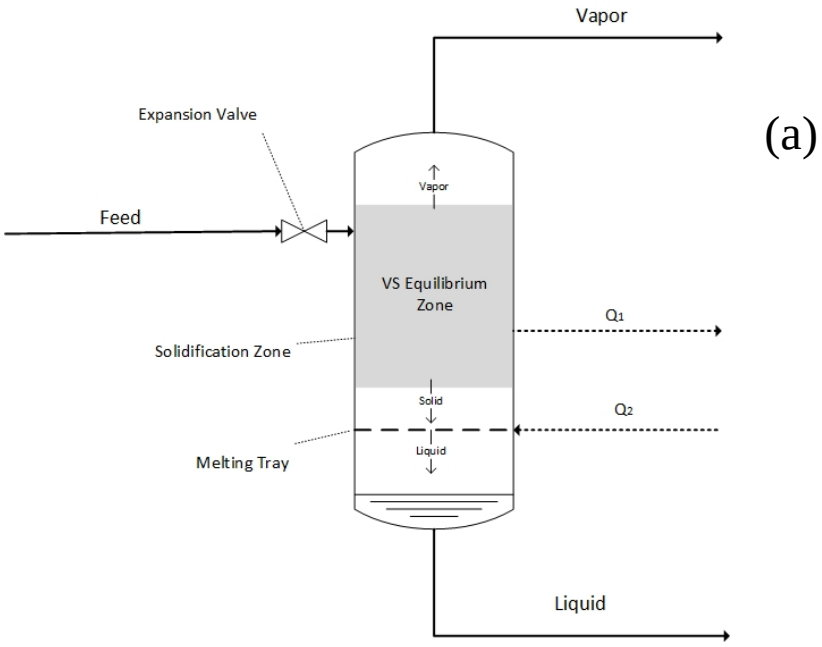


(a)

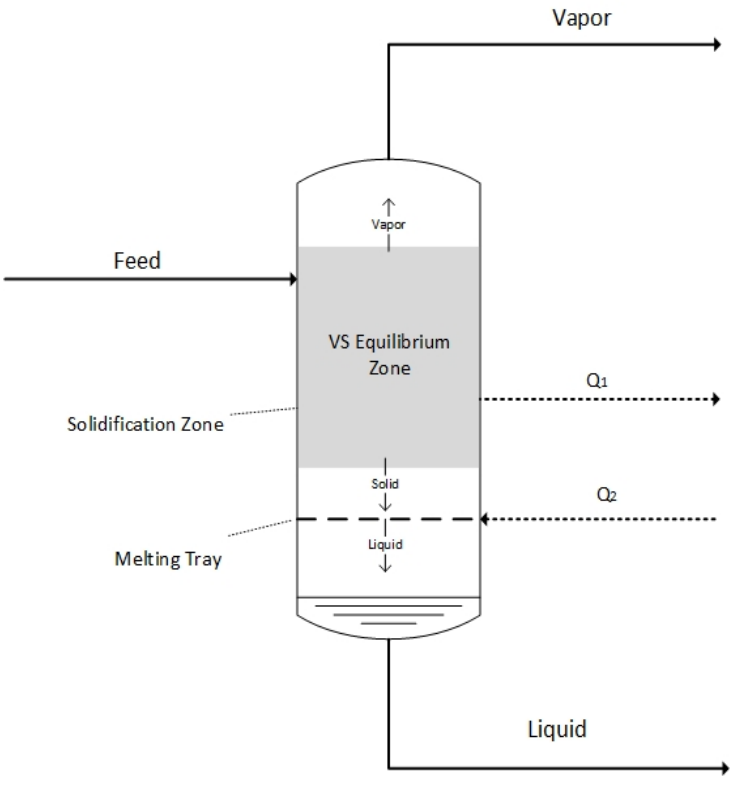


(b)

Figure 7-1: Schematic diagram for the suggested SV separation unit (a) with an expansion valve, and (b) without an expansion valve.

In the case of the gas sweetening process, the first scenario (involving an expansion valve on the feed stream prior to its entry to the separation unit) is used. The feed, which should initially be in liquid phase is throttled using the expansion valve. Ideally, the throttling process is performed adiabatically, but subsequent cooling ($Q_1$) might be required to either ensure that its temperature drops to a condition that corresponds to the SVE zone (where $CH_4$ remains in the vapor phase and only $CO_2$ and $H_2S$ solidify partially. Figure 7-2 further explains this process. The conditions of the feed stream (point "1") are transformed to reach point "2", at which the mixture enters the solidification zone of the SV separation unit, and the separation of acid gases into a solid phase is achieved. The formed solids (in the SVE zone) descend due to their higher densities, reaching the melting tray, which is supplied with sufficient heat ($Q_2$) to melt the solids into a liquid stream. The formed liquid stream (consisting only of $CO_2$ and $H_2S$) can be collected at the bottom of the unit, whereas high-purity methane gas is collected at the top of the unit. The second scenario of the SV unit (Figure 7-1b) is used for the separation of the noble gases from nitrogen and to capture $CO_2$ from flue gas streams. Further details of the process is discussed in the subsequent sections.

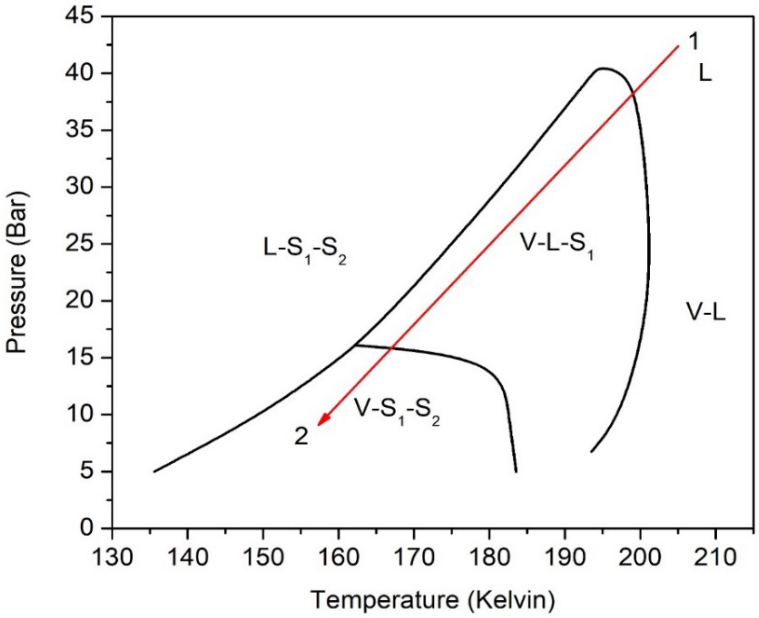


Figure 7-2: A simplified path for the throttling/equilibrium process (red line) versus the SLVE phase diagram. Phases: V: vapor, L: liquid, $S_1$: solid $CO_2$, $S_2$: solid $H_2S$.

The separation unit has two heat utility streams: $\dot{Q}_1$ and $\dot{Q}_2$. The first heat utility stream ($\dot{Q}_1$) is for cooling the feed stream to achieve the needed temperature of the SVE zone, whereas the second heat utility stream ($\dot{Q}_2$) is for heating required to melt the solid $CO_2$ formed in the SVE zone. Figure 3 better explains the mass and energy flow schemes for the SV separation unit.

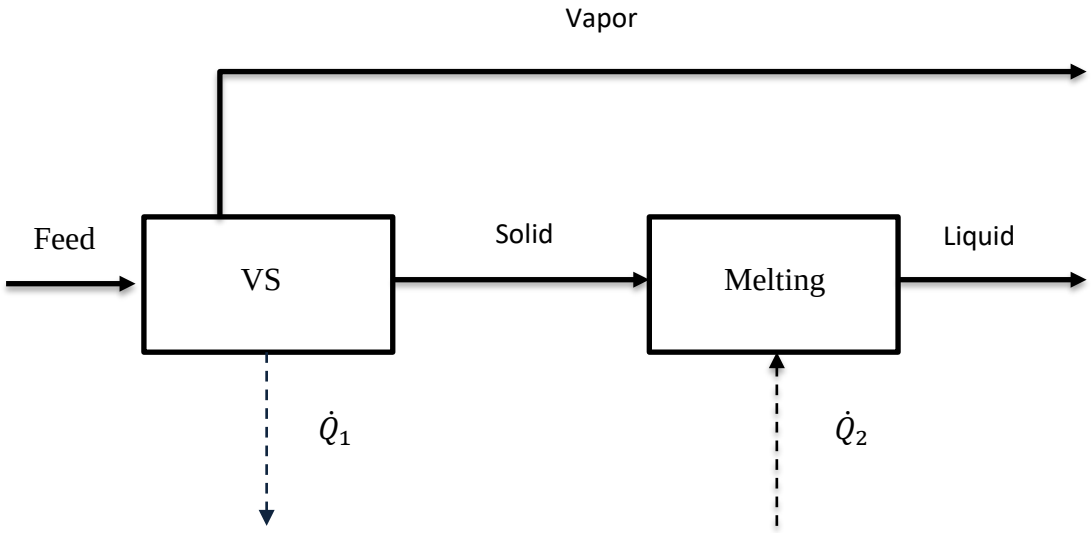


Figure 7-3: Simplified mass and energy flows for the SV separation unit, where $\dot{Q}_1$ is the cooling rate for the feed stream and $\dot{Q}_2$ is the heating rate required to melt the solid formed in the SVE zone into a liquid stream.

### 7.1.1 Modeling of SV unit for the natural gas system[8]

The material balance equations for the SV separation unit for this system are given by:

Total Material Balance: $$\dot{n}_{Feed} = \dot{n}_{Vapor} + \dot{n}_{Liquid} \quad (7\text{-}1)$$

Material Balance on $CH_4$: $$z_{CH_4}\dot{n}_{Feed} = y_{CH_4}\dot{n}_{Vapor} \quad (7\text{-}2)$$

Material Balance on $CO_2$: $$z_{CO_2}\dot{n}_{Feed} = y_{CO_2}\dot{n}_{Vapor} + x_{CO_2}\dot{n}_{Liquid} \quad (7\text{-}3)$$

$$\dot{n}_{Liquid} = \dot{n}_{Solid} = \dot{n}_{Solid-CO_2} + \dot{n}_{Solid-H_2S} \quad (7\text{-}4)$$

$$x_{CO_2} + x_{H_2S} = 1 \quad (7\text{-}5)$$

$$y_{CH_4} + y_{CO_2} + y_{H_2S} = 1 \quad (7\text{-}6)$$

[8] H. Ababneh, A. AlNouss, I. A. Karimi, and S. A. Al-Muhtaseb, "Natural Gas Sweetening Using an Energy-Efficient, State-of-the-Art, Solid and Vapor Separation Process," *Energies*, vol. 15, no. 14, 2022, doi: 10.3390/en15145286.

$$x_{CO_2} = \frac{\dot{n}_{Solid-CO_2}}{\dot{n}_{Solid}} \quad (7\text{-}7)$$

where $\dot{n}_{Feed}$, $\dot{n}_{Vapor}$ and $\dot{n}_{Solid}$ are the total molar flow rates of the feed stream, vapour stream and solid (or liquid) streams, respectively; and $z_i$ is the mole fraction of the component *i* in the feed.

Steady-state energy balances on the two subsystems illustrated in Figure 7-3 are given by

$$\dot{Q}_1 = \dot{H}_{Feed} - (\dot{H}_{Vapor} + \dot{H}_{Solids}) \quad (7\text{-}8)$$

$$\dot{Q}_2 = \dot{H}_{liquid} - \dot{H}_{Solids} \quad (7\text{-}9)$$

where $\dot{H}_{Feed} = \dot{n}_{Feed} h_{Liquid}(T_{Feed}, P_{Feed})$ (7-10)

$$\dot{H}_{Vapor} = \dot{n}_{Vapor}\, h_{Vapor}(T, P) \quad (7\text{-}11)$$

$$\dot{H}_{liquid} = \dot{n}_{Liquid} h_{Liquid}(T, P) \quad (7\text{-}12)$$

and $\dot{H}_{Solids} = \dot{n}_{Solid\_CO_2} h_{Solid\_CO_2} + \dot{n}_{Solid\_H_2S} h_{Solid\_H_2S}$ (7-13)

where $\dot{H}$ is the enthalpy flow rate, *h* is the molar enthalpy of the component/stream, $h_{Vapor}$ is the molar enthalpy of the vapor stream emerging from the SVE unit. While $h_{Liquid}$ and $h_{Solid}$ are, respectively, the molar enthalpies of the liquid stream emerging from the melting tray and the solid stream entering to the melting tray at *T* and *P*. They are determined at the corresponding conditions by the built-in Aspen Plus models. Furthermore, the molar enthalpies of the solid phase can be estimated by

$$h_{Solid\_CO_2}(T, P) = h_{Vapor\_CO_2}(T, P) - \Delta h^{sub}_{CO_2} \quad (7\text{-}14)$$

$$h_{Solid\_H_2S}(T, P) = h_{Vapor\_H_2S}(T, P) - \Delta h^{sub}_{H_2S} \quad (7\text{-}15)$$

where $\Delta h_i^{sub}$ is the enthalpy of sublimation of the component $i$; which equals 28.83 kJ/mol for $CO_2$ [106], and 23.8 kJ/mol for $H_2S$ [107].

### 7.1.2 Modeling of SV unit for the noble gases in nitrogen

The material balance equations for the SV separation unit are given by

Total Material Balance: Equation 7-1

Material Balance on $N_2$: $z_{N_2}\dot{n}_{Feed} = y_{N_2}\dot{n}_{Vapor}$ (7-16)

Material Balance on Kr: $z_{Kr}\dot{n}_{Feed} = y_{Kr}\dot{n}_{Vapor} + x_{Kr}\dot{n}_{Liquid}$ (7-17)

$$\dot{n}_{Liquid} = \dot{n}_{Solid} = \dot{n}_{Solid-Kr} + \dot{n}_{Solid-Kr} \quad (7\text{-}18)$$

$$x_{Kr} + x_{Xe} = 1 \quad (7\text{-}19)$$

$$y_{N_2} + y_{Kr} + y_{Xe} = 1 \quad (7\text{-}20)$$

$$x_{Kr} = \frac{\dot{n}_{Solid-Kr}}{\dot{n}_{Solid}} \quad (7\text{-}21)$$

where $\dot{n}_{Feed}$, $\dot{n}_{Vapor}$ and $\dot{n}_{Solid}$ are the total molar flow rates of the feed stream, vapour stream and solid (or liquid) streams, respectively; and $z_i$ is the mole fraction of the component *i* in the feed.

Steady-state energy balances on the two subsystems illustrated in Figure 7-3 are given 7-8 to 7-12, plus Equation 7-22.

$$\dot{H}_{Solids} = \dot{n}_{Solid\_Kr}h_{Solid\_Kr} + \dot{n}_{Solid\_Xe}h_{Solid\_Xe} \quad (7\text{-}22)$$

Furthermore, the molar enthalpies of the solid phase can be estimated by

$$h_{Solid\_Kr}(T,P) = h_{Vapor\_Kr}(T,P) - \Delta h_{Kr}^{sub} \quad (7\text{-}23)$$

$$h_{Solid\_Xe}(T,P) = h_{Vapor\_Xe}(T,P) - \Delta h_{Xe}^{sub} \quad (7\text{-}24)$$

where $\Delta h_i^{sub}$ is the enthalpy of sublimation of the component $i$; which equals 11.53 kJ/mol for Kr , and 15.79 kJ/mol for Xe [106].

### 7.1.3 Modeling of SV unit for the flue gas system[9]

Figure7-2b shows a schematic diagram of the SV separation unit used for $CO_2$ capture from flue gas. The separation unit consists of a solid-vapor equilibrium (SVE) separation zone and a heated melting tray underneath the equilibrium zone to melt the solid phase to be collected as a liquid. The feed stream enters the unit at its operating pressure and at a low temperature (in the range of 200-230K), so it will be close the solidification temperature, which is usually from 200-215K. In the SVE zone (where only $CO_2$ solidifies; and nitrogen, oxygen and traces of $CO_2$ remain in the vapor phase). The temperature is further dropped by cooling (with a cooling rate of $\dot{Q}_1$) to ensure that the unit is operating in the SVE zone. The solid $CO_2$ would descend down due to its higher density, reaching the melting tray, at which a heating rate ($\dot{Q}_2$) is supplied to melt the solid $CO_2$ into a liquid stream. The formed liquid stream can be collected at the bottom of the unit, while the top vapor stream will consist mostly of $N_2$ and $O_2$.

In the SVE solidification zone, the equilibrium equations were discussed in the previous chapter 6. Furthermore, the material balance equations for the SV separation unit are given by

Total Material Balance: Equation 7-1

Material Balance on $N_2$: $Z_{N_2}\dot{n}_{Feed} = y_{N_2}\dot{n}_{Vapor}$ (7-25)

Material Balance on $CO_2$: Equation 7-3

where $\dot{n}_{Liquid} = \dot{n}_{Solid} = \dot{n}_{Solid-CO_2}$ (7-26)

$$x_{CO_2} = 1 \quad (7\text{-}27)$$

$$y_{N_2} + y_{CO_2} + y_{O_2} = 1 \quad (7\text{-}28)$$

$\dot{n}_{Feed}$, $\dot{n}_{Vapor}$ and $\dot{n}_{Solid}$ are the total molar flow rates of the feed stream, vapour stream

[9] This chapter was taken from the article currently under review: H. Ababneh, A. AlNouss, and S. A. Al-Muhtaseb, "Carbon Capture from Post Combustion Flue Gas Using a State-of-the-Art, Anti-Sublimation, Solid-Vapor Separation Unit"

and solid (or liquid) streams, respectively; and $Z_i$ is the mole fraction of the component $i$ in the feed. These cooling and heating rates can be estimated from the following steady-state energy balances on the two subsystems illustrated in Figure 7-3 are given 7-8 to 7-12, plus Equation

$$\dot{H}_{Solids} = \dot{n}_{Solid\_CO_2} h_{Solid\_CO_2} \quad (7\text{-}29)$$

where the molar enthalpy of the solid phase can be estimated from Equation 7-14.

## 7.2 Results and Discussion

### 7.2.1 Natural gas sweetening process[10]

The SV separation unit model was exported to Aspen Plus for simulation. The following three feed compositions (mole%) were tested:

- Feed **A** (80% $CH_4$, 10% $CO_2$, 10% $H_2S$)
- Feed **B** (80% $CH_4$, 15% $CO_2$, 5% $H_2S$)
- Feed **C** (70% $CH_4$, 17.5% $CO_2$, 12.5% $H_2S$)
- Feed **C'** (70% $CH_4$, 17.5% $CO_2$, 12.5% $H_2S$) with additional cooling

The feeds at 80 bar and 200K were throttled to 10 bar to assure that the SV unit is in the SVE zone as illustrated in Figure 7-2 and predicted in this study. The overall performance results are also listed in Table 7-1. It is noticed from Table 7-1 that when the methane composition in the feed stream is high (such as cases A and B), the sweet gas (vapor outlet) stream would have a higher purity of methane. However, when a sourer gas is fed to the unit (such as in Case C), methane purity in the outlet vapor would be relatively low. Therefore, an optimization of the operation condition, for

[10] H. Ababneh, A. AlNouss, I. A. Karimi, and S. A. Al-Muhtaseb, "Natural Gas Sweetening Using an Energy-Efficient, State-of-the-Art, Solid and Vapor Separation Process," *Energies*, vol. 15, no. 14, 2022, doi: 10.3390/en15145286

example by adjusting the temperature of SV equilibrium unit (cooling the it down) or adding another SV separation unit could be added, if required.

Table 7-1: Results for the tested three feed compositions

| Feed | | A | B | C | C' * |
|---|---|---|---|---|---|
| *T* (K) after throttle valve | | 161.3 | 168.0 | 182.2 | 165.0 |
| Heat Transfer Rate (W/kmol Feed) | $\dot{Q}_1$ | 0 | 0 | 0 | 486 |
| | $\dot{Q}_2$ | 552 | 617 | 780 | 885 |
| Vapor Phase Composition (mol%) | $CH_4$ | 99.2 | 98.4 | 94.1 | 98.9 |
| | $CO_2$ | 0.5 | 1 | 4.1 | 0.7 |
| | $H_2S$ | 0.3 | 0.6 | 1.8 | 0.4 |
| Liquid Phase Composition (mol%) | $CO_2$ | 49.6 | 75.7 | 56.6 | 58.2 |
| | $H_2S$ | 50.4 | 24.3 | 43.4 | 41.8 |
| Removal Ratio in Liquid Phase (%) | $CO_2$ | 96.2 | 94.6 | 82.7 | 97.1 |
| | $H_2S$ | 97.6 | 90.9 | 88.9 | 97.6 |
| | $CO_2$+$H_2S$ | 96.9 | 93.7 | 85.3 | 97.3 |

* The feed C' represents another run of the feed "C", but with subsequent cooling ($Q_1$).

The first option for optimization (further cooling of the feed stream) is demonstrated in case C', where the feed was cooled down to 165 K (in addition to being adiabatically throttled). The purity of the produced methane improves significantly to about 99%, while the gas removal ratios have also increased significantly. However, a cooling rate ($\dot{Q}_1$) of 485 W/(mole of the feed) is needed, whereas a higher heating rate ($\dot{Q}_2$) was needed for the melting the acid gases as a results of higher solidification amounts of $CO_2$ and $H_2S$. More detailed considerations of various scenarios to optimize this process, along with a comparison to the conventional absorption process, will be addressed in a future work.

A traditional amine-sweetening unit was simulated using the Aspen Hysys® software. Two different feed compositions (with low and high concentrations of acid gases), where the compositions represent actual natural gas streams extracted in state of Qatar, were tested. Furthermore, in this study only $CH_4$, $CO_2$, and $H_2S$ gases were considered, and the compositions were normalized to exclude other trace gases (such as $C_{2+}$). The two cases of tested feed stream compositions and conditions are presented in Table 7-2.

Table 7-2: Dry basis compositions of the two tested feeds and their specifications.

| Feed | | Case 1 | Case 2 |
|---|---|---|---|
| Dry feed composition | $CH_4$ | 96.19% | 89.27% |
| | $CO_2$ | 2.87% | 5.88% |
| | $H_2S$ | 0.94% | 4.85% |
| Feed flow rate | kg/hr | 287640 | 287640 |
| | kmol/hr | 16905.1 | 15496.1 |
| Feed conditions | Temperature (°C) | 40 | |
| | Pressure (bar) | 45 | |

The targeted goal is to produce sweetened gas stream with a minimum purity of 99.7%. Many technologies are used for the acid gas removal from NG, with amine scrubbing (physicochemical absorption) being the most common technique [24]. Among the common amine technologies used is the Sulfinol process, which utilizes blends of Sulfolane (as a physical solvent) and diisopropanolamine (DIPA) (as a chemical solvent) [108]. This process is preferred in LNG applications, as sulfur compounds are more soluble in this blended solvent than in aqueous amines, and solvent loadings are better, especially at greater acid gas partial pressures [109]. Additionally, it requires lower circulation rates, it is less corrosive than other types of amine, hence needing smaller equipment and lower capital cost [110]. Figure 7-4 shows a traditional

acid gas treatment flowsheet employing Sulfolane and DIPA as a chemical solvent at high pressure to remove $H_2S$ and $CO_2$ from sour gas. The sour gas is fed into a high-pressure absorber (45 bar), which purifies the natural gas mixture to the sales gas specification. Then, acid gases are stripped from the rich amine in a regenerator column, which operates at a low pressure (2 bar) and high temperature (135 °C) and recycles the Sulfolane and DIPA lean solvent (with potential makeup) back to the absorber column.

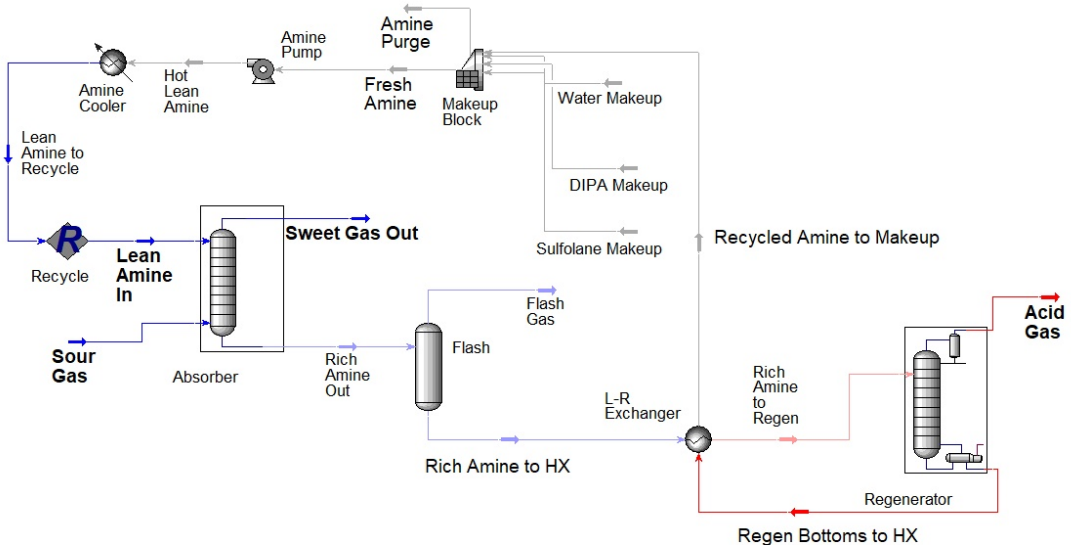


Figure 7-4: Process flow diagram of the simulated optimized amine sweeting unit for natural gas sweetening.

Figure 7-5 illustrates the process flow diagram of the SV separation unit. A feed gas at the same conditions (40 °C and 45 bar) is fed to a compressor, where its pressure is from 45 bar to 70-90 bar. Following that, the sour gas is cooled and liquefied to 210 K. The liquid mixture is then throttled adiabatically just before the entrance of the SV unit, and cooled further if deemed necessary (e.g., to improve the SV separation). Vapor-solid separation takes place in the SV unit, and the sweet gas flows to the top of the unit, while the sour gases are collected at the bottom of the unit in liquid phase (as explained in section 7.2.1.1).

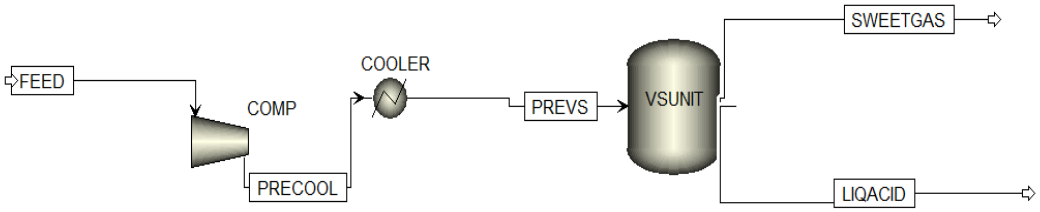


Figure 7-5: Process flow diagram of the SV separation unit for natural gas sweetening

*7.2.1.1 Sensitivity Analysis and Optimization of SV Separation Unit*

The impact of the compressor discharge pressure and the throttling pressure in the SV separation unit on the overall energy consumption of the process was studied, while maintaining the targeted purity level (99.7% pure $CH_4$). The results are presented in Figures 7-6 and 7-7. It is noticed from Figure 7-6 that increasing the compressor pressure increases the total energy requirement significantly, which is due to (1) the higher work for the compressor itself and (2) higher cooling rate at the cooler as a result of the higher temperature and pressure of the sour gas discharged from the compressor. Although the higher pressure has a negligible impact on $\dot{Q}_2$ (SV unit heating rate), it has a noticeable impact on the $\dot{Q}_1$ of the SV unit (again, as result of the higher pressure of the feed coming into the SV unit; which requires more cooling to reach the targeted purity). On the other hand, Figure 7-7 shows that the throttling pressure of the feed to the SV separation unit has less impact on the total energy rate requirements. The higher the throttling pressure lowers the cooling rate needed within the SV separation unit ($\dot{Q}_1$), while there is no change in the cooling needed upstream of the unit or heating within the SV unit itself. The SV separation unit is to be optimized (with the target of minimizing the energy consumption while achieving the needed purity) by manipulating both the throttling pressure of the SV separation unit and the compressor

pressure. The optimization results for feed “A” are seen in Figure 7-8, where the minimum energy consumption is achieved when the compressor discharge pressure is decreased and the throttling pressure is increased.

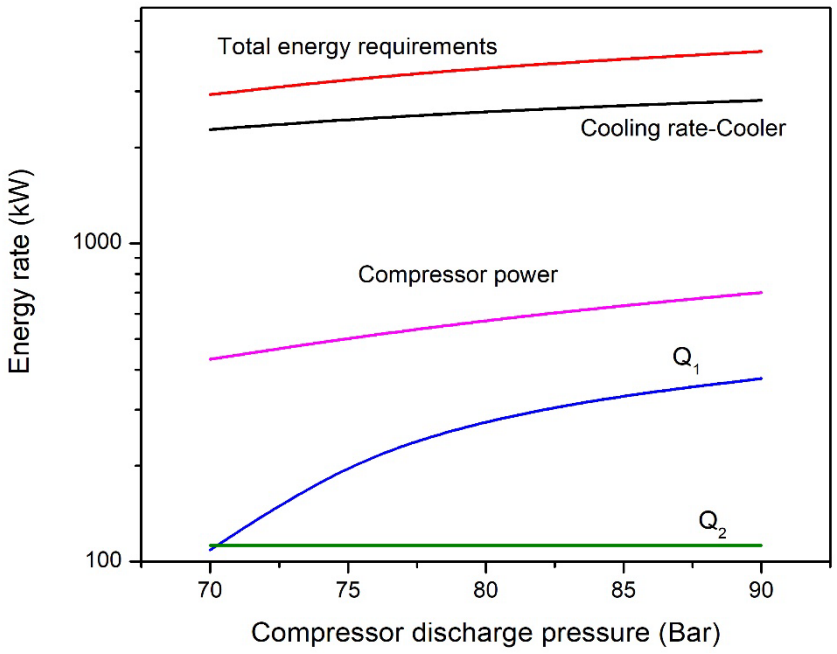


Figure 7-6: Impact of the compressor discharge pressure on the SV separation unit’s energy requirements.

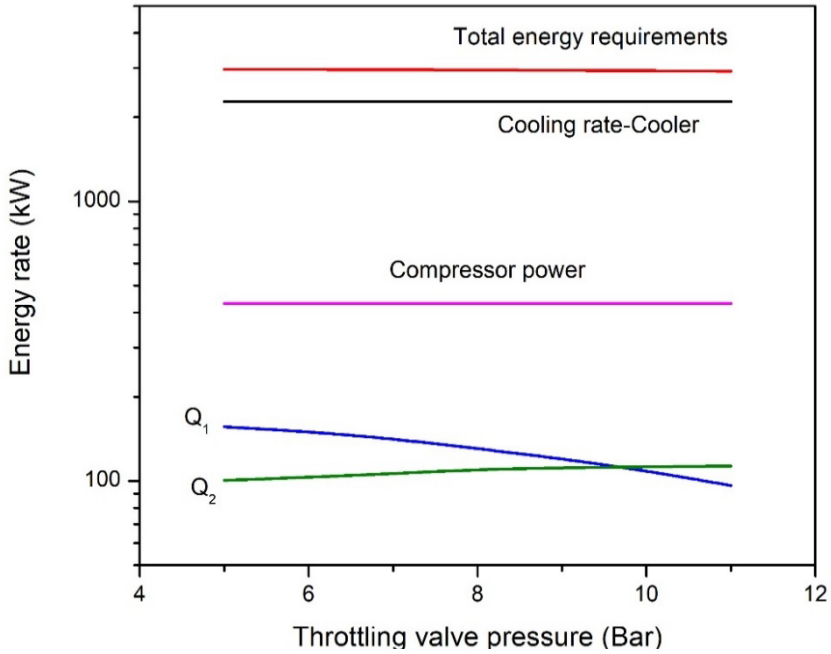


Figure 7-7: Impact of the throttling valve pressure on the SV separation unit's energy requirements.

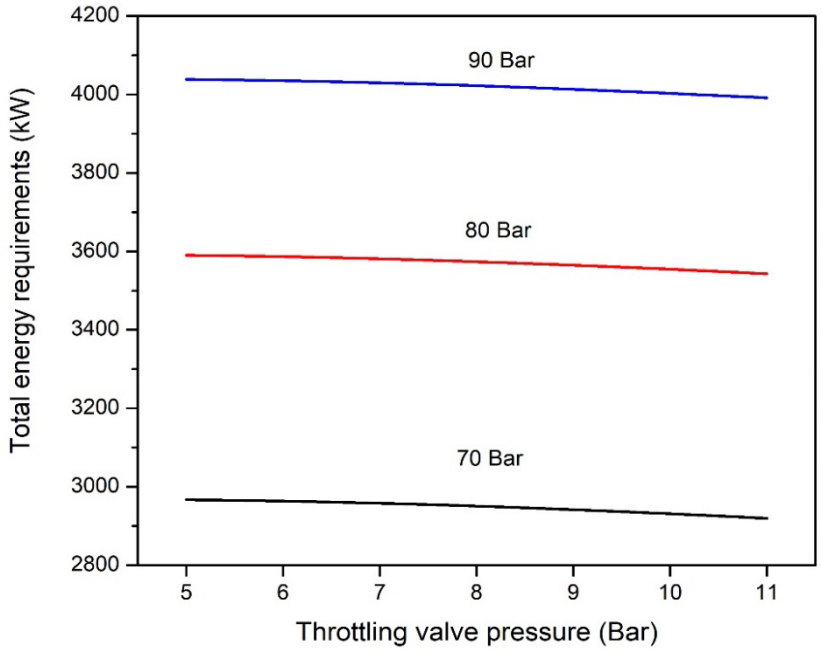


Figure 7-8: Combined impact of compressor discharge pressure (different lines) and throttling pressure of the SV unit on the total energy requirements of the SV process-case A.

*7.2.1.2 Comparison between amine sweeting unit and the SV unit*

The two processes (the SV separation process and amine absorption process) were compared to each other on the same basis, using the same feed flow rate, compositions and conditions as seen in Table 7-2. The optimized results of the traditional amine sweetening unit are summarized in Table 7-3, while the optimized results for the SV separation unit PFD are presented in Table 7-4. Even though the amine sweetening unit is able to achieve higher molar removal levels of acid gases compared to SV unit, the presence of water in the sweet gas stream (resulting from the evaporation of water in the used solvent mixture) means that further processing might be needed to remove it. Additionally, the sweet gas would be at a relatively high temperature ≈ 50 °C, which means that cooling might be needed if the sweet gas is to be liquefied.

Comparing the total energy requirements of the two processes shows that the SV separation process requires only 26-27% of the energy needed for the amine sweeting process as noticed in Tables 7-3 and 7-4, indicating one of the main advantages that the SV separation process offers over the traditional amine units. Additionally, the SV separation process requires lower number of equipment units, eliminates the need for corrosive solvents which damage the equipment over time and avoids contaminating the sweet gas product with water moisture. Therefore, the SV separation process has lower capital and operational costs in comparison to the traditional absorption processes.

Table 7-3: Optimized results of the Amine sweetening unit

| | | Case 1 | Case 2 |
|---|---|---|---|
| Solvent | | Sulfolane -DIPA | |
| Solvent flow rate | kg/hr | 52201.28 | 93296.03 |
| | kmol/hr | 784.5 | 1402 |
| Sweet gas composition | $CH_4$ | 99.67% | 99.74% |
| | $CO_2$ | 0.0020% | 0.0004% |
| | $H_2S$ | 0.0657% | 0.0005% |
| | $H_2O$ | 0.2667% | 0.2625% |
| Molar removal | $CO_2$ | 99.93% | ≈100% |
| | $H_2S$ | 93.28% | ≈100% |
| Energy requirements (kW) | Reboiler | 5835 | 6112.3 |
| | Condenser | 3428.6 | 3300.1 |
| | Pump | 78.8 | 140.7 |
| | Cooler | 1530.7 | 2636.9 |
| | Total | 10873.1 | 12189.9 |
| Sweet gas conditions | Temperature (K) | 323.54 | 323.19 |
| | Pressure (bar) | 45 | 45 |

Table 7-4: Optimized results of the SV separation unit

| | | Case 1 | Case 2 |
|---|---|---|---|
| Temperature after throttle valve (K) | | 153.6 | |
| Vapor Phase Composition (mol%) | $CH_4$ | 99.7000% | 99.7000% |
| | $CO_2$ | 0. 1737% | 0. 1737% |
| | $H_2S$ | 0.1263% | 0.1263% |
| Liquid Phase Composition (mol%) | $CO_2$ | 76.7620% | 54.7203% |
| | $H_2S$ | 23.2380% | 45.2797% |
| Molar removal (%) | $CO_2$ | 94.2% | 97.36% |
| | $H_2S$ | 87.03% | 97.67% |
| Energy requirements (kW) | Compressor | 431.95 | 427.85 |
| | Cooler | 2278.57 | 2590.68 |
| | $\dot{Q}_1$ | 96.40 | 93.88 |
| | $\dot{Q}_2$ | 113.12 | 301.43 |
| | Total | 2920.05 | 3226.08 |
| Sweet gas conditions | Temperature (K) | 153.63 | |
| | Pressure (bar) | 11 | |

### 7.2.2 Noble gases in nitrogen system

The SV separation unit model discussed in chapter 5 was exported from the ACM to Aspen Plus environment for simulation. To separate both noble gases (Kr and Xe) from the nitrogen, the separation unit should operate in the phase equilibrium region where both of these two gases would freeze. Such phase equilibrium region is denoted as $VS_2S_3$, as discussed previously, Since the $VS_2S_3$ region for the ternary

system $N_2$-Kr-Xe is small, and it was impractical to construct the phase envelope for this system as explained in details in section 6.1.4 , only one feed was tested in the corresponding SV separation unit, with the following composition (mole%):

- Feed (50% $N_2$, 30% Kr, 20% Xe)

It should be noted that the compositions suggested here may not be realistic and does not necessarily represent the actual gas streams, where the actual gas streams contains much lower concentrations of noble gases. This composition was chosen so that the performance of the SV unit could be easily studied upon selective solidification of the two noble gases. The initial feed at 1 bar and 298.15K was compressed to 1.5 bar, and then cooled to 200 K; where the feed will still be in vapor phase (at 1.5 bar and 200 K). To assure that the SV unit operates in the SVE region of the phase envelope, the temperature in the SV unit is dropped to about 100 K. Figure 7-9 shows the process flow diagram of SV separation unit, while Figure 7-10 illustrates the process path of the SV separation on the phase diagram.

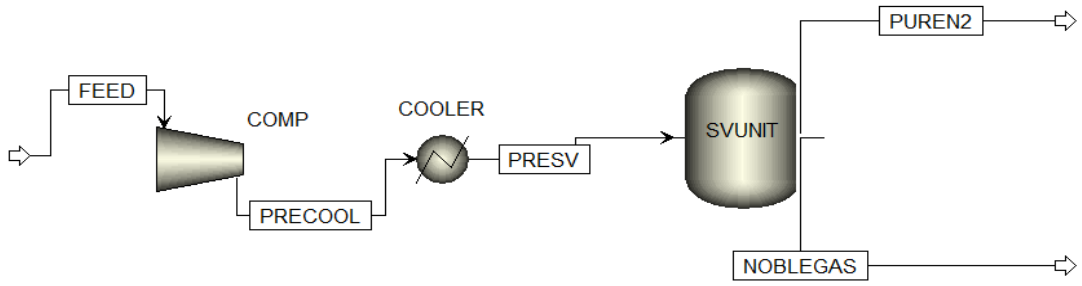


Figure 7-9: Process flow diagram of the SV separation unit removing noble gases from nitrogen

As result of the very small $VS_2S_3$ region (where the pressure and temperature can be changed only within 1- 2 bars and between 80-105K, respectively), not much could be done in terms of optimizing this system. The above mentioned feed was tested,

and the results obtained a summarized in Table 7-5.

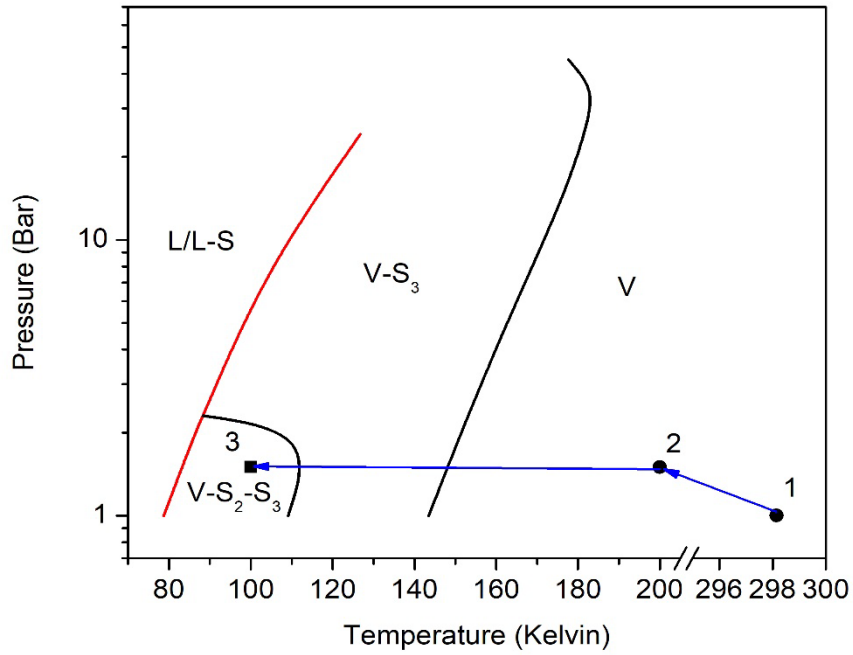


Figure 7-10: A simplified process path line (blue line) for the noble gas separation from nitrogen using the SV separation unit versus the SLVE phase diagram. Point 1 resembels the intial feed condition, point 2 resembels the feed after compression and cooling, and point 3 resembles the conditions in the SV separation unit

Table 7-5: Results for SV unit to separate noble gases from nitrogen

| Property | | Value |
|---|---|---|
| Feed Composition (mole%) | $N_2$ | 50% |
| | Kr | 30% |
| | Xe | 20% |
| Feed flow rate | kg/hr | 100 |
| | kmol/hr | 6540.5 |
| Feed conditions | Temperature (K) | 298.15 |
| | Pressure (bar) | 1 |
| Output vapor phase composition (mol%) | $N_2$ | 91.5% |
| | Kr | 8.4% |
| | Xe | 0.1% |
| Output liquid phase composition (mol%) | Kr | 56% |
| | Xe | 44% |
| Noble gas recovery (ratio removed from feed) | Kr | 84.6% |
| | Xe | 99.9% |
| Energy requirements (kW) | Compressor | 41.5 |
| | Cooler | 110.2 |
| | $\dot{Q}_1$ | 240.6 |
| | $\dot{Q}_2$ | 31.7 |
| | Total | 424 |
| Output gas conditions | Temperature (K) | 100 |
| | Pressure (bar) | 1.5 |

It could be noticed from Table 7-5 that the recovery for Xe is much higher than that of Kr, which could be attributed to the fact that the triple point temperature of Xe (161.4 K [111]) is higher than that for Kr (116 K [112]). Therefore, at the operating temperature (100 K), which is slightly below the triple point of Kr; a significant portion of Kr is still in the vapor phase, while over 99% of Xe was solidified and removed.

The total energy consumption was 424 kW. Cooling in the cooler and in the SV unit were the major contributors of energy consumption (constituting 83% of the total energy consumption). This is explained by the need to drop the temperature to 100 K, which requires high cooling loads. Unfortunately, to our knowledge, there are no other common industrial separation technologies used to separate such mixture of noble gases from nitrogen. Hence, unlike the other two studied systems (sweetening of natural gas and removal of carbon dioxide from flue gas mixtures), the developed SV separation unit for this system was not compared to other technologies. Overall, such SV separation units have proven the potential to be used in similar systems; such as air separation.

### 7.2.3 Flue gas system[11]

The SV separation unit model discussed in chapter 6 was exported from the ACM to Aspen Plus environment for simulation. The following two feed compositions (mole%) were tested:

- Case **1** (86.9% $N_2$, 11.0% $CO_2$, 2.1% $O_2$)
- Case **2** (71.8% $N_2$, 24.7% $CO_2$, 3.5% $O_2$)

These flue gas compositions represent typical dry-basis gas compositions found in the energy industry [16]; where Cases 1 and 2 represent relatively low and high concentrations of $CO_2$ in the feed, respectively. Table 7-6 summarizes the feed properties for the two cases.

Table 7-6: Dry basis compositions and specifications of the tested flue gas feeds.

| Feed | | Case 1 | Case 2 |
|---|---|---|---|
| Dry feed composition | $N_2$ | 86.9% | 71.8% |
| | $O_2$ | 2.1% | 3.5% |
| | $CO_2$ | 11.0% | 24.7% |
| Feed flow rate | kg/hr | 2986 | 3210 |
| | kmol/hr | 100 | |
| Feed conditions | Temperature | 280 °C (553.15 K) | |
| | Pressure | 1 atm (1.01325 bar) | |

[11] This chapter was taken from the article currently under review: H. Ababneh, A. AlNouss, and S. A. Al-Muhtaseb, "Carbon Capture from Post Combustion Flue Gas Using a State-of-the-Art, Anti-Sublimation, Solid-Vapor Separation Unit"

Figure 7-11 illustrates the process flow diagram of the $CO_2$ capture process using the SV separation unit. The flue gas feed, which is at 1 atm and 553.15K was compressed to a pressure between 5 and 50 bar using a compressor. Then, it was cooled down isobarically to a temperature of about 210 K before entering the SV unit, while the temperature is further dropped (to 140-190K) to make sure that the unit is operating in SVE region.

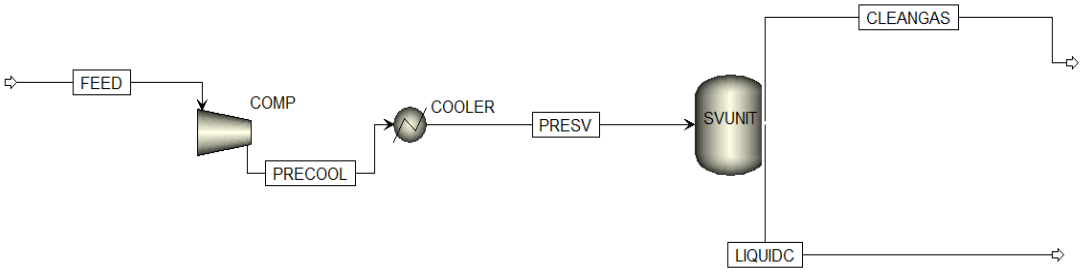


Figure 7-11: Process flow diagram of the SV $CO_2$ capture process

*7.2.3.1 Sensitivity Analysis and Optimization of SV Separation Unit*

To study the performance of the SV unit, two sensitivity analysis tests were conducted on one of the cases, i.e., "Case 1" presented above in Table 7-6, as an example to study the effects of the compressor discharge pressure and SV operating temperature on (1) the composition of $CO_2$ in the effluent output gas stream and (2) the energy requirements for each of the compressor, cooler, and heater; as well as the overall energy consumption.

The first sensitivity analysis studied the effect of compressor discharge pressure (SV unit pressure) and the SV unit's operating temperature on the composition of the $CO_2$ in the output clean gas stream. Figure 7-12 illustrates the results of the first sensitivity analysis tool; where increasing the operating temperature in the SV unit results in increasing the $CO_2$ composition in clean gas stream emerging from the unit

(i.e., reducing $CO_2$ recovery). Contrary to that is the relationship between the compressor discharge pressure with the mole fraction of $CO_2$ in the output gas stream; where increasing the discharge pressure decreases the mole fraction of $CO_2$ in the output gas stream. Nevertheless, the impact of pressure is less significant than that of temperature. For example, increasing the pressure from 10 to 30 bar would decrease the mole fraction of $CO_2$ in the output gas stream from 0.004 to 0.0021 (≈ 50% reduction). However, raising the operating temperature form 160 to 180K at 30 bar would increase the $CO_2$ content in the output gas stream by 7 folds.

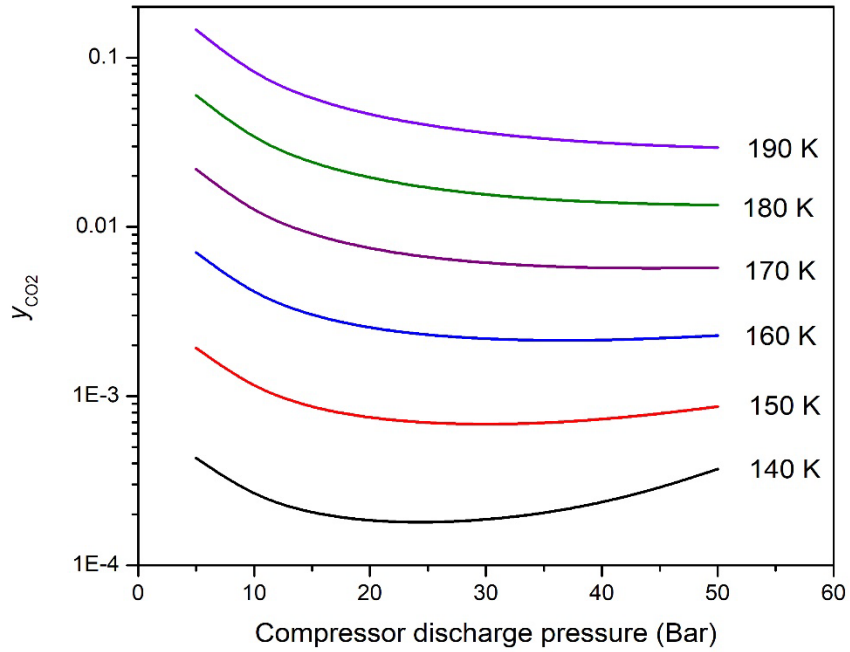


Figure 7-12: The impact of compressor discharge pressure at different SV operating temperatures on the $CO_2$ composition in the output clean gas stream.

The second sensitivity analysis test aims to study the impact of the same manipulated variables on compressor power, cooling rate in the cooler, cooling rate in the SV unit ($\dot{Q}_1$), heating rate needed for melting the solids ($\dot{Q}_2$), and the overall process energy consumption. The analysis results are shown in Figures 7-13 and 7-14. Figure 7-13a shows the impact of compressor discharge pressure on the energy consumption

of the SV separation process, while the unit temperature is fixed at the average value of 160K. It is clear from the figure that increasing the pressure would increase all of the energy consumption components (cooler cooling rate, compressor work, $\dot{Q}_1$ and $\dot{Q}_2$); and as results, it would significantly raise the overall energy requirements. Higher discharge pressures would require more power to compress the flue gas, and more cooling rate in the cooler (since it would raise the temperature of the flue gas exiting from the compressor). However, the discharge pressure has a minimal effect on $\dot{Q}_1$ and $\dot{Q}_2$ when the SV temperature is fixed. While both cooling and heating rates ($\dot{Q}_1$ and $\dot{Q}_2$) would increase, their change is not significant since the operating temperature of the unit is more influential on in its energy requirements as to be observed in Figure 7-13b. In Figure 7-13b, the operating temperature was altered while maintaining the compressor discharge pressure at an average value of 30 bars. No change was observed in the energy rates consumed by the compressor or the feed cooler at different SV unit operating temperatures since both of these process components are upstream of the SV unit. However, both of $\dot{Q}_1$ and $\dot{Q}_2$ have slightly dropped with the increase of the temperature. The drop of $\dot{Q}_1$ results from the lower cooling rates needed to achieve higher operating temperature, and that of $\dot{Q}_2$ results from the less amount of solid $CO_2$ formed in the unit at higher operating temperature, hence less energy is needed to melt it.

Figure 7-14 shows the combined impact of both the compressor's discharge pressure and SV unit operating temperature on the overall energy rate requirements by the process. Overall, the discharge pressure has a more significant impact on the overall energy rate needed for the process when compared to the unit operating temperature. Furthermore, the overall energy requirement decreases by reducing the compressor discharge pressure and/or increasing the SV separation process temperature.

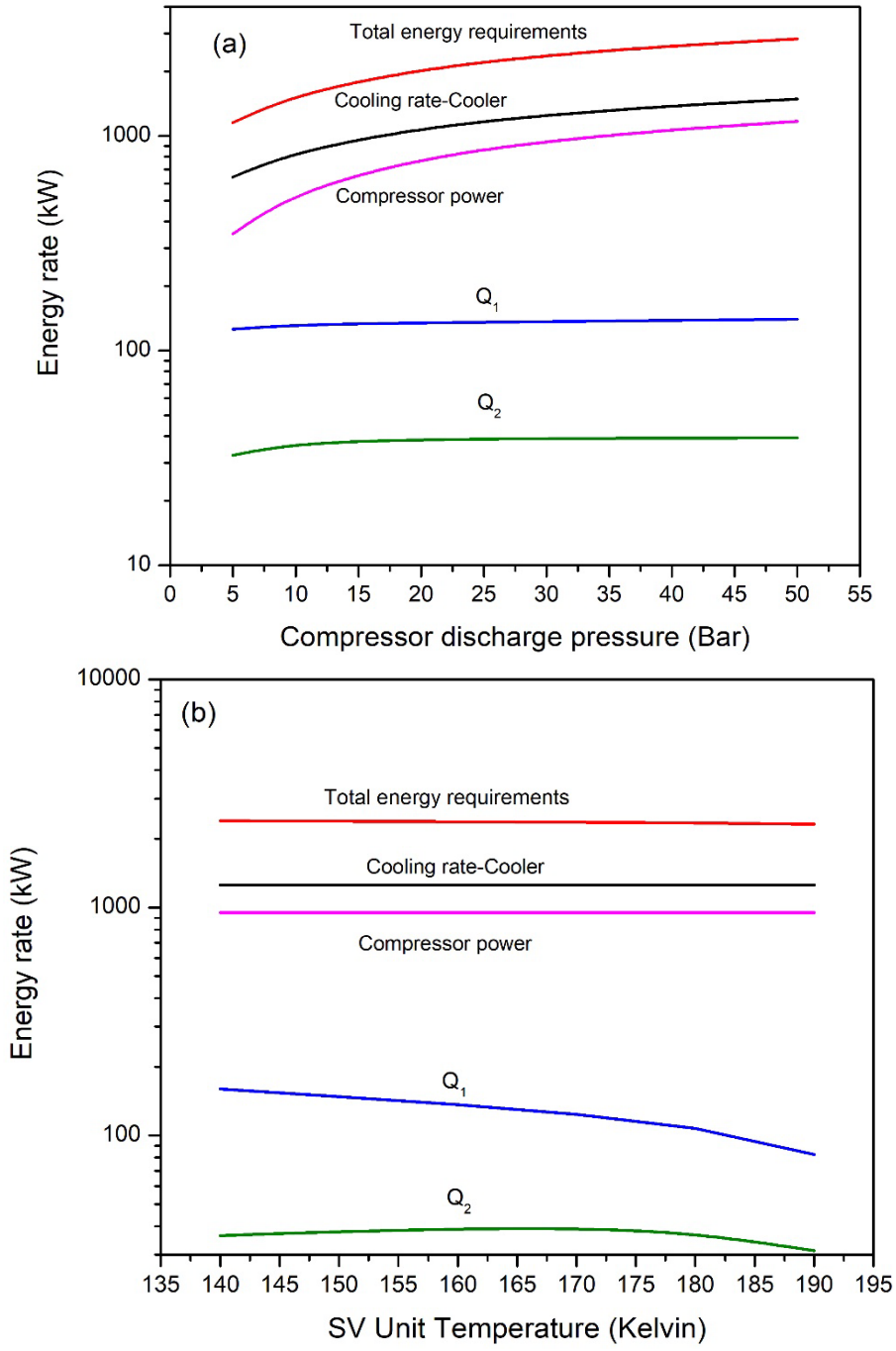


Figure 7-13: Impact of (a) compressor discharge pressure (at an SV process operating temperature of 160 K) and (b) SV unit operating temperature (at a compressor discharge pressure of 30 bar) on the energy consumption elements of the SV $CO_2$ capture process.

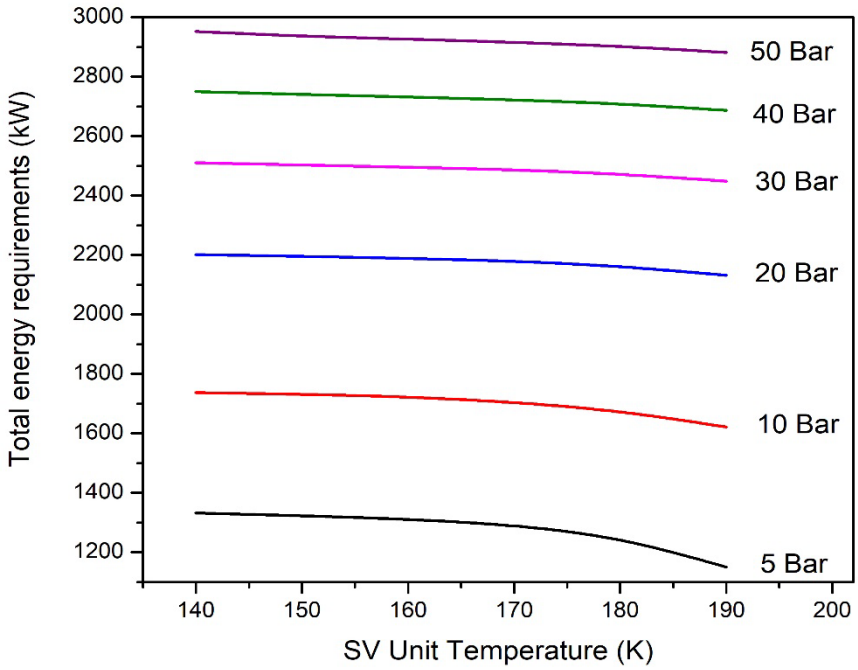


Figure 7-14: Combined Impact of compressor discharge pressure and SV unit operating temperature on the total energy rate consumption of the SV $CO_2$ capture process

*7.2.3.2 Comparison with amine-based $CO_2$ capture unit*

An industry-common amine-based $CO_2$ capture unit was simulated using the Aspen Hysys® software. Figure 7-15 shows the process flow diagram of this $CO_2$ capture process, which consists of a traditional gas-liquid acid gas absorption process at high pressure that uses N-methyldiethanolamine (MDEA) as a chemical solvent to remove $CO_2$ from the flue gas stream. MDEA is a highly selective solvent that is commonly used to treat sour gases and removes a large proportion of the $CO_2$ in the feed gas from the system [113]. It is also a key ingredient in many specialty amine formulations designed for deeper $CO_2$ removal in applications such as synthesis gas production and treating high concentrations of $CO_2$ in natural gases found in various parts of the world [114]. In recent years, however, attempts have been made to use

solvents containing only MDEA for $CO_2$ removal from high concentration gases, typically at high pressures [114]. In this process, the flue gas is cooled (to a temperature of 311 K) and pressurized (to a pressure of 57 bar) before being fed to the high-pressure absorber, where the $CO_2$ gas is removed. Acid gases are then stripped from amine by a regenerator column operating at low pressure (1.5 bar) and high temperature (120 °C) using MDEA solvent, which is recycled back to the absorber column with makeup fresh solvent.

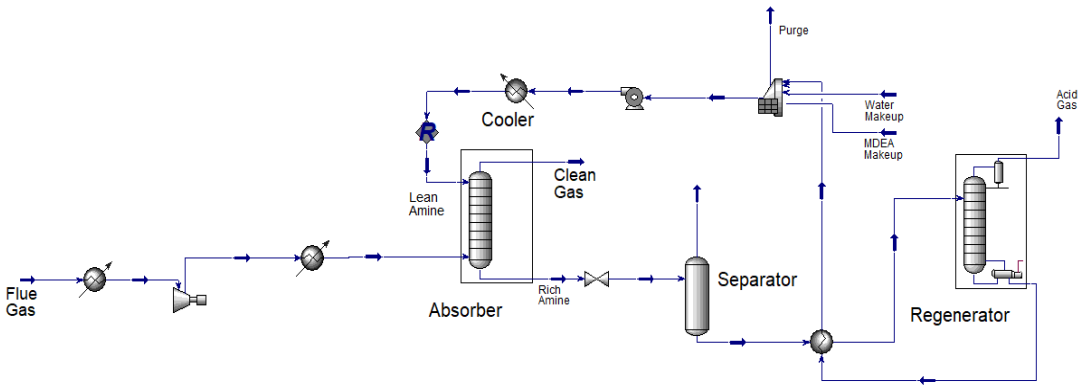


Figure 7-15: Process flow diagram of the MDEA $CO_2$ capture process

The two processes (the novel SV separation process studied in this work and the commercial amine absorption process) were compared to each other on the same basis, using the same feed flow rate, compositions and conditions of the two cases presented in Table 7-6. The target was to achieve a clean gas output stream with a $CO_2$ mole fraction that does not exceed 0.3%, while optimizing each process by minimizing the overall energy consumption. The optimized results of the traditional amine $CO_2$ capture unit and those for the optimized SV separation unit are presented in Tables 7-7 and 7-8, respectively.

Table 7-7: Results for the optimized amine-based $CO_2$ capture process.

| | | Case 1 | Case 2 |
|---|---|---|---|
| Solvent | | MDEA | |
| Solvent flow rate | kg/hr | 4168.5 | 9178.2 |
| | kmol/hr | 143.0 | 314.5 |
| Output gas composition | $N_2$ | 97.1% | 94.9% |
| | $O_2$ | 2.4% | 4.6% |
| | $CO_2$ | 0.3% | 0.3% |
| | $H_2O$ | 0.2% | 0.2% |
| $CO_2$ recovery (ratio removed from the feed) | $CO_2$ | 97% | 99.1% |
| Energy requirements (kW) | Flue gas Cooler 1 | 214.2 | 226.4 |
| | Flue gas Compressor | 680.2 | 657.8 |
| | Flue gas Cooler 2 | 687.2 | 670.1 |
| | Reboiler | 259.2 | 369.4 |
| | Condenser | 137.0 | 109.2 |
| | Pump | 8.4 | 18.6 |
| | Amine Cooler | 102.0 | 232.6 |
| | Total | 2088.1 | 2284.1 |
| Output clean gas conditions | Temperature (K) | 316.93 | |
| | Pressure (bar) | 56.17 | |

Table 7-8: Results of the optimized SV separation unit

| | | Case 1 | Case 2 |
|---|---|---|---|
| Output clean gas phase composition (mol%) | $N_2$ | 97.3% | 95.1% |
| | $O_2$ | 2.4% | 4.6% |
| | $CO_2$ | 0.3% | 0.3% |
| $CO_2$ recovery (ratio removed from feed) | $CO_2$ | 97% | 99.1% |
| Energy requirements (kW) | Compressor | 350.7 | 345.3 |
| | Cooler | 644.1 | 653.7 |
| | $\dot{Q}_1$ | 134.4 | 245.8 |
| | $\dot{Q}_2$ | 33.1 | 75.3 |
| | Total | 1162.1 | 1320.4 |
| Output clean gas conditions | Temperature (K) | 153.4 | |
| | Pressure (bar) | 5 | |

A comparison of the total energy requirements of the two processes shows that the novel SV process developed in this work consumes less energy when compared to the conventional amine-based process. Tables 7-7 and 7-8 show that the energy savings by the novel SV separation process ranges between 42% and 44% for Case 2 and Case 1, respectively.

Overall, we may conclude that $CO_2$ capture using the novel SV separation process offers many benefits compared to conventional amine-based process. The first benefit is the lower energy consumption, hence lower operational costs, than the conventional amine-based process. The second is the elimination of solvent handling equipment, therefore requiring a lower capital cost. This factor would further help avoid

contaminating the product gas stream with steam or solvent vapors. Also, lower corrosion rates are anticipated in the units of the novel SV separation process since solvents are no longer required and due to the lower operating temperature.

# CHAPTER 8: CONCLUSIONS & FUTURE WORK

## 8.1 Conclusions

In this study, an empirical phase equilibrium correlation model was developed based on the Peng-Robinson equation of state (PR EoS), with fugacity expressions to describe the solid-fluid phase for the ternary systems of $CH_4$-$CO_2$-$H_2S$, $N_2$-Kr-Xe, and $N_2$-$O_2$-$CO_2$ over wide ranges of pressure and temperature; and at different sets of feed compositions. In the natural gas system ($CH_4$-$CO_2$-$H_2S$); the model was first tested on the binary systems $CH_4$-$CO_2$, $CH_4$-$H_2S$ and $CO_2$-$H_2S$; and was found successful in predicting the corresponding solidification points and their compositions when optimizing the corresponding interaction parameters. Therefore, it was further expanded in a predictive manner to the ternary system $CH_4$-$CO_2$-$H_2S$. An equilibrium stage separation unit was used to study the separation of three different feed compositions, and was used to construct the phase envelope of this ternary mixture and study the impact of operating parameters on separation and recovery of $CO_2$, $H_2S$, and $CH_4$.

In this study, for the first time, an empirical correlation model was developed to predict the SLVE for the ternary system of nitrogen-krypton-xenon ($N_2$-Kr-Xe). To test the model accuracy and performance, it is first used to predict the SLVE locus of the binary systems Kr-$N_2$ and Xe-$N_2$ and Kr-Xe. The results were compared to the experimental data available in the literature, and the model proved to be successful in predicting the SLVE locus when the corresponding interaction parameters were optimized. Afterwards, the model was used for describing the SLVE behavior of the ternary system $N_2$-Kr-Xe with optimized interaction parameters. The predicted SLVE locus results of this ternary system were compared to a limited set of experimental data that is available in the literature. Furthermore, an equilibrium stage separation unit

model was utilized to construct the phase envelope of this ternary system at a sample overall composition. However, in the absence of reliable data, it was not possible to confirm the accuracy of the constructed phase envelope.

The thermodynamic model developed was able to predict and describe the solid-fluid phase equilibria of the ternary system of the flue gas components (i.e., $N_2$-$O_2$-$CO_2$). The study covered wide ranges of pressure (from 5 to 130 bar) and temperature (140 to 220 K). Then, the model was optimized by applying it to selected pairs of the binary systems forming the flue gas with a possibility to form solid $CO_2$ (i.e., $N_2$-$CO_2$ and $O_2$-$CO_2$), where the optimum interaction parameters were determined to be 0.0405 and 0.1600, respectively. The model proved to be successful in predicting the phase diagrams for these binary systems and for the ternary system ($N_2$-$O_2$- $CO_2$).

It was concluded that conducting the separation in the solid–vapor equilibrium (SVE) region would produce high-purity products and high recovery for the unwanted gases (such as $CO_2$ and $H_2S$), or desired gases (such as Kr and Xe). Therefore, based on that conclusion, solid–vapor (SV) separation units are further developed, with additional energy balance calculations for the units, and were added to the ACM model. The ACM model is successfully exported to the Aspen Plus simulation environment, and sample performance results are presented herein. The performance of the SV separation unit is analyzed, optimized, and compared to other traditional $CO_2$ capture, and gas sweetening units used in the industry (such as amine scrubbing). Comparisons were in terms of the product quality, removal ratio of acid gases and the energy requirements. The solid–vapor (SV) separation unit offers some key advantages over traditional amine-scrubbing units such as lower energy requirements, lower capital costs, lower maintenance and operational costs, and production of water-free and solvent-free clean gas and liquid streams.

For natural gas sweetening, simulation results showed that the unit produces high-purity methane gas, with high removal ratios of $CO_2$ and $H_2S$ from the feed stream. Moreover, in the case of high concentrations of $CO_2$ and $H_2S$ in the feed stream, the separation can be enhanced by cooling the feed stream to lower temperatures within the SVE zone. Results showed that, for similar sweet gas purity, the developed SV unit consumes only ~27% of the energy required by the industry-popular amine-based technology.

In capturing $CO_2$ from flue gas streams using the SV separation unit, results proved that for the same output clean gas composition (which contains only 0.3% $CO_2$), the developed state-of-the-art SV separation unit consumes almost half of the energy required by the conventional process. Finally, The SV unit was simulated to separate noble gases (resembled by krypton and xenon) from nitrogen. Results indicated that the recovery for Xe is much higher than that of Kr, possibly due to the considerable difference between their triple point temperatures. Moreover, it was noticed that the energy consumption is relatively high, which can be due to the very low operating temperature required to achieve high recovery rates. Nonetheless, the SV separation unit developed herein was the first suggested solution for separating noble gases from nitrogen. However, in the absence of commercial processes to separate such mixtures; the SV unit was not compared to other technologies. Despite that, the SV unit proved the potential to be used in similar systems; such as air separation.

### 8.2 Future work

Taken together, the results reported in this work showed that the empirical phase equilibrium correlation model, which was developed herein based on the Peng-Robinson equation of state (PR EoS) with fugacity expressions, was successful in representing and describing the solid-fluid phase equilibria for a number of ternary gas

mixtures. Moreover, based on this model a state-of-the-art solid-vapor (SV) separation unit (which is operating in the solid-vapor equilibria region) was modeled and simulated.

The results reported herein are expected to be of a great benefit for professionals and researchers to understand the pertaining behaviors, and to design corresponding separation processes for different industries.

Several lines of research have raised from this work, which we recommend to be pursued and addressed in the future. Examples of such recommended research lines are listed below.

1- The ternary system representing the natural gas could be further expanded in to incorporate other gases found in the upstream natural gas, such as $C_{2+}$ gases and water vapor. Expanding the model in this study to describe such system would be invaluable for the industry.

2- Mercaptan compounds are sulfur compounds that are found naturally in natural gas. They have corrosive properties, and they damage catalysts in the downstream processing. Therefore, it is important to remove them from the natural gas. It is suggested to expand the model prediction capabilities for the natural gas systems to include them.

3- Natural gas produced from wells may contain high amounts of water vapor ($H_2O$). In this study, it was assumed that the sweetening process is for dry gas. However, it is suggested that in the future to study the impact of the presence of water on the SV unit process, and to estimate the cost of its drying to produce water-free gas streams.

4- It is highly recommended to determine experimentally the behavior of the ternary system $N_2$-Kr-Xe to accurately describe the solid-fluid equilibrium

regions for it. Such data will help to compare and evaluate the predictions of this model.

5- The composition of flue gas is determined by the type of fossil fuel burned. In the case of coal or other solid fuels, the flue gas consists of significant portions of $NO_x$ gases; which have disastrous impact on the environment. Hence, It is recommended to expand the ternary system ($N_2$-$O_2$-$CO_2$) to become a quaternary system (involving, e.g., $NO_2$ gas) and describe its solid-fluid behavior in order to design even a more developed separation unit for such harmful gases.

6- It is recommended to implement this system to other types of gas systems, such as air separation and hydrogen-ammonia systems.

7- The SV natural gas sweetening unit proved to be energy-efficient and useful in achieving high-purity methane gas. The emerging methane stream is at low temperature, therefore saving costs in case if the methane is going to be liquefied. Therefore, it is recommended to integrate the SV unit in a Liquefied Natural Gas (LNG) plant and study its performance and the energy savings that could be achieved from this step.

8- This study has not discussed the detailed design of the cooling systems used the SV separation unit. It is recommended to study the type of fluids (or refrigerants) that can be used to provide the cooling rates required by the process. Fluids such as propane found in natural gas streams, could be reused as a refrigerant in the SV separation process, hence resulting in the possibility of process integration between the SV separation process and upstream processes.

9- Solids formed in the proposed SV unit during the selective gas freezing could

constitute a mixture of $CO_2$ and $H_2S$ crystals. In the future, it is recommended to propose a design or a technique to separate mixed solids from each other to enhance their utilization.

10- While the SV unit proved that it could achieve significant energy savings, it is important to conduct a life cycle assessment and economic evaluation of the SV separation process.

# LIST OF PUBLICATIONS

From this dissertation, four articles have been published in peer-reviewed journals, and a fifth article is currently under review. Following is the list of the publications resulted from this work:

1- H. Ababneh, A. AlNouss, I. A. Karimi, and S. A. Al-Muhtaseb, “Natural Gas Sweetening Using an Energy-Efficient, State-of-the-Art, Solid and Vapor Separation Process,” *Energies*, vol. 15, no. 14, 2022, doi: 10.3390/en15145286.

2- H. Ababneh and S. A. Al-Muhtaseb, “A Review on the Solid-Liquid-Vapor Phase Equilibria of Acid Gases in Methane,” *Greenh. Gases Sci. Technol.*, vol. 12, no. 4, pp. 566–579, 2022, doi: 10.1002/ghg.2161.

3- H. Ababneh and S. A. Al-Muhtaseb, “Prediction of solid-liquid-vapor phase equilibria of noble gases in nitrogen,” *Arab. J. Chem.*, vol. 15, no. 6, p. 103866, 2022, doi: 10.1016/j.arabjc.2022.103866.

4- H. Ababneh and S. Al-Muhtaseb, “An Empirical Correlation-Based Model to Predict Solid-Fluid Phase Equilibria and Phase Separation of the Ternary System CH4-CO2-H2S,” *J. Nat. Gas Sci. Eng.*, vol. 94, p. 104120, 2021, doi: https://doi.org/10.1016/j.jngse.2021.104120.

5- H. Ababneh, A. AlNouss, and S. A. Al-Muhtaseb, “Carbon Capture from Post Combustion Flue Gas Using a State-of-the-Art, Anti-Sublimation, Solid-Vapor Separation Unit” Currently under review.

REFERENCES

[1] BP, “Statistical Review of World Energy 2020,” 2020.

[2] British Petroleum, “Energy Outlook 2020,” 2020.

[3] P. Theveneau, X. Xu, O. Baudouin, J. N. Jaubert, P. Ceragioli, and C. Coquelet, “Vapor-Liquid Equilibria of the CH4 + CO2 + H2S Ternary System with Two Different Global Compositions: Experiments and Modeling,” *J. Chem. Eng. Data*, vol. 65, no. 4, pp. 1802–1813, 2020, doi: 10.1021/acs.jced.9b01082.

[4] M. Riva, M. Campestrini, J. Toubassy, D. Clodic, and P. Stringari, “Solid-liquid-vapor equilibrium models for cryogenic biogas upgrading,” *Ind. Eng. Chem. Res.*, vol. 53, no. 44, pp. 17506–17514, 2014, doi: 10.1021/ie502957x.

[5] I. A. A. C. Esteves, M. S. S. Lopes, P. M. C. Nunes, and J. P. B. Mota, “Adsorption of natural gas and biogas components on activated carbon,” *Sep. Purif. Technol.*, vol. 62, no. 2, pp. 281–296, 2008, doi: https://doi.org/10.1016/j.seppur.2008.01.027.

[6] S. Langé *et al.*, “EXPERIMENTAL DE- TERMINATION OF THE SOLID-LIQUID-VAPOR LOCUS FOR THE CH 4 -CO 2 -H 2 S SYSTEM AND APPLICATION TO THE DESIGN OF A NEW LOW-TEMPERATURE DISTILLATION PROCESS FOR THE PURIFICATION OF NATURAL GAS,” in *94th GPA Convention*, 2016.

[7] B. T. Kelley, J. A. Valencia, P. S. Northrop, and C. J. Mart, “Controlled Freeze Zone™ for developing sour gas reserves,” *Energy Procedia*, vol. 4, pp. 824–829, 2011, doi: 10.1016/j.egypro.2011.01.125.

[8] K. Maqsood, A. Mullick, A. Ali, K. Kargupta, and S. Ganguly, “Cryogenic carbon dioxide separation from natural gas: A review based on conventional and

novel emerging technologies," *Rev. Chem. Eng.*, vol. 30, no. 5, pp. 453–477, 2014, doi: 10.1515/revce-2014-0009.

[9] International Energy Agency, "CO2 Emissions From Fuel Combustion 2017," 2017.

[10] IPCC, "Global warming of 1.5°C An IPCC Special Report on the impacts of global warming of 1.5°C above pre-industrial levels and related global greenhouse gas emission pathways, in the context of strengthening the global response to the threat of climate change," 2018.

[11] C. M. Fowler, "2.11 - Cracking Stimulated by Hydrogen," B. Cottis, M. Graham, R. Lindsay, S. Lyon, T. Richardson, D. Scantlebury, and H. B. T.-S. C. Stott, Eds. Oxford: Elsevier, 2010, pp. 923–927.

[12] R. C. Ropp, "Chapter 3 - Group 16 (O, S, Se, Te) Alkaline Earth Compounds," R. C. B. T.-E. of the A. E. C. Ropp, Ed. Amsterdam: Elsevier, 2013, pp. 105–197.

[13] F. Pouliquen *et al.*, "Hydrogen Sulfide," *Ullmann's Encyclopedia of Industrial Chemistry*. 15-Jun-2000, doi: https://doi.org/10.1002/14356007.a13_467.

[14] S. Moazzem, "A Review on Technologies for Reducing CO2 Emission from Coal Fired Power Plants," M. G. Rasul, Ed. Rijeka: IntechOpen, 2012, p. Ch. 11.

[15] P. Lettieri, L. Yassin, and S. J. R. Simons, "7 - Advanced thermal treatment of composite wastes for energy recovery," in *Woodhead Publishing Series in Composites Science and Engineering*, V. B. T.-M. Goodship Recycling and Reuse of Waste Composites, Ed. Woodhead Publishing, 2010, pp. 152–191.

[16] C. Song *et al.*, "Tri-reforming of Methane over Ni Catalysts for CO2 Conversion to Syngas With Desired H2/CO Ratios Using Flue Gas of Power Plants Without CO2 Separation," in *Carbon Dioxide Utilization for Global Sustainability*, vol.

153, S.-E. Park, J.-S. Chang, and K.-W. B. T.-S. in S. S. and C. Lee, Eds. Elsevier, 2004, pp. 315–322.

[17] H. A. Alalwan and A. H. Alminshid, “Science of the Total Environment CO 2 capturing methods : Chemical looping combustion ( CLC ) as a promising technique,” *Sci. Total Environ.*, vol. 788, p. 147850, 2021, doi: 10.1016/j.scitotenv.2021.147850.

[18] J. D. Figueroa, T. Fout, S. I. Plasynski, H. McIlvried, and R. D. Srivastava, “Advances in CO2 Capture Technology—The U.S. Department of Energy’s Carbon Sequestration Program,” *Int. J. Greenh. Gas Control*, vol. 2, pp. 9–20, 2008, doi: 10.1016/S1750-5836(07)00094-1.

[19] J. Godin, W. Liu, S. Ren, and C. C. Xu, “Advances in recovery and utilization of carbon dioxide: A brief review,” *J. Environ. Chem. Eng.*, vol. 9, no. 4, p. 105644, 2021, doi: https://doi.org/10.1016/j.jece.2021.105644.

[20] B. P. Spigarelli and S. K. Kawatra, “Opportunities and challenges in carbon dioxide capture,” *J. CO2 Util.*, vol. 1, pp. 69–87, 2013, doi: https://doi.org/10.1016/j.jcou.2013.03.002.

[21] R. M. Cuéllar-Franca and A. Azapagic, “Carbon capture, storage and utilisation technologies: A critical analysis and comparison of their life cycle environmental impacts,” *J. CO2 Util.*, vol. 9, pp. 82–102, 2015, doi: https://doi.org/10.1016/j.jcou.2014.12.001.

[22] M. Wang, A. Lawal, P. Stephenson, J. Sidders, and C. Ramshaw, “Post-combustion CO2 capture with chemical absorption: A state-of-the-art review,” *Chem. Eng. Res. Des.*, vol. 89, no. 9, pp. 1609–1624, 2011, doi: https://doi.org/10.1016/j.cherd.2010.11.005.

[23] H. Ababneh and S. Al-Muhtaseb, “An Empirical Correlation-Based Model to

Predict Solid-Fluid Phase Equilibria and Phase Separation of the Ternary System CH4-CO2-H2S," *J. Nat. Gas Sci. Eng.*, vol. 94, p. 104120, 2021, doi: https://doi.org/10.1016/j.jngse.2021.104120.

[24] H. Ababneh and S. A. Al-muhtaseb, "A Review on the Solid-Liquid-Vapor Phase Equilibria of Acid Gases in Methane," *Greenh. Gases Sci. Technol.*, vol. 12, no. 4, pp. 566–579, 2022, doi: 10.1002/ghg.2161.

[25] C. Font-Palma, D. Cann, and C. Udemu, "Review of Cryogenic Carbon Capture Innovations and Their Potential Applications," *C* , vol. 7, no. 3. 2021, doi: 10.3390/c7030058.

[26] J. A. Valencia, R. D. Denton, P. S. Northrop, C. J. Mart, and R. K. Smith, "Controlled freeze zone technology for the commercialization of Australian high CO2 natural gas," *Soc. Pet. Eng. - SPE Asia Pacific Oil Gas Conf. Exhib. APOGCE 2014 - Chang. Game Oppor. Challenges Solut.*, vol. 2, pp. 951–961, 2014, doi: 10.2118/171508-ms.

[27] A. Ali, K. Maqsood, N. Syahera, A. B. M. Shariff, and S. Ganguly, "Energy Minimization in Cryogenic Packed Beds during Purification of Natural Gas with High CO2 Content," *Chem. Eng. Technol.*, vol. 37, no. 10, pp. 1675–1685, Oct. 2014, doi: https://doi.org/10.1002/ceat.201400215.

[28] M. J. Tuinier, M. van Sint Annaland, G. J. Kramer, and J. A. M. Kuipers, "Cryogenic CO2 capture using dynamically operated packed beds," *Chem. Eng. Sci.*, vol. 65, no. 1, pp. 114–119, 2010, doi: https://doi.org/10.1016/j.ces.2009.01.055.

[29] P. Willson *et al.*, "Evaluation of the performance and economic viability of a novel low temperature carbon capture process," *Int. J. Greenh. Gas Control*, vol. 86, pp. 1–9, 2019, doi: https://doi.org/10.1016/j.ijggc.2019.04.001.

[30] C.-F. Song, Y. Kitamura, S.-H. Li, and K. Ogasawara, “Design of a cryogenic CO2 capture system based on Stirling coolers,” *Int. J. Greenh. Gas Control*, vol. 7, pp. 107–114, 2012, doi: https://doi.org/10.1016/j.ijggc.2012.01.004.

[31] M. J. Jensen *et al.*, “Prediction and validation of external cooling loop cryogenic carbon capture (CCC-ECL) for full-scale coal-fired power plant retrofit,” *Int. J. Greenh. Gas Control*, vol. 42, pp. 200–212, 2015, doi: https://doi.org/10.1016/j.ijggc.2015.04.009.

[32] A. Hart and N. Gnanendran, “Cryogenic CO2 capture in natural gas,” *Energy Procedia*, vol. 1, no. 1, pp. 697–706, 2009, doi: 10.1016/j.egypro.2009.01.092.

[33] K. A. Pacheco, Y. Li, and M. Wang, “Study of Integration of Cryogenic Air Energy Storage and Coal Oxy-fuel Combustion through Modelling and Simulation,” in *24 European Symposium on Computer Aided Process Engineering*, vol. 33, J. J. Klemeš, P. S. Varbanov, and P. Y. B. T.-C. A. C. E. Liew, Eds. Elsevier, 2014, pp. 1537–1542.

[34] Z.-Y. CHEN, S.-J. LIU, J.-L. WANG, and Y.-Z. CHANG, “Determination of Atmospheric Krypton and Xenon by Gas Chromatography-Mass Spectrometry in Direct Injection Mode,” *Chinese J. Anal. Chem.*, vol. 44, no. 3, pp. 468–473, 2016, doi: https://doi.org/10.1016/S1872-2040(16)60916-7.

[35] T. D. BURCHELL, “CHAPTER 13 - Fission Reactor Applications of Carbon,” T. D. B. T.-C. M. for A. T. Burchell, Ed. Oxford: Elsevier Science Ltd, 1999, pp. 429–484.

[36] M. Teller and H. Knapp, “Measurements of solubilities of solid krypton and xenon in liquid nitrogen,” *Cryogenics (Guildf).*, vol. 24, no. 9, pp. 471–476, 1984, doi: 10.1016/0011-2275(84)90005-5.

[37] E. Aprile *et al.*, “Removing krypton from xenon by cryogenic distillation to the

ppq level," *Eur. Phys. J. C*, vol. 77, no. 5, 2017, doi: 10.1140/epjc/s10052-017-4757-1.

[38] H. G. Donnelly and D. L. Katz, "Phase Equilibria in the Carbon Dioxide–Methane System," *Ind. Eng. Chem.*, vol. 46, no. 3, pp. 511–517, 1954, doi: 10.1021/ie50531a036.

[39] M. J. Pikaar, "A STUDY OP PHASE EQUILIBRIA IN HYDROCARBON-CO2 SYSTEMS.," University of London, 1959.

[40] C. J. Sterner, "Phase Equilibria in the CO2-Methane Systems BT - Advances in Cryogenic Engineering," 1961, pp. 467–474.

[41] J. A. Davis, N. Rodewald, and F. Kurata, "Solid-liquid-vapor phase behavior of the methane-carbon dioxide system," *AIChE J.*, vol. 8, no. 4, pp. 537–539, 1962, doi: 10.1002/aic.690080423.

[42] R. Thermodynamic Tables Project. K. M. de., Angus, S., Armstrong, B., *International thermodynamic tables of the fluid state : carbon dioxide*. Oxford; New York: Pergamon Press, 1976.

[43] A. Thermodynamic Tables Project. S., Armstrong, B., Reuck, K. M. de., *International thermodynamic tables of the fluid state-5 : methane*. Oxford; New York: Pergamon Press, 1978.

[44] N. L. Yarym-Agaev, L. D. Afanasenko, V. G. Matvienko, Y. Y. Ryabkin, and G. B. Tolmacheva, "Gas-liquid equilibrium in the system methane - hydrogen sulphide at a temperature below 273K," *Ukr. Khimicheskii Zhurnal*, vol. 57, pp. 701–704, Jul. 1991.

[45] S. Langé, M. Campestrini, P. Stringari, S. Langé, M. Campestrini, and P. Stringari, "Phase behavior of system methane + hydrogen sulfide," vol. 62, no. 11, pp. 4090–4108, 2017.

[46] C. Coquelet, A. Valtz, P. Stringari, M. Popovic, D. Richon, and P. Mougin, “Phase equilibrium data for the hydrogen sulphide+methane system at temperatures from 186 to 313K and pressures up to about 14MPa,” *Fluid Phase Equilib.*, vol. 383, pp. 94–99, 2014, doi: https://doi.org/10.1016/j.fluid.2014.09.025.

[47] J. P. Kohn and F. Kurata, “Heterogeneous phase equilibria of the methane—hydrogen sulfide system,” *AIChE J.*, vol. 4, no. 2, pp. 211–217, 1958, doi: 10.1002/aic.690040217.

[48] D. B. Robinson, A. P. Lorenzo, and C. A. Macrygeorgos, “The carbon dioxide-hydrogen sulphide-methane system: Part II. Phase behavior at 40°f. and 160°f.,” *Can. J. Chem. Eng.*, vol. 37, no. 6, pp. 212–217, Dec. 1959, doi: https://doi.org/10.1002/cjce.5450370603.

[49] A. Chapoy, C. Coquelet, H. Liu, A. Valtz, and B. Tohidi, “Vapour-liquid equilibrium data for the hydrogen sulphide (H2S)+carbon dioxide (CO2) system at temperatures from 258 to 313K,” *Fluid Phase Equilib.*, vol. 356, pp. 223–228, 2013, doi: 10.1016/j.fluid.2013.07.050.

[50] H. Li, “Thermodynamic properties of CO2 mixtures and their applications in advanced power cycles with CO2 capture processes,” Royal Insititute of Techonology, 2008.

[51] D. P. Sobocinski and F. Kurata, “Heterogeneous phase equilibria of the hydrogen sulfide–carbon dioxide system,” *AIChE J.*, vol. 5, no. 4, pp. 545–551, 1959, doi: 10.1002/aic.690050425.

[52] P. Théveneau, R. Fauve, C. Coquelet, and P. Mougin, “Measurement and modelling of solid apparition temperature for the CO2 – H2S – CH4 ternary system,” *Fluid Phase Equilib.*, vol. 509, p. 112465, 2020, doi:

https://doi.org/10.1016/j.fluid.2020.112465.

[53] R. E. Sonntag and G. J. Wylen, “The Solid—Vapor Equilibrium of Carbon Dioxide—Nitrogen,” *Adv. Cryog. Eng.*, pp. 99–105, 1962, doi: 10.1007/978-1-4757-0531-7_12.

[54] G. E. Smith, R. E. Sonntag, and G. J. Wylen, “Solid-Vapor Equilibrium of the Carbon Dioxide-Nitrogen System at Pressures to 200 Atmospheres,” *Adv. Cryog. Eng.*, pp. 197–206, 1964, doi: 10.1007/978-1-4757-0525-6_24.

[55] A. J. Rest, R. G. Scurlock, and M. F. Wu, “The solubilities of nitrous oxide, carbon dioxide, Aliphatic ethers and alcohols, and water in cryogenic liquids,” *Chem. Eng. J.*, vol. 43, no. 1, pp. 25–31, 1990, doi: 10.1016/0300-9467(90)80041-A.

[56] R. I. Yakimenko, N. P.; Gluch, G. M.; Iomtev, M. B.; Abramova, “Solubility of Solid Carbon-Dioxide in Liquid-Nitrogen,” *Zhurnal Fiz. Khimii*, vol. 49, pp. 209–210, 1975.

[57] M. F. Fedorova, “The solubility of C2h2 and CO2 in liquid nitrogen and oxygen,” *Zhurnal Fiz. Khimii*, vol. 14, pp. 422–426, 1940.

[58] O. R. SCHWEITZER, “SOLID-LIQUID-VAPOR PHASE EQUILIBRIA IN THE BINARY SYSTEMS: ETHYLENE - CARBON-DIOXIDE, PROPANE - CARBON-DIOXIDE, NITROGEN - CARBON-DIOXIDE, AND HELIUM - CARBON-DIOXIDE,” Wayne State University, 1962.

[59] O. Fandiño, J. P. M. Trusler, and D. Vega-Maza, “Phase behavior of (CO2+H2) and (CO2+N2) at temperatures between (218.15 and 303.15)K at pressures up to 15MPa,” *Int. J. Greenh. Gas Control*, vol. 36, pp. 78–92, 2015, doi: 10.1016/j.ijggc.2015.02.018.

[60] M. O. Amamchyan, R. G., Bertsev, V. V., and Bulanin, “Analysis of cryogenic

solutions according to IR absorption spectra," *Zavod. Lab*, vol. 39, pp. 432–434, 1973.

[61] V. De Stefani, A. Baba-Ahmed, A. Valtz, D. Meneses, and D. Richon, "Solubility measurements for carbon dioxide and nitrous oxide in liquid oxygen at temperatures down to 90 K," *Fluid Phase Equilib.*, vol. 200, no. 1, pp. 19–30, 2002, doi: 10.1016/S0378-3812(01)00821-4.

[62] R. Heastie, "Condensed solutions of the rare gases," *Pure Appl. Chem.*, vol. 2, no. 1–2, pp. 325–328, 1961, doi: 10.1351/pac196102010325.

[63] Mastera, "Vapour-Liquid Equilibrium Data from gasmixtures of Ar-N2 ; Kr-Ar, Kr-N2 and Xe-Kr and the Liquidus-lines of solid Xenon and of solid Krypton in Liquid air-component-mixtures," Berichte der Kernforschungsanlage Jülich, 1977.

[64] F. AspenTech, "Aspen Plus User Guide," 2000.

[65] I. K. Nikolaidis, G. C. Boulougouris, L. D. Peristeras, and I. G. Economou, "Equation-of-State Modeling of Solid-Liquid-Gas Equilibrium of CO2 Binary Mixtures," *Ind. Eng. Chem. Res.*, vol. 55, no. 21, pp. 6213–6226, 2016, doi: 10.1021/acs.iecr.6b00669.

[66] M. Seiler, J. Groß, B. Bungert, G. Sadowski, and W. Arlt, "Modeling of Solid/Fluid Phase Equilibria in Multicomponent Systems at High Pressure," *Chem. Eng. Technol.*, vol. 24, no. 6, pp. 607–612, Jun. 2001, doi: https://doi.org/10.1002/1521-4125(200106)24:6<607::AID-CEAT607>3.0.CO;2-T.

[67] A. Jäger and R. Span, "Equation of state for solid carbon dioxide based on the Gibbs free energy," *J. Chem. Eng. Data*, vol. 57, no. 2, pp. 590–597, 2012, doi: 10.1021/je2011677.

[68] Y. Tan, W. Nookuea, H. Li, E. Thorin, and J. Yan, “Cryogenic technology for biogas upgrading combined with carbon capture-a review of systems and property impacts,” *Energy Procedia*, vol. 142, pp. 3741–3746, 2017, doi: 10.1016/j.egypro.2017.12.270.

[69] A. Ali, A. Abdulrahman, S. Garg, K. Maqsood, and G. Murshid, “Application of artificial neural networks (ANN) for vapor-liquid-solid equilibrium prediction for CH 4 -CO 2 binary mixture,” *Greenh. Gases Sci. Technol.*, vol. 9, no. 1, pp. 67–78, 2019, doi: 10.1002/ghg.1833.

[70] J. H. Vera, “Book Review: Molecular thermodynamics of fluid-phase equilibria by John M. Prausnitz, Rüdiger N. Lichtenthaler and Edmundo Comes de Azevedo, Third Edition, 1999,” *Can. J. Chem. Eng.*, vol. 78, no. 2, pp. 429–430, Apr. 2000, doi: https://doi.org/10.1002/cjce.5450780222.

[71] D.-Y. Peng and D. B. Robinson, “A New Two-Constant Equation of State,” *Ind. Eng. Chem. Fundam.*, vol. 15, no. 1, pp. 59–64, Feb. 1976, doi: 10.1021/i160057a011.

[72] R. Span and W. Wagner, “A new equation of state for carbon dioxide covering the fluid region from the triple-point temperature to 1100 K at pressures up to 800 MPa,” *J. Phys. Chem. Ref. Data*, vol. 25, no. 6, pp. 1509–1596, 1996, doi: 10.1063/1.555991.

[73] P. Stringari, M. Campestrini, C. Coquelet, and P. Arpentinier, “An equation of state for solid-liquid-vapor equilibrium applied to gas processing and natural gas liquefaction,” *Fluid Phase Equilib.*, vol. 362, pp. 258–267, 2014, doi: 10.1016/j.fluid.2013.10.020.

[74] Q. Nasir, K. M. Sabil, and K. K. Lau, “Measurement of isothermal (vapor+liquid) equilibria, (VLE) for binary (CH4+CO2) from T=(240.35 to

293.15) K and CO2 rich synthetic natural gas systems from T=(248.15 to 279.15) K," *J. Nat. Gas Sci. Eng.*, vol. 27, pp. 158–167, 2015, doi: 10.1016/j.jngse.2015.08.045.

[75] A. S. Kapadia, W. Chan, and L. Moyé, *Mathematical Statistics with Applications*, 7th editio. Thomson, 2017.

[76] M. Ramdin, T. M. Becker, S. H. Jamali, M. Wang, and T. J. H. Vlugt, "Computing equation of state parameters of gases from Monte Carlo simulations," *Fluid Phase Equilib.*, vol. 428, pp. 174–181, 2016, doi: 10.1016/j.fluid.2016.06.012.

[77] A. M. Clark, A. H. Cockett, and H. S. Eisner, "The vapour pressure of hydrogen sulphide," *Proc. R. Soc. London. Ser. A. Math. Phys. Sci.*, vol. 209, no. 1098, pp. 408–415, 1951, doi: 10.1098/rspa.1951.0214.

[78] G. M. Schneider, "Book Review: Carbon Dioxide – International Thermodynamic Tables of the Fluid State, Bd. 3. Von S. Angus, B. Armstrong und K. M. de Rerrck. Pergamon Press Ltd., Oxford–New York 1976.," *Chemie Ing. Tech.*, vol. 49, no. 7, p. 594, Jul. 1977, doi: https://doi.org/10.1002/cite.330490727.

[79] X. Yang, D. Rowland, C. C. Sampson, P. E. Falloon, and E. F. May, "Evaluating cubic equations of state for predictions of solid-fluid equilibrium in liquefied natural gas production," *Fuel*, vol. 314, p. 123033, 2022, doi: https://doi.org/10.1016/j.fuel.2021.123033.

[80] S. B. Rodriguez-Reartes, M. Cismondi, and M. S. Zabaloy, "Computation of solid-fluid-fluid equilibria for binary asymmetric mixtures in wide ranges of conditions," *J. Supercrit. Fluids*, vol. 57, no. 1, pp. 9–24, 2011, doi: 10.1016/j.supflu.2011.02.004.

[81] G. De Guido, S. Langè, S. Moioli, and L. A. Pellegrini, “Thermodynamic method for the prediction of solid CO2 formation from multicomponent mixtures,” *Process Saf. Environ. Prot.*, vol. 92, no. 1, pp. 70–79, 2014, doi: 10.1016/j.psep.2013.08.001.

[82] K. Carter and K. D. Luks, “Extending a classical EOS correlation to represent solid-fluid phase equilibria,” *Fluid Phase Equilib.*, vol. 243, no. 1–2, pp. 151–155, 2006, doi: 10.1016/j.fluid.2006.02.021.

[83] L. Tang, C. Li, and S. Lim, “Solid-Liquid-Vapor Equilibrium Model Applied for a CH4-CO2 Binary Mixture,” *Ind. Eng. Chem. Res.*, vol. 58, no. 39, pp. 18355–18366, 2019, doi: 10.1021/acs.iecr.9b02389.

[84] K. Nasrifar and M. Moshfeghian, “Prediction of carbon dioxide frost point for natural gas and LNG model systems,” *J. Nat. Gas Sci. Eng.*, vol. 76, no. December 2019, p. 103206, 2020, doi: 10.1016/j.jngse.2020.103206.

[85] A. Yokozeki, “Analytical Equation of State for Solid-Liquid-Vapor Phases,” *Int. J. Thermophys.*, vol. 24, no. 3, pp. 589–620, 2003, doi: 10.1023/A:1024015729095.

[86] J. M. Prausnitz, R. N. Lichtenthaler, and E. G. de Azevedo, “Solubilities of Solids in Liquids,” in *Molecular Thermodynamics of Fluid-Phase Equilibria*, 3rd ed., Pearson Education, 1998, p. 864.

[87] M.-J. Huron, G.-N. Dufour, and J. Vidal, “Vapour-liquid equilibrium and critical locus curve calculations with the soave equation for hydrocarbon systems with carbon dioxide and hydrogen sulphide,” *Fluid Phase Equilib.*, vol. 1, no. 4, pp. 247–265, 1977, doi: https://doi.org/10.1016/0378-3812(77)80008-3.

[88] I. Tsivintzelis, G. M. Kontogeorgis, M. L. Michelsen, and E. H. Stenby, “Modeling phase equilibria for acid gas mixtures using the CPA equation of

state. I. Mixtures with H2S," *AIChE J.*, vol. 56, no. 11, pp. 2965–2982, Nov. 2010, doi: https://doi.org/10.1002/aic.12207.

[89] X. Tang and J. Gross, "Modeling the phase equilibria of hydrogen sulfide and carbon dioxide in mixture with hydrocarbons and water using the PCP-SAFT equation of state," *Fluid Phase Equilib.*, vol. 293, no. 1, pp. 11–21, 2010, doi: 10.1016/j.fluid.2010.02.004.

[90] J.-N. Jaubert, R. Privat, and F. Mutelet, "Predicting the phase equilibria of synthetic petroleum fluids with the PPR78 approach," *AIChE J.*, vol. 56, no. 12, pp. 3225–3235, Dec. 2010, doi: https://doi.org/10.1002/aic.12232.

[91] T. Holderbaum and J. Gmehling, "PSRK: A Group Contribution Equation of State Based on UNIFAC," *Fluid Phase Equilib.*, vol. 70, no. 2, pp. 251–265, 1991, doi: https://doi.org/10.1016/0378-3812(91)85038-V.

[92] M.-J. Huron and J. Vidal, "New mixing rules in simple equations of state for representing vapour-liquid equilibria of strongly non-ideal mixtures," *Fluid Phase Equilib.*, vol. 3, no. 4, pp. 255–271, 1979.

[93] O. Kunz and W. Wagner, "The GERG-2008 Wide-Range Equation of State for Natural Gases and Other Mixtures: An Expansion of GERG-2004," *J. Chem. Eng. Data*, vol. 57, no. 11, pp. 3032–3091, Nov. 2012, doi: 10.1021/je300655b.

[94] C. W. Leming and G. L. Pollack, "Sublimation Pressures of Solid Ar, Kr, and Xe," *Phys. Rev. B*, vol. 2, no. 8, pp. 3323–3330, Oct. 1970, doi: 10.1103/PhysRevB.2.3323.

[95] M. Campestrini, P. Stringari, and P. Arpentinier, "Solid-liquid equilibrium prediction for binary mixtures of Ar, O2, N2, Kr, Xe, and CH4 using the LJ-SLV-EoS," *Fluid Phase Equilib.*, vol. 379, pp. 139–147, 2014, doi: 10.1016/j.fluid.2014.07.020.

[96] S. I. Sandler, *Chemical, biochemical, and engineering thermodynamics*. 2006.

[97] J. M. Smith  Van Ness, H. C., Abbott, Michael M., *Introduction to chemical engineering thermodynamics.* Boston: McGraw-Hill, 2005.

[98] M. Riva, “Biomethane purification processes: thermodynamic study of solid-liquid-vapor equilibria of methane-rich mixtures,” Université Paris sciences et lettres, 2016.

[99] R. T. Jacobsen, R. B. Stewart, and M. Jahangiri, “Thermodynamic Properties of Nitrogen from the Freezing Line to 2000 K at Pressures to 1000 MPa,” *J. Phys. Chem. Ref. Data*, vol. 15, no. 2, pp. 735–909, Apr. 1986, doi: 10.1063/1.555754.

[100] F. von Henning and J. Otto, “Vapor-Pressure Curves and Triple Points in the Temperature Range from 14° to 90° Abs,” *Phys. Z.*, vol. 37, no. 18, p. 633, 1936.

[101] G. De Guido and L. A. Pellegrini, “Calculation of solid-vapor equilibria for cryogenic carbon capture,” *Comput. Chem. Eng.*, vol. 156, p. 107569, 2022, doi: 10.1016/j.compchemeng.2021.107569.

[102] L. Baxter, A. Baxter, and S. Burt, “Cryogenic CO2 Capture as a Cost-Effective CO2 Capture Process,” in *26th Annual International Pittsburgh Coal Conference 2009, PCC 2009*, 2009, vol. 1.

[103] K. Maqsood *et al.*, “Experimental and simulation study on high-pressure V-L-S cryogenic hybrid network for CO2 capture from highly sour natural gas,” *Process Saf. Environ. Prot.*, vol. 150, pp. 36–50, 2021, doi: 10.1016/j.psep.2021.03.051.

[104] M. J. Tuinier, M. van Sint Annaland, and J. A. M. Kuipers, “A novel process for cryogenic CO2 capture using dynamically operated packed beds—An experimental and numerical study,” *Int. J. Greenh. Gas Control*, vol. 5, no. 4, pp. 694–701, 2011, doi: https://doi.org/10.1016/j.ijggc.2010.11.011.

[105] M. J. Tuinier and M. van Sint Annaland, “Biogas Purification Using Cryogenic Packed-Bed Technology,” *Ind. Eng. Chem. Res.*, vol. 51, no. 15, pp. 5552–5558, Apr. 2012, doi: 10.1021/ie202606g.

[106] H. Shakeel, H. Wei, and J. M. Pomeroy, “Measurements of enthalpy of sublimation of Ne, N2, O2, Ar, CO2, Kr, Xe, and H2O using a double paddle oscillator,” *J. Chem. Thermodyn.*, vol. 118, pp. 127–138, 2018, doi: https://doi.org/10.1016/j.jct.2017.11.004.

[107] A. V Chadwick, “8 Diffusion in molecular solids,” in *Diffusion in Non-Metallic Solids (Part 1)*, D. L. Beke, Ed. Springer-Verlag Berlin Heidelberg, 1999.

[108] S. Mokhatab and W. A. Poe, “Chapter 7 - Natural Gas Sweetening,” in *Handbook of Natural Gas Transmission and Processing*, S. Mokhatab and W. A. B. T.-H. of N. G. T. and P. (Second E. Poe, Eds. Boston: Gulf Professional Publishing, 2012, pp. 253–290.

[109] J. G. Speight, “8 - Gas cleaning processes,” in *Natural Gas*, J. G. B. T.-N. G. (Second E. Speight, Ed. Boston: Gulf Professional Publishing, 2019, pp. 277–324.

[110] B. Guo and A. Ghalambor, “Chapter 8 - Dehydration,” in *Natural Gas Engineering Handbook*, B. Guo and A. B. T.-N. G. E. H. (Second E. Ghalambor, Eds. Gulf Publishing Company, 2005, pp. 143–171.

[111] K. Hill and A. Steele, “The triple point of xenon,” *Metrologia*, vol. 42, pp. 278–288, Aug. 2005, doi: 10.1088/0026-1394/42/4/013.

[112] K. Hill, “The Triple Point of Krypton,” *AIP Conf. Proc.*, vol. 1552, pp. 198–203, Sep. 2013, doi: 10.1063/1.4819539.

[113] A. Benamor, M. Nasser, and M. J. Al-Marri, “Gas Processing Technology-Treatment and Utilization,” M. A. B. T.-E. of S. T. Abraham, Ed. Oxford:

Elsevier, 2017, pp. 359–387.

[114] R. H. Jenny Seagraves, Ineos Oxide, Weiland, “Treating high CO2 gases with MDEA,” *www.digitalrefining.com*, 2009. [Online]. Available: https://www.digitalrefining.com/article/1000573/treating-high-co2-gases-with-mdea#.Ysh8T3ZBw2x.

# APPENDIX A: PENG ROBINSON EQUATION OF STATE FOR CALCULATING FUGACITY COEFFICIENTS[12]

The Peng-Robinson equation of state (PR-EoS) is given by

$$P = \frac{RT}{v-b_m} - \frac{a_m}{v(v+b_m)+b_m(v-b_m)} \qquad \text{(A-1)}$$

To find the PR-EoS coefficients for mixtures (i.e., $a_m$ and $b_m$values), the following mixing rules will be applied:

$$a_m = \sum_{i=1}^{N}\sum_{j=1}^{N} z_i z_j (a_i a_j)^{0.5}(1-k_{ij}) \qquad \text{(A-2)}$$

$$b_m = \sum_{j=1}^{N} z_i b_i \qquad \text{(A-3)}$$

where $k_{ij}$ is the binary interaction parameter characterizing molecular interactions between molecules *i* and *j*, and $z_i$ is the mole fraction of component *i* in the mixture. The individual component PR-EoS coefficients of component *i* (and similarly for component *j*) are given by

$$a_i = 0.45724\frac{R^2T_{ci}^2}{P_{ci}}\left[1+m_i\left(1-\left(\frac{T}{T_{ci}}\right)^{0.5}\right)\right]^2 \qquad \text{(A-4)}$$

$$b_i = 0.0778\frac{RT_{ci}}{P_{ci}} \qquad \text{(A-5)}$$

and $$m_i = 0.037464 + 1.54226\omega_i - 0.26992\omega_i^2 \qquad \text{(A-6)}$$

where $T_{ci}$, $P_{ci}$ and $\omega_i$ are, respectively, the critical pressure, critical temperature and acentric factor of component *i*.

The corresponding fugacity coefficient for component *i* in the mixture (in either vapour or liquid phase) is given by the following equation:

[12] H. Ababneh and S. Al-Muhtaseb, "An Empirical Correlation-Based Model to Predict Solid-Fluid Phase Equilibria and Phase Separation of the Ternary System CH4-CO2-H2S," J. Nat. Gas Sci. Eng., vol. 94, p. 104120, 2021, doi: https://doi.org/10.1016/j.jngse.2021.104120

$$\hat{\varphi}_i = \exp\left(\frac{b_i}{b_m}(z-1) - ln(z-B)\right.$$

$$\left. - \frac{A}{2\sqrt{2}B}\left(\frac{2\sum_{i=1}^{N}\sum_{j=1}^{N} z_i z_j (a_i a_j)^{0.5}(1-k_{ij})}{a_m}\frac{b_i}{b_m}\right) ln\left(\frac{z+2\left(1+\sqrt{2}\right)B}{z+2\left(1-\sqrt{2}\right)B}\right)\right)$$

(A-7)

where z is the compressibility factor, and A and B are given by

$$A = \frac{a_m P}{R^2 T^2} \quad \text{(A-8)}$$

$$B = \frac{b_m P}{RT} \quad \text{(A-9)}$$